Project No. 09-834

Advanced Models of LWR Pressure Vessel Embrittlement for Low Flux-High Fluence Conditions

Reactor Concepts RD&D

Dr. G. Robert Odette
University of California, Santa Barbara

In collaboration with:
University of Tennessee, Knoxville
Oak Ridge National Laboratory

Sue Lesica, Federal POC
Jeremy Busby, Technical POC

NEUP Nuclear Energy University Programs
U.S. Department of Energy

US DOE NUCLEAR ENERGY UNIVERSITY PROGRAM

Advanced Models of LWR Pressure Vessel Embrittlement for Extended Life Conditions

Final Report

STANDARD RESEARCH SUBCONTRACT NO. 90320
BATTELLE ENERGY ALLIANCE, LLC (BEA)
[OPERATING UNDER U.S. GOVERNMENT CONTRACT NO. DE-AC07-05ID14517]

Project 09-196

October 1, 2009 to September 30, 2012

G. Robert Odette (PI) and Takuya Yamamoto (Co-PI)

University of California Santa Barbara

Submitted June 17, 2013

TABLE OF CONTENTS

Contents	Page
Excecutive Summary	1
1. Introduction	6
2. Brief overview of microstructure processes in irradiated RPV steels	8
2.1 Nanoscale Hardening Features	8
2.2 Key Nanostructural Evolution Processes and Mechanisms	9
3. Physically based RPV embrittlement prediction models	13
3.1 Dose Rate Effect, Radiation Enhanced Diffusion and Precipitation Models - Two Feature Solute Trap Enhanced Recombination Model (2FM)	13
3.2 Chemistry Factor Fitting Model for 2FM	20
3.3 Three-feature model (3FM) with additional UMD hardening and sinks – historical background	23
3.3.1 Previous 3FM	26
3.3.2 Previous Three Feature Model (3FM) Analyses of Selected Test Reactor Data	30
4. Database Analyses	35
4.1 Formulating a Two-Feature Model (2FM) For the IVAR Database	35
4.2 Predicted $\Delta\sigma_y(\phi t_e)$ Curves for the IVAR Database	39
4.3 Updated 3FM	42
5. The BR2 High Flux-High Fluence Irradiation Study	46
5.1 BR2 Experiments	46
5.2 The BR2-A Irradiation	46
5.3 PIA Results and Analysis	47
5.4 Summary of BR2-A Results	52
5.5 The BR2-B irradiation	52
6. Design and Preparation for UCSB ATR-2 Irradiation Experiment to Develop a High Fluence Embrittlement Database	54
6.1 Background	54
6.2 Target Irradiation Conditions	55
6.3 Test Train Design	56

Contents	Page

6.4 Materials and Specimens 58

6.5 Status and Schedules 59

References 62

Appendix 1: Publications and Presentations from This work 67

Appendix 2: Related Publications and Presentations 69

Executive Summary

Reactor life extension requires predicting neutron embrittlement of reactor pressure vessel (RPV) steels manifested as hardening induced ductile to brittle transition temperature shifts (TTS). However, existing TTS models do not reliably extrapolate to high fluence levels of $\approx 10^{20}$ n/cm^2, pertinent to pressurized water reactor extended life conditions. Thus high fluence data from worldwide surveillance programs and test reactor irradiations must be used to develop improved low flux-high fluence TTS models for extended life. Higher flux test reactor irradiations that can reach high fluence will be critical. However, it is well known that higher flux affects TTS. One hypothesis that can rationalize complex flux effects, is that a significant population of a third feature, that is thermally unstable under irradiation, is important at high flux. These so-called unstable matrix defects (UMD) directly contribute to hardening and TTS; but they also act as point defect sinks that delay the evolution of so-called stable matrix features (SMF) and copper rich precipitates (CRP) hardening features by decreasing the efficiency of radiation enhanced diffusion (RED). As a result of this dual role of UMD, higher flux can increase, decrease, or leave unaffected the TTS, depending on the combination of all other embrittlement variables. Another important unresolved issue is that models have long predicted that Mn-Ni-Si late blooming phases (LBP) could form, even in low Cu steels, causing severe unanticipated embrittlement. ***Thus the challenge is to develop robust TTS models for low flux and high fluence conditions pertinent to extended vessel life based on a combination of insight on physical mechanisms, accelerated test reactor data and limited high fluence surveillance results.*** The focus of this work is on the effects of dose rate (or neutron flux) and alloy chemistry on the character and balance of the hardening features at high, extended life fluence.

The fine, nm-scale hardening features that develop under irradiation fall into four broad categories: 1) nano-scale Cu enriched precipitates, that can also contain large quantities of Mn, Ni and Si depending on the alloy composition, form under irradiation at a highly accelerated rate due to RED; 2) stable matrix features (SMF), that are smaller defect-solute cluster complexes, or their solute remnants, are believed to initially form directly in high-energy displacement cascades in alloys both with and without Cu; 3) unstable matrix defects (UMD) that are yet even smaller cascade cluster complexes that dissolve (anneal) during irradiation, thus increase in number with fluence up to a steady-state that is proportional to flux, acting as both sinks for point defects and hardening features; and, 4) so-called, late blooming Mn, Ni, Si rich precipitate phases (LBP) that may form in low and high Cu steels, that are defined as having less than $\approx$ 15% Cu, with very large volume fractions at high fluence.

Two (CRP, SMF) and three feature (CRP, UMD and SMF) models can rationalize almost all the complex interactive effects of metallurgical and irradiation variables on hardening and TTS observed in both high flux test reactor irradiation experiments and the low flux power reactor surveillance database (PREDB). RED, due to vacancy, and perhaps self-interstitial atom (SIA), super-saturations that enormously accelerate the kinetics of thermodynamically driven processes that would normally be very sluggish at RPV operating temperatures around 300°C. In RPV steels, solutes bind with and trap vacancies, thereby increasing the SIA-vacancy recombination rates. Strong solute trapping

shifts the SIA-vacancy recombination dominated dose rate dependent regime down to much lower flux.

Analysis of the PREDB (Eason, Odette, Nanstad and Yamamoto – EONY) found a dose rate dependence of TTS at flux less than $5x10^{10}$ n/cm^2. The EONY model used an effective fluence to account for the flux effects as $\phi t_e = \phi t(\phi_r/\phi)^p$; here ϕ_r is a reference flux. The EONY fit yield an overall p = 0.26. The precise, large and comprehensive Irradiation Variables (IVAR) database showed a similar, but stronger effect of dose rate, up to the highest flux in the experiment of $\approx 10^{12}$ n/cm^2, that is also attributed to solute enhanced recombination. Thus dose rate effects are expected to occur over a wide range due to the combination of thermal contributions to Cu diffusion at very low flux, solute enhanced recombination at intermediate flux and, perhaps, UMD cascade cluster sinks at the highest flux.

These concepts were used to develop a low flux, two-feature solute trap enhanced recombination model (2FM) that was previously applied to the IVAR database. The 2FM treats the SMF contribution in a semi-empirical fashion as $\Delta\sigma_{smf}(\phi t) = CF_{smf}\sqrt{\phi t_e}$, where CF_{smf} is a composition (Ni, Mn, P,….) dependent chemistry factor found by fitting the IVAR database for low Cu steels. The effects of flux are treated in terms of a rate theory model that evaluates the fraction of defects that reach sinks, $g_s < 1$. Cu RED models (D*) use the ratio of the Cu to self-diffusion coefficient D_{cu}/D_{sd}, and the estimated radiation enhanced self-diffusion coefficient, D_vX_v, to estimate D* as $\approx [D_{cu}/D_{sd}]D_vX_v$, where D_v and X_v are the vacancy diffusion coefficient and atom fractions, respectively. The growth of CRPs by long-range RED of Cu and other solutes is treated by an Avrami model expressed in terms of a normalized precipitate volume fraction ($0 < f/f_{max} < 1$) as a function of ϕt_e. The CRP hardening is modeled as $\Delta\sigma_y = \Delta\sigma_{ymax}\sqrt{[f/f_{max}]}$. The fluence dependence is set by p and $\phi t_{0.8}$, the fluence at $\Delta\sigma_y = 0.8\Delta\sigma_{ymax}$, and an Avrami shape factor β, which is 3/2 for purely diffusion controlled growth. The effect of flux is represented by a single effective p fit parameter.

This so-called fitted recombination model (FRM) was applied to all the alloys for each individual irradiation condition in the IVAR experiment. The average p was ≈ 0.38, raging from ≈ 0.32 to 0.48 where the latter approaches fully recombination-dominated limit of 0.5. The p tended to increase with increasing alloy solute content, consistent with the proposed trapping mechanism. The p also decreased at higher irradiation temperature, consistent with increased de-trapping rates. The $\Delta\sigma_{ymax}$ is an effective CRP chemistry factor that depends in a systematic way on the alloy Cu, Ni and Mn solute content. The same p applies to both CRP and SMF contributions. The $\phi t_{0.8}$ decreased with increasing Cu and decreasing Ni. Note, all the IVAR alloys showed the same general trends, manifested as increases in fluence required to produce the same amount of precipitation and hardening in the pre-plateau transition, with increasing flux. Finally, the hardening and embrittlement in IVAR were found to be remarkably similar to independent EONY fits to the independent surveillance database.

The IVAR FRM parameters were cross fit as functions of the alloy Cu, Ni and Mn to derive an analytical 2FM with improved treatment of SMF hardening and the compositional dependence of $\Delta\sigma_y$ reflected in both the equivalent p, $\phi t_{0.8}$ and $\Delta\sigma_{ymax}$ fitting terms. The new analytical 2FM is highly consistent with the IVAR (and

surveillance) database. The two key results of the 2FM are: 1) Ni and Mn add to the Cu only hardening with coefficients of ≈ 120 and 30 MPa/% respectively; and, 2) the higher Cu reduces and higher Ni increases the $\phi t_{0.8}$ needed to approach the hardening plateau.

These IVAR and EONY analyses form the foundation for treating rate effects in the low to intermediate flux regime. However, many test reactor irradiations are at higher, up to much higher flux. Early work by Mader and Odette empirically estimated the effect of high flux on the balance of the various hardening features, based on low temperature short time (350°C/5h) post-irradiation annealing (PIA) microhardness recovery measurements. This work led to a three feature model (3FM) UMD, SMF, CRP interpretation of flux effects, as outlined above. More recent application of the 3FM was shown to rationalize most trends observed in high flux test reactor data. The 3FM has a reasonably sound physical basis, but it was initially developed only for very low fluence conditions. Thus one of the main objectives in this research was to evaluate, refine and extend the 3F model by low-temperature short time PIA of a large number of RPV alloys included in both the lower flux-fluence IVAR and to much higher flux-fluence BR2 irradiations.

Thus considerable effort was directed at refining the 3FM based on fits to test reactor data for alloys irradiated over a range of flux, up to high fluence in some cases. This data was primarily from IVAR and the RADAMO study in the Belgian BR2 test reactor. The Mader-Odette model was used to calculate the UMD hardening, but with new fit parameters. The CRP and SMF contributions were taken for the EONY model using an effective fluence, ϕt_e. The agreement between the revised 3FM and the IVAR and other test reactor data is reasonable to good in all cases. However, these newer results suggest that the original 3FM overestimated the UMD hardening and underestimated the corresponding UMD annealing time, by about a factor of 2 in both cases.

In order to obtain data more directly relevant to the 3FM, an extensive study was carried out on a subset of 29 alloys irradiated at IVAR low to intermediate flux that were also irradiated in the BR2 reactor at high flux to a much higher fluence (BR2-A). The nominal irradiation conditions in BR2-A were 300°C at 10^{14} n/cm^2-s from 1.7 to 12.7 x10^{19} n/cm^2. One capsule was irradiated BR2 at a lower flux of 1.3 x 10^{12} n/cm^2-s to 2.1 x10^{19} n/cm^2. PIA experiments on the BR2-A and IVAR alloys were used to discriminate the flux-dependent UMD, SMF and CRP contributions from ≈ 6x10^{10} to 10^{14} n/cm^2-s up to 1.1x10^{20} n/cm^2. The 350°C-5h PIA produces significant hardening recovery in all the high flux BR2 cases, but little recovery for the low flux IVAR conditions. Rcovery generally increases with fluence. The high BR2 flux clearly delays CRP and SMF hardening. The delays are observed in both mechanical properties and directly measured CRP nanostructures. However, again the recovery observed in BR2 is less than estimates in the original 3FM. The corresponding recovery times are ≈ 2 times larger, than estimates in the previous 3FM. There is also evidence of delayed emergence of late blooming phases in both Cu free and high Cu alloys with 0.8, 1.25 and 1.6%Ni in the high flux and fluence BR2-A irradiations (ongoing work not discussed here). It is noted that PIA recovery of hardness in the intermediate flux BR2-A irradiation is larger than expected and not well understood. Further, there is significant scatter in the hardness data that may affect some data comparisons

A second BR2-B irradiation was conducted at 290°C at a flux of ≈ 2 x 10^{13} n/cm^2-s to ≈ 10^{20} n/cm^2. The hardness generally follows compositional trends observed at lower flux, and was found to be insensitive to PIA. The hardening in this irradiation was similar to the trend in the annealed higher flux BR2-A data. The BR2-B specimens were subject to positron annihilation spectroscopy (PAS) measurements of both lifetimes and orbital electron momentum (OEM) spectra, as characterized by high and low momentum components. Significant changes in the PAS OEM and lifetimes occur PIA at 350°C for 5 h. The low momentum component of OEM and lifetime is larger in the as-irradiated condition and increases with flux, fluence and Cu content. The highest lifetime is ≈ 180 ps. PIA reduces or eliminates the flux, fluence and Cu sensitivity. These results may suggest that UMD are associated with a mono-vacancy. However the effect of vacancies associated with solute clusters is not known.

A significant fraction of the effort in this program was directed at building the National Scientific Users Facility (NSUF) UCSB ATR-2 RPV Steel Irradiation Experiment (UCSB ATR-2) intended to fill the gap in embrittlement data. It contains a total of ≈ 1664 specimens that were primarily prepared as part of this program. The UCSB ATR-2 irradiation includes a large number (≈180) of RPV steels that fall into two broad categories: 1) those which have been irradiated in a number of other programs over a wide range of flux; and, 2) a new set of alloys that will fill in major gaps in the effects of composition on embrittlement. Irradiations are being carried out at nominal temperatures of 250, 270, 290 and 310 °C. The peak flux of ≈ 3.8x10^{12} n/cm^2-s will produce a maximum fluence of ≈ 10^{20} n/cm^2. All of the alloys are included in the form of multipurpose disc coupons. These specimens will be used for hardness and shear punch tests and for making a wide variety of microstructural samples for techniques that include transmission electron microscopy (TEM), small angle neutron scattering (SANS), atom probe tomography (APT), resistivity-Seebeck coefficient measurements (RSC) and X-ray diffraction (XRD). A subset of 55 alloys is included in the form of tensile specimens and 3 alloys as disc compact tensions specimens.

UCSB ATR-2 will provide high fluence data at an intermediate flux that can be linked with other test reactor and surveillance data over a much wider range of flux. The ATR-2 test train provides a means to monitor and control sample temperatures. The radial gap, between the sample holders and test train tube inner diameter, is filled by a gas mixture of helium and argon. The gas gap width is designed to allow temperature control over the lifetime of the experiment, within the accessible range of the He/Ar gas composition. The irradiation temperature is monitored by thermocouples located in close proximity to the specimen packets. Several different specimen geometries were included in the experiment. All specimens were placed inside smaller thin-walled tube packets. Packets of irradiation specimens were assembled that represent a common sample geometry and irradiation temperature. Twenty mm diameter disc multi-purpose coupons (DMC) make up the majority of the samples. They are complemented by a smaller subset of tensile and disc pre-cracked compact tension (DCT) fracture specimens. Diffusion multiples were also included. The specimen sub-capsule packets were fabricated and assembled at UCSB. Final assembly of the test train was performed at Idaho National Laboratory (INL).

UCSB ATR-2 experiments started irradiation on 6/7/2011. Except the low-mid flux range at the bottom being slightly affected by adjacent high temperature zone, all the sub-capsules have maintained within ≈ 15 °C of the target temperatures. Post-irradiation examination is expected to begin in early 2014.

Advanced Models of LWR Pressure Vessel Embrittlement for Extended Life Conditions

Section 1. Introduction

In service exposure to energetic neutrons degrades the fracture toughness of reactor pressure vessel (RPV) steels. Irradiation embrittlement is typically characterized by a shift in an indexed transition temperature marking the transition between the low toughness brittle (cleavage) and high toughness ductile (microvoid coalescence) fracture regimes. Embrittlement is an unresolved issue for light water reactor (LWR) life extension, since transition temperature shifts (TTS) must be predicted using so-called embrittlement trend curve (ETC) for high 80-year fluence levels up to $\approx 10^{20}$ n/cm^2, which is well beyond the current surveillance database [1,2].

A large number of irradiation and metallurgical variables, and variable combinations, control TTS [3-8]. The irradiation variables include the neutron flux (ϕ), fluence (ϕt), energy spectrum, and irradiation temperature (T_i). The metallurgical variables include the start-of-life concentrations and distributions of the alloy solutes such as Cu, Ni, Mn and P, and the microstructure as mediated by composition and thermo-mechanical processing history.

Thus the ultimate objective of ETC predictions is to provide robust, physically based and experimentally validated predictive relations between TTS and *specific combinations* of the embrittlement variables, viz. - TTS = f(ϕ, ϕt, T_i, Cu, Ni, Mn, P, product form, heat treatment,…). To be successful, ETC development must be closely integrated with a wide range of experiments. Key experiments include characterizing both mechanical properties and the corresponding microstructural evolutions for a balanced and well-controlled matrix of combinations of the important embrittlement variables, as well as focused mechanism studies.

The primary embrittlement mechanism in Mn-Mo-Ni-P RPV steels is irradiation hardening ($\Delta\sigma_y$) produced by nanometer (nm)-scale features that develop as a consequence of irradiation [2-23]. The nano-features are clusters that contain varying amounts of both defects created by irradiation and alloy solutes. Solute clustering is accelerated by radiation-enhanced diffusion (RED). The thermodynamics and kinetics of the evolution of the nano-features are mediated by the combination of irradiation and metallurgical variables. The sequence of relations -- irradiation and metallurgical variables to the nanofeatures -- nanofeatures to $\Delta\sigma_y$ -- $\Delta\sigma_y$ to ΔT -- can be incorporated into predictive TTS models [7,8,14,17]. Such physically based models can provide higher confidence in TTS predictions when extrapolated beyond the range of available data than simple statistical eqution fits to databases.

Over the last 25 years tremendous advances in understanding of embrittlement mechanisms, and improved physically motivated TTS models, such as described in Ref. 1, now provide generally excellent statistical fits to a much larger US power reactor (surveillance) embrittlement database (PREDB) [7,8]. Further, the test reactor database has evolved, and now includes the results of the Irradiation Variables (IVAR) program [3], which was a large systematic effort to characterize embrittlement mechanisms, to develop high resolution maps of the effects of embrittlement variables and variable

combinations, with special emphasis on flux effects, and to provide independent checks on the PREDB based TTS models.

Current TTS models reflect the hardening effects of two features generally cited as being copper rich precipitates (CRP) and stable matrix features (SMF). CRP form in steels with more than ≈ 0.07% Cu while SMF form in both low and higher Cu steels. However, it has been shown recently that existing TTS models cannot reliably extrapolate to high fluence levels of up to ≈ 10^{20} n/cm^2 pertinent to pressurized water reactor extended life conditions, since 99% of the PREDB data is at < ≈ $5x10^{19}$ n/cm^2. Figure 1.1 plots predicted minus measured residuals for the TTS low flux PREDB based TTS model used for accident analysis [6] applied to a large independent body of generally higher flux test reactor data. The large negative residuals, that increase with fluence, show that the current model systematically and significantly underpredicts the test reactor TTS. Thus, reliably modeling high fluence embrittlement at the much lower RPV fluxes is a critical issue. High fluence data from other surveillance programs and test reactor irradiations must be used to develop improved low flux-high flurnce TTS models for extended life.

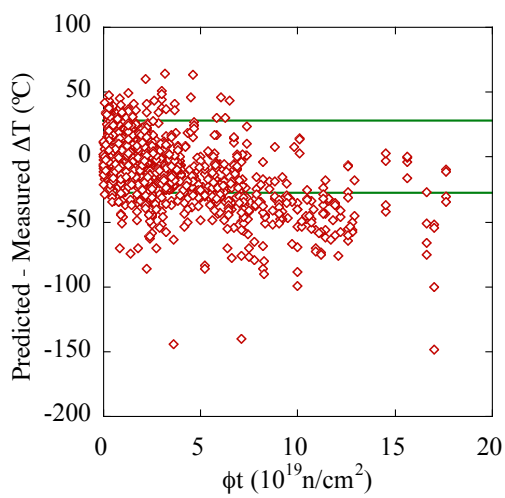

Figure 1.1 EONY model predicted minus measured residuals for the test reactor database assembled by M. EricksonKirk [6]

Higher flux, accelerated test reactor irradiations can access high fluence. However, flux influences the various hardening features and corresponding TTS for a given alloy, irradiation temperature and fluence [24-26]. Indeed, there is evidence that a significant population of a third defect, that is thermally unstable under irradiation, is important at high flux [25,26]. These so-called unstable matrix defects (UMD) directly contribute to hardening and TTS, but they also act as point defect sinks that delay the SMF and CRP hardening contributions by decreasing the efficiency of RED. As a result of this dual role of UMD, higher flux can increase, decrease, or leave unaffected the TTS, depending on the combination of all other embrittlement variables.

Another improtant unresolved issue is that models have long predicted that Mn-Ni-Si late blooming phases (LBP) could form in low Cu steels after a significant incubation

fluence (hence, the term "late blooming"), resulting in severe unanticipated TTS [2,13,15-18]. Current regulatory models *do not* reflect potential LBP contributions to TTS. However, recent research has clearly demonstrated the existence of LBP for a wide range of alloys and irradiation conditions [6,18-21]. It is not longer a matter of if LBP can form, but rather when, where and how.

Thus the challenge is to develop robust TTS models for low flux and high fluence conditions pertinent to extended vessel life based on a combination of physical models, accelerated test reactor data and limited surveillance data.

The focus of this work is on the effects of dose rate (or neutron flux) and alloy chemistry on the character and balance of the hardening features. Dose rate effects have been clearly observed in well-controlled experiments such as IVAR [7,27]. They are also found in the PRDB, but are less apparent, due to covariance of irradiation and material variables, large data uncertainties and scatter, and the limited variable ranges and independent combinations [7,8]. While they have been shown to be self-consistent [7,8,28], further integration of IVAR and PREDB embrittlement models is one of the objectives of this work.

Thus Section 2 we begin in with a brief summary of the current knowledge base of the multiscale nano-structural processes that control embrittlement, including that we have developed within this 3-year project. In Section 3 we describe the mechanistic models based on this knowledge base. Section 4 briefly summarizes the IVAR and other test reactor databases. These data are used in Section 5 to analyze dose rate and chemistry effects on irradiation hardening ($\Delta\sigma_y$) and embrittlement (TTS). In section 6, we describe the results of a high flux and fleunce irradiation experiment in the BR2 reactor in Belgium. Finally, in section 7 we outline our new ongoing UCSB ATR-2 irradiation experiment in the Advanced Test Reactor (ATR) at Idaho National Laboratory (INL), as a part of the ATR national scientific user facility (NSUF) program. ATR-2 that will provide higher dose irradiation hardening and embrittlement data to validate, fine tune or develop further our low fluence models to a higher dose.

Section 2. Brief overview of microstructure processes in irradiated RPV steels

2.1 Nanoscale Hardening Features: The fine, nm-scale hardening features that develop under irradiation fall into three broad categories.

<u>Precipitates:</u> Nano-scale precipitates that form under irradiation at a highly accelerated rate due to RED include: a) copper (Cu > 50%) Cu-Ni-Mn rich precipitates (CRP); b) manganese-nickel (Cu < 50%) Mn-Ni-Cu rich precipitates (MNP); c) so-called late blooming phases (Cu < 15% Cu) Ni-Si-Mn precipitates (LBP) that may develop at high fluence, even in low/no Cu steels; and, d) alloy phosphides precipitates.

<u>Stable Matrix Features (SMF):</u> Defect (vacancy)-solute cluster complexes, or their solute remnants, are believed to initially form directly in high-energy displacement cascades in alloys both with and without Cu. These featues are stable under irradiation (do not dissolve) thus increase in number in rough proportion to the fluence. SMF may evolve in to LBP.

Unstable matrix defects (UMD): Smaller cascade cluster complexes that dissolve during irradiation, thus increase in number up to a steady state that is proportional to flux. UMD act as both sinks for point defects and hardening features.

Dislocation Loops: A population of fairly large (several nm) dislocation loops may develop in steels at sufficiently high flux and fluence. The significance of interstitial loops for conditions pertinent to RPV embrittlement is not well established; it is believed that loops play a secondary role, in hardening and TTS, if any.

Three feature (precipitates, UMD and SMF) models (3FM) can rationalize almost all the complex interactive effects of metallurgical and irradiation variables on hardening and embrittlement observed in both controlled test reactor irradiation experiments and the PREDB. Modeling the evolution of these features is discussed below.

2.2 Key Nanostructural Evolution Processes and Mechanisms

Cascade defect generation and aging: Primary defects are generated in displacement cascades by high-energy primary recoil atoms produced by fast neutrons are initially in the form of single and small clusters of vacancies and self interstitial atoms (SIA). These defects are mobile and some vacancy and SIA rapidly recombine in the cascade. Mobile defects that escape local recombination either initially cluster or leave the cascade; the escaping defects ultimately reach sinks by long-range diffusion. The SIA defects are the most mobile and, unless strongly trapped, quickly escape in times on the order of μs or less. However, a large fraction of the remaining vacancies undergo correlated rearrangements within the cascade to form larger clusters with lower energy and higher thermal stability; they also retain significant mobility. The vacancy clusters are complexed with various solutes like Mn, Ni, Si and Cu that are bound to their surfaces. The complexes dissolve by emitting vacancies slowly (complexes have higher thermally stability) compared to pure vacancy clusters. Vacancy cluster complexes continue to slowly evolve by a combination of dissolution-coarsening and cluster migration-coalescence reactions. The vacancies in intermediate sized UMD cluster complexes dissolve and diffuse to sinks during irradiation. The steady-state number density of UMD depends on their formation cross-section, dissolution time, hence temperture, and the dose rate.

Larger stable matrix feature (SMF) cluster complexes can persist in aging cascades for very long periods of time. Indeed, some cluster complexes, as well as the solute cluster remnants of vacancy cluster complexes, likely serve as the nucleation sites for SMF that grow continuously by long-range diffusion of solutes. Over time, additional cascades overlap regions containing previously formed aging cascades. Cascade overlap results in additional recombination and formation of new cluster complexes. Vacancy solute cluster complexes are believed to be the dominant UMD (smaller ones) and SMF (larger remnants) embrittlement features.

While computer simulations suggest that a/2<111> SIA clusters (loops) are intrinsically mobile in pure Fe, they are likely trapped by solutes and solute atmospheres in multiconstituent steels. Interactions between a/2<111> SIA clusters can form immobile a/2<100> dislocation loops. Such loops grow at high ϕt by absorbing a bias driven excess flux of migrating SIA relative to the corresponding vacancy flux. These complex

(multiple) cascade aging processes are being modeled using a combination of molecular dynamics (MD) and various Monte Carlo (MC) methods.

Long Range Defect and Solute Diffusion: Radiation enhanced diffusion (RED) due to vacancy (and perhaps SIA) supersaturation can enormously accelerate the kinetics of thermodynamically driven processes that would normally be very sluggish at RPV operating temperatures around 300°C. The supersaturation is governed by the balance between the vacancy generation rates and the corresponding rate that they are either annihilated at sinks or recombined with SIAs. At very high dose rates UMD are the dominant sink. In this regime the RED coefficient (D*) is independent of flux and the net solute diffusion depends only on time rather than fluence. At lower flux, where vacancy cluster complexes can be neglected, D* varies with increasing flux between a dose rate and temperature-independent sink dominated regime and a dose rate temperature-dependent recombination dominated regime. In the sink dominated regime, D* scales with flux and in the recombination dominated regime D* scales with the square root of flux. Thus in the sink-dominated regime, the net Cu diffusion (D*t) leading to precipitation at a specified fluence is independent of flux, while D*t scales with the inverse of the square root of flux in the recombination-dominated regime. At very low D* approaches the thermal diffusion coefficient and D*t at a specified fluence again depends on the inverse of flux.

Lattice recombination can be neglected in pure Fe at dose rates even well in excess of those typically encountered in accelerated RPV steel test reactor irradiations. However in alloys, solutes bind with and trap vacancies, thereby increasing the recombination rate. Strong solute trapping shifts the recombination dominated dose rate dependent regime down to much lower flux (see below). Thus flux effects on RED (D*) are expected in all but the sink-dominated regime. The magnitudes of D* also depends on complex binding interactions between vacancies and solutes that increase the thermal vacancy concentration and control the frequency of five (or more) vacancy exchanges with the solutes and up to the fifth nearest neighbor atoms [29-33]. Solute-vacancy binding can lead to solute D* that is significantly greater than the radiation enhanced self-diffusion coefficient of in pure Fe.

Precipitation: RED leads to accelerated clustering and precipitation of Cu and other solutes from supersaturated solution. Following typical heat treatments, up to about 0.3% Cu remains dissolved in the steel compared to the equilibrium solubility of less than 0.01% at 300°C. Because of the low temperature and large thermodynamic driving force (supersaturation), Cu clusters homogeneously nucleate rapidly and on a very fine scale. For typical alloy compositions, the activity of Mn is lower in the Cu clusters than in the Fe matrix. Thus Mn is enriched in CRP. There are also strong Mn-Ni-Si interactions, leading to the enrichment of these elements in the CRP. Additional enrichment occurs because the interface energy between the precipitate and Fe-matrix is lower for Mn and Ni compared to Cu. The Mn and Ni content in the precipitates increases with increasing alloy content of these elements and decreasing temperature. In some regimes CRP give way to Mn-Ni rich precipitates (MNP). The dividing line between CRP and MNP is taken as 50%Cu. Ni, Si and Mn are alloying elements with typical molar concentrtions of 2-3%. Since almost all the Cu precipitates, the primary functional effect of the alloying solutes is to increase the volume fraction of the CRP, MNP and LBP.

The nucleation rates LBP are expected to be low, thus large incubation fluences are required for their formation [3,11,16,29,34-36]. Some Cu helps catalyze LBP formation and MNP can acquire sufficient Ni+Si+Mn to qualify as LBP, based on the Cu < 15% criteria, even in high Cu steels. Once nucleated, the CRP, MNP and LBP continue to grow by RED of solutes. Nearly complete depletion of the dissolved Cu as well as more limited decreases in the matrix Mn and Ni terminate growth. However, once formed LBPs may grow to much larger volume fractions in alloys with high concentrations of Mn and Ni.

Rate theory cluster dynamics models have been used to model precipitation by the integration of the full set master equations that describe the time evolution of the concentration (C_n) of individual cluster containing n precipitating solutes [3,11,16,34]. The models incorporate both rate (e.g., diffusion) controlled transport kinetics and evolving thermodynamics in the coefficients that specify the incorporation and emission rate of solutes into and out-of the clusters. To date most detailed models have been applied to Cu clustering showing the overlapping stages of nucleation, growth and coarsening. Within the limits of spatial and short-time fluctuation averaging, the cluster dynamics models can incorporate an essentially arbitrary level of physical detail. For example, it is possible to generalize the master equation approach to model the formation of defect-solute complexes and multi-element precipitates, although the numerical complexity rapidly escalates with the number of species. To date simpler thermodynamic grow-shrinkage models have been used to treat the flow of solutes (Mn, Ni) to and from the precipitates, based on differences in their activities relative to the Fe matrix [3,11,16,30,34,36]. The activities are based on extended regular solution theory, using excess enthalpies and entropies for the various binary interactions (Cu-Ni, Cu-Mn, Ni-Mn) taken from the literature (with slight modifications in some cases to account for the bcc crystal structure). The activity evaluations also account for the composition dependent interface energy. The predicted precipitate compositions, which are assumed to be uniform, are in reasonable qualitative agreement with experimental estimates.

Precipitates compositions and structures have also been modeled with lattice MC methods to evolve the lattice cohesion Hamiltonian to a configurational free energy minimum, based on a regular solution pair bonding approximation [16,30,35,37]. Since the same basic thermodynamic data is used to evaluate the pair bond energies, the overall compositions in these simulations are similar to those predicted by the mean field thermodynamic models. However, the LMC simulations provide insight on the detailed structure of the precipitates. CRPs are typically composed of a Cu rich core with some Mn, surrounded by a Mn-Ni rich shell, which is partially ordered. At higher Ni and Mn and lower Cu levels the smaller coated Cu clusters are often attached to larger nearly pure and highly ordered Mn-Ni precipitates. These structures are remarkably similar to the solute arrangements observed in three dimensional atom probe studies [38,39]. The major limitations on the KLMC and LMC simulations are the use of simple empirical pair bond potentials. Further progress will require improved alloy potentials.

<u>The Eason, Odette, Nanstad and Yamamoto (EONY) TTS Model and Dose Rate Effects</u> [7,8,28]. Proper treatment of dose rate, or flux (ϕ), effects is a key outstanding challenge to reliably predicting embrittlment. The previous discussion provides a framework for understanding dose rate effects. To begin we note that UMD are not significant at dose

rates pertinent to RPV and surveillance capsules. The current basis for predicting embrittlement is the two-feature CRP plus SMF EONY model [7,8]. In the EONY study, physically based analytical models were fit to a large PREDB TTS (775 points) from surveillance programs [7,8]. The CRP contribution to TTS is a product of two terms. One term depends on the alloy Cu and Ni content and the other is a function of flux and fluence (or effective fluence). The CRP contribution *saturates* due to Cu depletion. The SMF is independent of Cu (< 0.072%), but increases with increasing P and Mn and decreasing irradiation temperature (T_i). The SMF contribution does not saturate, increasing continuously with the square root of a flux-dependent fluence, or effective fluence. The dose rate effect is treated in terms of an effective flunce (ϕt_e) as

$$\phi t_e = \phi t(\phi_r/\phi)^p \tag{2.1}$$

Here ϕt and ϕ are the actual fluence and flux respectively, ϕr is an abritray reference flux and p is a scaling exponent. Dose rate influences the pre-plateau CRP contribution, but the saturated CRP TTS levels are independent of flux. The SMF varies with the square root of the effective fluence. This model is schematically illustrated in Figure 2a. It is also noted that several earlier two-feature models have long been the basis for predicting TTS for both C-Mn-Ni-Mo light water reactor (LWR)-type steels [12,13] and C-Mn steels used in Magnox reactors [9].

The EONY analysis found a dose rate dependent regime in the PREDB at flux less than $5x10^{10}$ n/cm^2, with an overall p = 0.26. However, the IVAR database shows a similar or stronger effect up to the highest flux in the experiment $\approx 10^{12}$ n/cm^2 that is attributed to solute enhanced recombination [7,40]. There is also substantial experimental evidence for dose rate effects at high flux, characteristic of highly accelerated test reactor irradiations [3,11,16,41]. This regime is believed to begin above 10^{12} n/cm^2-s at 290°C due to a increasing concentration of UMD sinks. The presence of such vacancy cluster-complexes (naonovoids) has been demonstrated in model alloys by both small angle neutron scattering (SANS) and positron annihilation (PAS) studies [42-45]. In more complex alloys, solutes like Mn, Ni, P, Si segregate to the cascade vacancy cluster-complexes that contain few vacancies. Higher sink densities reduce D* delaying the precipitation of CRP and SMF.

In summary, dose rate effects are expected to occur over a wide range of ϕ due to the combination of thermal contributions to Cu diffusion at very low dose rates, solute enhanced recombination at intermediate dose rates and cascade cluster recombination at the highest dose rates. This is schematically illustrated in the plot of the ϕt need to produce a specified $\Delta\sigma_y$ (taken as 50% of the plateau) or ΔT from CRPs versus ϕ shown in Figure 2b.

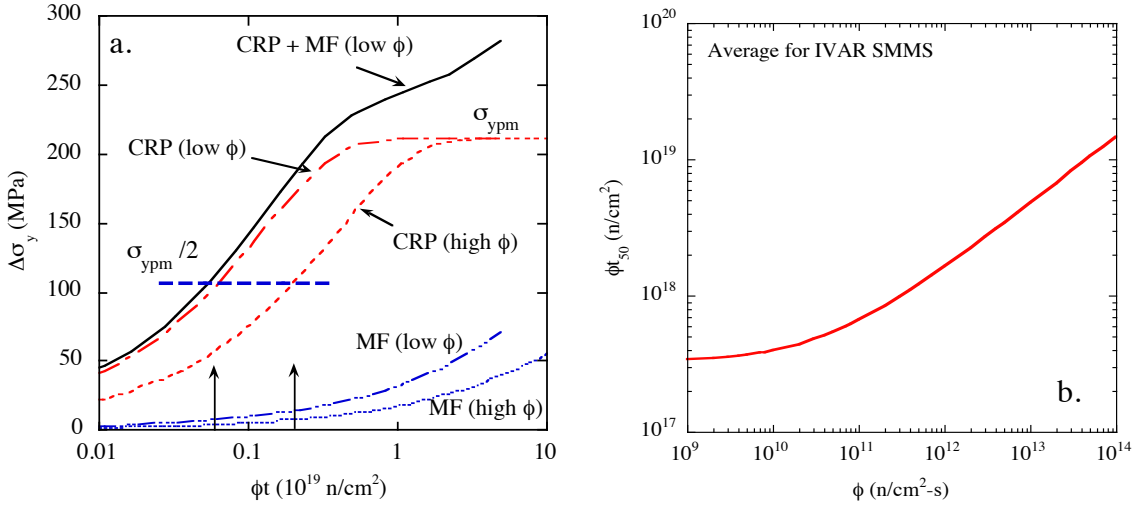

Figure 2,1 a) A schematic illustration of the CRP plus MF model of irradiation hardening and embrittlement. Here $\phi_{tpm/2}$, the fluence needed to produce 1/2 of the maximum CRP hardening, σ_{ypm}, shifts to higher with increasing flux; b) ϕt need to produce a specified $\Delta\sigma_y$ (taken as 50% of the plateau) or ΔT from CRPs versus ϕ.

Section 3. Physically based RPV embrittlement prediction models

3.1 Dose Rate Effect, Radiation Enhanced Diffusion and Precipitation Models - Two Feature Solute Trap Enhanced Recombination Model (2FM)

In this section we describe a physically based embrittlement model that also considers two hardening features, namely SMF and CRP. This two-feature model (2FM) is applicable to fluence levels expected in the currently planned reactor lifetime and flux levels of up to 10^{12} n/cm^2-s. The model assumes that dose rate effects are soley due to the flux dependence of RED, in terms of $D^*(\phi)$. The $D^*(\phi)$ is used in simple precipitation models. D^* depends on the steady-state vacancy concentration (molar or atom fraction) X_v as a function of flux, sink density, temperature and solute trap concentration. The relation between D^* and the increase in the CRP volume fraction (f_p) as a function of and fluence is expressed in terms of simple Avrami-type transformation model. A corresponding relation between hardening and $\sqrt{f_p}$ in Avrami-type expressions is to model the corresponding CRP contribution to $\Delta\sigma_p(\phi t)$. The SMF contribition is treated in a semi-empirical fashion as

$$\Delta\sigma_m(\phi t) = CF_m\sqrt{\phi t_e} \qquad (3.1)$$

Here CF_m is a SMF chemistry factor found by fitting the low Cu IVAR data that depnds on Ni, Mn, Si, Cu, P and C.

<u>Rate Theory Models of Defect Concentrations and Recombination</u>: At steady state, X_v is established by defect conservation balances describing vacancy production, transport and fate. Vacancy fates include clustering, annihilation at sinks and recombination with SIAs.

The dominant sinks are dislocations, incoherent boundaries and defect clusters. Note vacancies and SIAs can also be temporarily trapped at solutes and coherent interfaces, but they ultimately suffer one of the ultimate fates described above. We assume three-dimensional (3D) diffusion of all mobile defects, which is the basis of classical rate theory [46]. While some one-dimensional motion of interstitial clusters may occur, the use of more complex models is not warranted since our main objective is to gain insight from analysis of the large IVAR database. Classical rate theory is very consistent with a wide variety of data trends.

The primary vacancy and SIA sinks are spherical clusters and network dislocations. For 3D diffusion, the sink strength of clusters is $Z_c \approx 4\pi C_c r_c$, where C_c and r_c are the cluster concentration (or number density $C_c = X_c/\Omega_a$, where Ω_a is the atomic volume) and radius respectively. The sink strength of dislocations, with a cylindrical capture radius, is $Z_c \approx Z\rho$, where ρ is the dislocation density and $Z \approx 1$ is a geometric factor that depends weakly on ρ and is larger for SIA than vacancies due to their stronger mutual strain field interaction. Small SIA dislocation loops can be approximated as spherical clusters. Note in this analysis we also neglect sink 'bias' that leads to a preferential flow of SIAs to dislocations, leaving an excess flux of vacancies to accumulate at other sinks. These expressions also assume that the sinks easily absorb any defect that arrives at their capture radius. However, if local effects retard defect absorption, an additional modification is needed that reduces the sink efficiency. For example, dislocation sink efficiency is lower in the absence of jogs, which are easy sites for vacancy and SIA absorption. Further, the $Z_d \approx \rho$ approximation assumes a geometrically ordered arrangement of well-spaced individual dislocations. Thus, the effects of both actual sink efficiency and geometry of the complex dislocation structures found in structural alloys may reduce the effective Z_d to significantly less than ρ. The total sink strength (Z_t) is approximately the sum of the spherical sinks, like UMD cascade vacancy clusters, and dislocation sink strengths.

It is convenient to express X_v in terms of the fraction of vacancies and SIA that escape recombination and reach fixed sinks (g_s).

$$X_v = [g_s(T, \phi, Z_t)\, \xi\phi\sigma_{dpa}]/[D_v S_t] \tag{3.2a}$$

Here σ_{dpa} is the dpa cross section, ξ is the fraction of vacancies created per dpa and D_v is the vacancy diffusion coefficient ($<< D_i$, the interstitial diffusion coefficient). When recombination is only between vacancies and SIAs that diffuse freely through the matrix are considered,

$$g_{sm} = [2/\eta][(1 + \eta)^{1/2} - 1] \tag{3.2b}$$

$$\eta = 16\pi r_r \xi\phi\sigma_{dpa}/\Omega_a D_v Z_t^2 \tag{3.2c}$$

Here r_r is the recombination radius. Based on the nominal set of parameters (see reference 17 for details and sources) for Fe and, by inference, low alloy steels, given in Table 3.1, at 290°C, significant recombination, defined by $g_s = 0.5$, occurs at a flux > $3x10^{13}$ n/cm^2-s. Note the E_{vm} = 125 kJ/mole used in these calculations is an effective value for unalloyed, but slightly impure, Fe.

However, recombination is greatly enhanced if vacancies are strongly bound to a high concentration (X_t) of solute trapping sites. Assuming that a solute trap is limited to one bound vacancy, a small fraction of traps are occupied ($X_t >> X_{tv}$) and noting that $D_vC_v = D_iC_i$, the approximate steady-state defect balance equations are

$$\xi\phi\sigma_{dpa} + X_{tv}/\tau_t - D_vX_v[Z_t + 4\pi(r_tX_{tv} + r_rX_v)/\Omega_a] = 0 \quad (3.3a)$$

$$D_vX_v4\pi r_tX_t/\Omega_a - X_{tv}/\tau_t - D_vX_v4\pi r_tX_{tv}/\Omega_a = 0 \quad (3.3b)$$

$$\tau_t \approx b^2/[D_v\exp(-H_b/RT)] \quad (3.3c)$$

Here, r_t ($\approx r_c$) is the trap capture radius, τ_t is the average trapping time, H_b is the trap-vacancy binding energy (or more formally enthalpy) and b is the atomic spacing. Solute vacancy binding energies are typically in the range of about 5 to 30 kJ/mole [47]. However, for reasons discussed below, the effective H_b may be even higher. In cases with significant trapping and $X_{tv} >> X_v$, Equation 3.3 can be solved for the flux corresponding to a specified $g_{st}(\phi, T_i, S_t, X_t, r_t, H_b)$ as

$$\phi(g_{st}) = [\ (1/g_s - 1)\Omega_aZ_t/(4\pi r_t\tau_t)]/[\sigma_v4\pi r_tg_s/(\Omega_aZ_t)C_t + (g_s - 1)] \quad (3.3d)$$

Recombination can also occur at multiple vacancy trapping sites, including at coherent precipitate interfaces. Trapping at small solute cluster complexes may be particularly important, since the binding energies of additional vacancies are relatively large. For example, based on the capillary approximation and assuming vacancy formation energy of 175 kJ/mole and surface energy of 1.5 J/m^2, the binding energy increases from about 28kJ/mole for a di-vacancy to about 70 kJ/mole for a 5 vacancy cluster. Further, as noted above, Z_t may be less the actual dislocation density, ρ, leading to additional recombination and lower g_s. These (and other) effects can be treated by more detailed rate theory models. However, they can be accounted for approximately by treating H_b, Z_t and X_t as 'effective' parameters.

As discussed in Section 2, UMD are created directly in cascades and are thermally unstable, shrinking by vacancy emission with a characteristic annealing time τ_c [3,4,16,29,32,41,48]. The clusters build up to a steady-state concentration that is directly

proportional to the dose rate and formation cross section, σ_c. The cascade clusters act as vacancy and SIA sinks. The steady-state cluster sink strength is

$$Z_c \approx 4\pi r_c \sigma_c \phi \tau_c / \Omega_a \tag{3.4a}$$

Neglecting other recombination processes g_{sc} is given by

$$g_{sc} = Z_t / [Z_t + Z_c] \tag{3.4b}$$

Table 3.1 Parameters Used in Recombination Models

Parameter	Value
r_c & r_t	0.57 nm
σ_{dpa}	$1.5\text{x}10^{-22}$ cm^2
ξ	0.4
D_v	0.5exp(125,000/RT) cm^2/s
H_b (base)	30 kJ/mole
Z_t (base)	$2\text{x}10^{10}$ cm^{-2}
Ω_a	$1.17\text{x}10^{-24}$ cm^3
b	0.248 nm
X_t (base)	0.03
σ_c	$1\text{x}10^{-24}$ cm^2
τ_c	$3\text{x}10^5$ s

The effects of solute trap and cascade cluster recombination act together to reduce g_s as

$$g_s \approx g_{st} g_{sc} \tag{3.4c}$$

Low temperature (290 and 350°C) post-irradiation annealing studies have suggested $\tau_c \approx 3\text{x}10^5$s and $\sigma_c = 10^{-24}$ cm^2 at T_i = 290°C [3,4,16,29,32,41,48]. Figure 3.1a plots the corresponding g_s versus flux for the nominal parameters given in Table 1 and X_t = 0.03 and H_b = 30 kJ/mole. The g_s transitions between dose rate-independent, sink dominated regime at very low ϕ, though a solute trap recombination dominated regime at intermediate flux ϕ, to a cascade cluster dominated regime at high ϕ. Figure 3.1b plots the corresponding ϕ at g_s = 0.5 as a function of H_b for various S_t and X_t. These results

clearly indicate that solute enhanced recombination is likely to be important over a wide range of dose rates pertinent to RPV embrittlement. Note lower values of S_t and larger values of τ_c and σ_c would also expand the dose rate regime for significant cascade cluster recombination.

In summary, rate theory models show that a variety of recombination processes result in steady-state defect concentrations (or defect fluxes) that are strong functions of dose rate (and irrdiation temperature) over a very wide range of conditions pertinent to RPV steel embrittlement. Thus, it would actually be surprising if dose rate effects on $\Delta\sigma_y$ and ΔT were not observed. The effects of dose rate can be treated in terms of simple models that evaluate the fraction of defects that reach sinks, g_s.

Radiation Enhanced Solute Diffusion Models: We consider D* for Cu, assuming other solutes behave in a qualitatively similar manner. One simple approach is to scale the thermal D_{cu} by the total vacancy supersaturation (X_v/X_{ve}), where X_{ve} is the equilibrium vacancy concentration, as $D^* = D_{cu}X_v/X_{ve}$. However, both D_{cu} and X_{ve} are uncertain, particularly when extrapolated to low T_i, compounding the large uncertainty in X_v itself. A better approach is to use the ratio of the solute to self-diffusion coefficient D_{cu}/D_{sd}, and the estimated radiation enhanced self-diffusion coefficient which is approximately the vacancy flux, as $D_{sd}^* \approx D_vX_v$, thus

$$D^* \approx [D_vX_v][D_{cu}/D_{sd}] + D_{cu} \approx [g_s\,\xi\sigma_{dpa}\phi/Z_t][D_{cu}/D_{sd}] + D_{cu} \approx K(\phi,T)\phi + D_{cu} \qquad (3.5)$$

Here $K(\phi,T) = g_s[D_{cu}/D_{sd}]\xi\sigma_{dpa}/Z_t$ is the RED factor and D_{cu} accounts for thermal Cu diffusion. The maximum RED factor $K_m \neq f(\phi,T_i)$ is given by Equation 3.5 with $g_s = 1$. Empirical evaluations of D_{cu}/D_{sd} also require extrapolations to low T_i, but this is less significant than the other extrapolation uncertainties noted above. Using a lower-bound estimate of $D_{cu}(0.27\%Cu)/D_{sd} \approx 5$ at 290°C [32] and the nominal values in Table 3.1, yields $K_m \approx 1.5\times10^{-31}cm^4$ for $g_s = 1$. Fits of $\Delta\sigma_P(\phi t)$ data (see below) suggests this D* estimate is reasonable, but may be low by factors of up to about 30 to 250. Such differences can be attributed to a combination of underestimates of D_{cu}/D_{sd} arising from strong solute-vacancy interactions and, perhaps, overestimates of the effective sink strength, S_t. Other effects, such as mobile cluster complexes, may also lead to higher D* and K_m.

In the recombination dominated regime, the effect of dose rate can be described by a simple scaling law as $K(\phi_r) = K(\phi_r)\sqrt{(\phi_r/\phi)}$, where $\sqrt{(\phi_r/\phi)}$ can be viewed as an acceleration factor (Q) for different dose rates relative to the reference flux (ϕ_r). Here we take $\phi_r = 3\times10^{11}$ n/cm^2-s. More generally the Q for a particular alloy is $g_s(\phi)/g_s(\phi_r) \approx (\phi_r/\phi)^p$. As illustrated in dose rate scaling exponent p varies continuously with increasing dose rate from p = 1 in the thermal diffusion regime at very low ϕ, through p = 0 if there is a sink dominated regime, to p = 1/2 at intermediate ϕ in a recombination dominated regime and finally to p = 1 again in the cascade cluster dominated regime. The most notable result is that at low irradiation temperature, diffusion rates of Cu (and other species) are greatly accelerated by irradiation. D* depends on both dose rate and irradiation temperature, due to their effects on g_s and the vacancy jump rates near a solute

atom. However, even if $g_s << 1$, deep in the recombination regime, large D* values are consistent with large values of $[D_{cu}/D_{sd}]$.

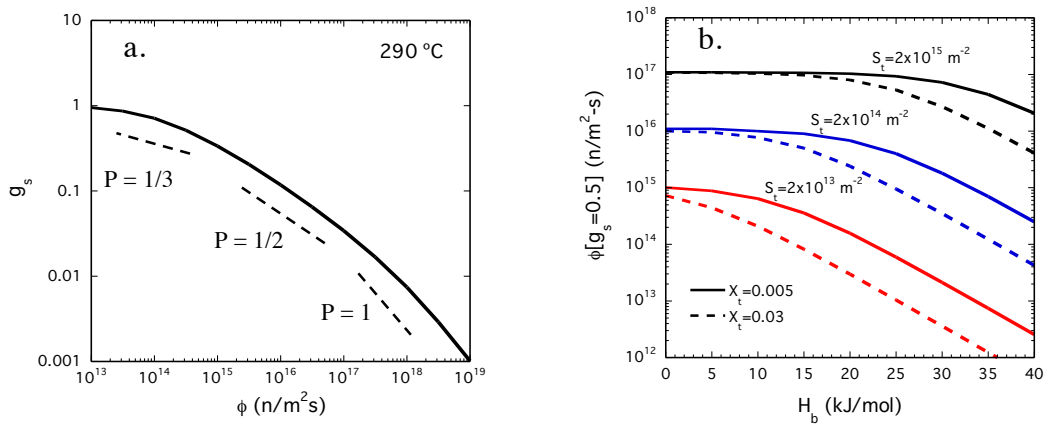

Figure 3.1 a) The decrease of g_s at 290°C showing the transition from sink to solute trap recombination to cascade cluster sink dominance of the fate of vacancies with increasing dose rate for the parameters in Table 3.1. b) The ϕ at $g_s = 0.5$ as a function of H_b for various S_t and X_t.

Copper Precipitation and Hardening Models: A very simple precipitation model that has been highly successful in rationalizing the effects of many embrittlement variables, including dose rate is now presented [3,4,16,52]. The model treats the growth of CRPs by long-range RED of Cu. The Mn and Ni in CRPs are assumed to arrive at a thermodynamically dictated rate that maintains the appropriate precipitate composition. This model does not treat precipitate nucleation or coarsening stages, and ignores the modest solubility of Cu in local equilibrium with CRP. The input variables to the growth model include D*, the concentration (number density) of precipitates (C_p), the amount of copper initially in solution (X_c) and the fraction of Cu in the precipitates (X_p) alloyed with Mn and Ni. Using an Avrami-type approximation to a more complex analytic integration of the diffusion controlled growth rate the volume fraction of the CRPs is given by [3,4,53]

$$f_p(\phi t) \approx [X_c/X_p]\theta(\phi t) \approx f_{pm}\{1 - \exp[-10.55C_p(X_c/X_p)^{1/2}(D^*t)^{3/2}]\} \quad (3.6a)$$

Here $\theta(\phi t) = \{1 - \exp[-10.55C_p(X_c/X_p)^{1/2}(D^*t)^{3/2}]\}$ and varies between 0 and 1 at 100% Cu precipitation. Assuming $K\phi >> D_{cu}$

$$f_p(\phi t) = \underline{f_{pm}}\{1 - \exp[-10.55C_p(X_c/X_p)^{1/2}(K\phi t)^{3/2}]\} \quad (3.6b)$$

Here $\underline{f_{pm}}$ is the maximum precipitate volume fraction at an equilibrium level of solute depletion, $f_{pm} \approx [X_c/X_p]$. The corresponding expression for fitting the $\Delta\sigma_y$ database is given by

$$\Delta\sigma_p(\phi t) = \Delta\sigma_y(\phi t) - CF_m\sqrt{\phi t} = \boldsymbol{\Delta\sigma_{ypm}}\sqrt{\theta} \tag{3.6c}$$

Here $\boldsymbol{\Delta\sigma_{\underline{ypm}}}$ is the maximum or plateau CRP contribution ($\Delta\sigma_{yp}$) to $\Delta\sigma_y$ and CF_m is the coefficient (empirical) for the MF hardening contribution. The CF_m for a Cu-bearing alloy is based on the $\Delta\sigma_y$ in steels with the same nominal composition but with no Cu. These expression can be fit to $f_p(\phi t)$ and $\Delta\sigma_p(\phi t)$ to evaluate K using experimental measurements (e.g., by SANS) or models of C_p, X_c, X_p. However, more generally we can fit Equation 3.5c with an expression θ as a function of an effective ϕt (ϕt_e)

$$\theta(\phi t_e) \approx (1 - \exp[-(F\phi t_e)^{3/2}) = (1 - \exp[-(\phi t_e/\phi t_{e80})]^{3/2}) \tag{3.6d}$$

$$F\ (=1/\phi t_{e80}) = (10.55C_p)^{2/3}(X_c/X_p)^{1/3}K(\phi_r) \tag{3.6e}$$

$$\phi t_e = \phi t[g_s(\phi)/g_s(\phi_r)] \tag{3.6f}$$

$$g_s = \frac{2}{\eta}\left(\sqrt{1+\eta} - 1\right) \tag{3.6g}$$

$$\eta = \left(\frac{\xi\sigma_{dpa}}{S_t^*}\right)\left\{\left(\frac{4\pi r_t\tau_t}{\Omega_a}\right) + \left(\frac{4\pi r_r}{\Omega_a D_v S_t^*}\right) + \left(\frac{4\pi r_t X_t}{\Omega_a S_t^*}\right)\left(\frac{4\pi r_t\tau_t}{\Omega_a}\right)\right\}\phi = L\phi \tag{3.6h}$$

A least square procedure optimizes the fit parameters F, L, f_{pm}, $\Delta\sigma_{ypm}$. The parameter F sets the ϕt_e-range for CRP evolution in a particular alloy, so that 80% of CRP hardening attained when the effective fluence, $\phi t_e = 1/F$, so we redefined this as $\boldsymbol{\phi t_{e80}}$. The parameter L sets the scale for recombination. Large L, hence η, correspond to low values of g_s, and p, approaching the recombination dominated limit of 1/2. If C_p, X_c and X_p are known

$$K(\phi_r) = 1/[(10.55C_p)^{2/3}(X_c/X_p)^{1/3}\ \phi t_{e80}] \tag{3.6i}$$

The maximum K without recombination (K_m) at $g_s = 1$ is

$$K_m = K(\phi_r)/g_s(L\phi_r) \tag{3.6j}$$

Equations 3.6 are based on approximations of the physics governing precipitation and hardening under irradiation. For example, it is well established that precipitation kinetics

involve overlapping regimes of nucleation, growth and coarsening that are not reflected in the simple diffusion controlled growth model. And Equation 3.5c does not fully account for the fact that, in addition to $\sqrt{f_p}$, $\Delta\sigma_{yp}$ also depends on the size, composition and structure of the CRPs, as well as how their individual hardening contribution combines, or superimposes, with that due to pre-existing obstacles to dislocation slip.

A Generalized Avrami-Type Model: Equation 3.6d can be expressed in a more general Avrami-type form as

$$\theta(\phi t_e) \approx \{1 - \exp[-(\phi t_e/\phi t_{e80})^{\beta}]\} \tag{3.7a}$$

Here, the additional fit parameter, β, can deviate from the nominal value of 3/2 appropriate to simple diffusion controlled growth and hardening as described by Equation 5c. Fitting β can partially account for both deviations from simple diffusion controlled growth and the complexities of the relationship between f_p and $\Delta\sigma_{yp}$. For $\beta \neq 3/2$ Equation 3.6i is modified as

$$K(\phi_r) = 1/[(10.55C_p)^{2\beta/3}(X_c/X_p)^{\beta/3}\,\phi t_{e80}] \tag{3.7b}$$

Equations 3.6 and 3.7 provide a general framework to analyze the $\Delta\sigma_p$ database. This has been done previously for individual alloys [7,8,40]. In the next section we develop expressions to fit the IVAR datbase for split melt alloys

3.2 Chemistry Factor Fitting Model for 2FM

In this section we describe fitting functions of the chemistry effects in hardening that we derived from IVAR $\Delta\sigma_y$ database. The total irradiation hardening, $\Delta\sigma_y$, down due to stable matrix feature (SMF) hardening, $\Delta\sigma_m$, and a copper rich precipitate (CRP) hardening, $\Delta\sigma_p$, is given by,

$$\Delta\sigma_y = \Delta\sigma_m + \Delta\sigma_p \tag{3.8}$$

The SMF hardening $\Delta\sigma_m$ is given by,

$$\Delta\sigma_m = CF_m\sqrt{\phi t_e} \tag{3.9a}$$

Here, CF_m is a function of Cu, Ni, Mn, P, Si and C as fitted to the low Cu IVAR data as shown in Section 4.1.

The CRP hardening, $\Delta\sigma_p$, term is given by,

$$\Delta\sigma_p = \Delta\sigma_{pm}[1 - \exp\{-(\phi t_e/\phi t_{e80})^{\beta}\}]^{1/2} \quad (3.9b)$$

Here, $\Delta\sigma_{pm}$ is a saturation CRP hardening, ϕt_e is the effective fluence at $\Delta\sigma_p = 0.8\Delta\sigma_{pm}$, and β sets the transient behavior shape slightly adjusted from the base diffusion control growth model with $\beta = 3/2$, as is illustrated in Figure 3.2. The effective fluence concept was described previously. It can be obtained by fitting the parmeter L for individual alloys irradiated over a range of flux and fluence to collapse the data into one hardening trend curve:

$$\phi t_e = \phi t\left[L\phi_r\left(\sqrt{1+L\phi}-1\right)\right]\Big/\left[L\phi\left(\sqrt{1+L\phi_r}-1\right)\right] \quad (3.9c)$$

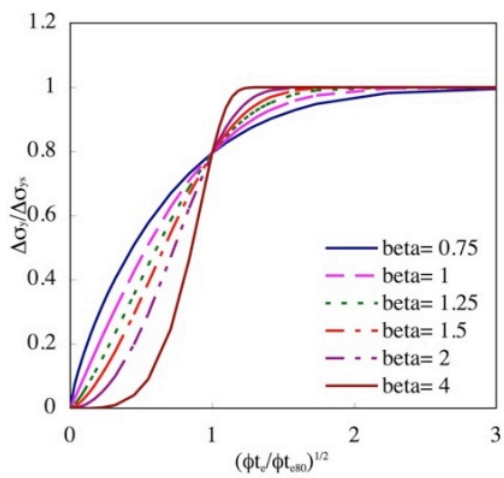

Figure 3.2 The effect of b on the shape of the pre-plateau precipitation Avrami curve.

Figure 3.3 shows an example of the fluence to effective fluence, ϕt to ϕt_e, conversion for a 0.4%Cu-1.3%Ni-1.4%Mn alloy (LD) irradiated at 290ºC and three different flux ranges shown by the different symbols. The solid and dashed lines are based on fits to $\Delta\sigma_{pm}$, L. ϕt_e and β. Figure 3.3a plots $\Delta\sigma_y$ on the actual fluence-scale clearly showing the delay of hardening at higher flux, while the $\Delta\sigma_y$ collapses on a single curve on the effective fluence scale in Figure 3.3b. The flux effect is even more clearly shown in the corresponding residual plots shown in Figure 3.3c and d, where measured $\Delta\sigma_y$ minus fit curve residuals are plotted as a function of flux.

The chemistry factor fits for $\Delta\sigma_{yp}$ were based on the split melt plate steels in IVAR database. First single variable subsets of alloys were grouped to analyze an effect of Cu, Mn and Ni. For example, a subset of alloys with 0.11, 0.22, 0.34 and 0.42%Cu, alloys with about 0.8%Ni and 1.5%Mn isolates Cu effects. Another subset of alloys with 0.0,

0.2, 0.8 and 1.25%Ni with 0.4%Cu and 1.4%Mn, isolates Ni effects. The fitting forms $\Delta\sigma_{pm}$, ϕt_{e80}, and β were motivated by cross plots of the $\Delta\sigma_p$ data. The fitting forms are

$$\Delta\sigma_{pm} = \left(k_{Ni}Ni + k_{Mn}Mn + k_o\right)\left[1 - \exp\left\{-\left(\frac{Cu - Cu_{min}}{Cu_0}\right)^m\right\}\right] \tag{3.10a}$$

$$\phi t_{e80} = \frac{k_{a,Ni}Ni + k_{ao}}{Cu - Cu_{min}} + k_{b,Ni}Ni + k_{b,Mn}Mn + k_o \tag{3.10b}$$

$$\beta = k_{b,Cu}Cu + k_{b,Ni}Ni + k_{b,Mn}Mn + k_0 \tag{3.10c}$$

Here, k_{Ni}, k_{Mn}, k_o, Cu_{min}, Cu_0, m, $k_{a,Ni}$, k_{ao}, $k_{b,Ni}$, $k_{b,Mn}$, k_o, $k_{\beta,Cu}$, $k_{\beta,Ni}$, $k_{\beta,Mn}$, and $k_{\beta 0}$ are the fit coeffients. The first fit was to the values of $\Delta\sigma_{pm}$, ϕt_e and β for individual alloys. The coeficients then refined to minimize the least square error for all of the $\Delta\sigma_p$ data. Note, these fits were performed on data already on a ϕt_e-scale. The chemistry dependent L parameter for the ϕt_e conversion was based on fits to the alloys as reported in [40]. The g_s dependency can be separately formulated in our future analysis to combine with the 2F $\Delta\sigma_y$ model that we focus in this project. Further details of the analyses will be shown in the results section.

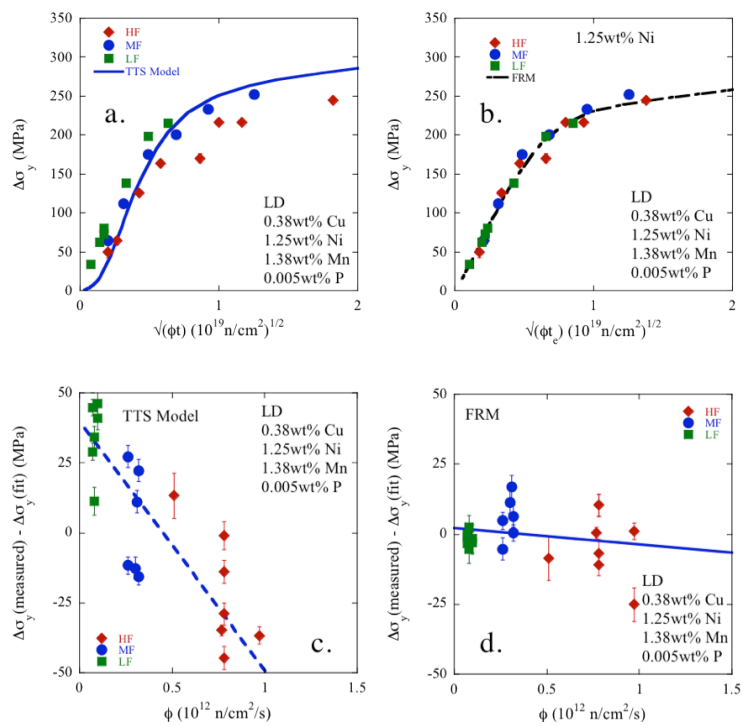

Figure 3.3 (a) TTS model predictions and data for the 290°C IVAR $\Delta\sigma_y$ data for SMMS LD alloy with 0.4 wt % Cu, 1.4 wt % Mn, and 1.25 wt % Ni on an actual fluence, ϕt, scale; (b) The fitted recombination model predictions for an effective fluence, ϕt_e, scale; (c,d) the corresponding measured minus predicted residuals for the models, showing the residuals on the ϕt_e scale are well centered and approximately independent of flux.

3.3 Three-feature model (3FM) with additional UMD hardening and sinks – historical background

The following background section outlines a 3FM developed in the 1990's to treat the effects of high flux test reactor irradiations. What is reported here preceeded the current program. Considerable work has gone into updating the 3FM that is described in Section 4, below.

In the high flux regime for some test reactor irradiations, UMD may contribute to be an important embrittlement feature. UMD continuously form and dissolve (anneal) under irradiation [3,29,41,48,50,54]. Mader and Odette showed that UMD play two roles [41,48]. First, the UMD directly contribute to irradiation hardening and embrittlement. However, the UMD also act as defect sinks that destroy vacancies, thereby decreasing the efficiency of RED. The effect of decreased RED efficiency is to delay (shift to higher fluence) the CRP and, presumably, SMF contributions to hardening and embrittlement. The dose rate scaling exponent p also approaches 1 in the UMD sink-dominated regime. *As a result of the dual role played by UMDs, increasing flux can increase, decrease, or leave unaffected hardening and embrittlement, depending on the alloy composition, irradiation temperature, flux, and fluence.*

Mader and Odette estimated the balance of the various hardening features empirically based on post-irradiation annealing (PIA) microhardness (ΔH) recovery measurements [41,48]. The underlying principle is that each of the three types (UMD, SMF, and CRP) of hardening features has a reasonably unique temperature (T_a)-time (t_a) thermal annealing signature. The UMDs are the least thermally stable and can recover in situ over the times characteristic of a high-flux irradiation. At sufficiently high fluence the UMD reach a steady-state concentration that varies in proportion to the flux. SMF accumulate in rough proportion to fluence in both low-Cu and Cu-bearing alloys. SMF do not recover under irradiation but do anneal to some extent at temperatures gewater than about 50°C higher than the nominal irradiation temperature of 290°C. The CRP are much more thermally stable than either UMD or SMF and require annealing temperatures above about 400°C for significant recovery in periods less than several hundred hours.

Very extensive annealing studies [41,48] led to estimates of the UMD recovery times, $\tau_{umd} \approx 3.25 \times 10^5$ s (150 h) and $\tau_{umd} \approx 1.8 \times 10^4$ s (5 h) at 290°C and 343°C, respectively. These values are consistent with theoretical estimates of the time for the dissolution of a small vacancy-solute cluster complex [48]. The formal definitions used in the Mader and Odette studies to experimentally determine ΔH_{umd}, ΔH_{smf}, and ΔH_{crp} are shown in Table 3.2 and are schematically illustrated in Fig. 3.4. Here the ΔH_a and ΔH_r are the decrease in microhardness at the specified annealing conditions, and the residual hardening in very low Cu steels at 343°C and 150 h (3.25×10^5s), respectively. The effects of variables such as Ni, irradiation temperature, flux, and fluence on the hardening contributions of the UMD, SMF and CRP were estimated by the PIA measurements on specimens with corresponding variations in composition or irradiation condition. The effect of flux is most pertinent to this discussion because the number density of UMD (N_{umd}) scales in direct proportion to dose rate and the hardening scales in proportion to the square root of their number density.

Table 3.2 Procedure used to define the UMD, MD and CRP contributions to the total irradiation hardening

Feature ΔH	T_a,t_a Definition of the ΔH Feature Contribution
ΔH_{umd}	$-\Delta H_a$(343°C,5h) and $-\Delta H_a$(290°C,150h)
$\Delta H_{sm(smd)}$	$-\Delta H_a$(343°C,150h) + ΔH_r(343°C,150h, low Cu) $-\Delta H_{umd}$
ΔH_{crp}	$-\Delta H_r$(343°C,150h) + ΔH_r(343°C,150h, low Cu)

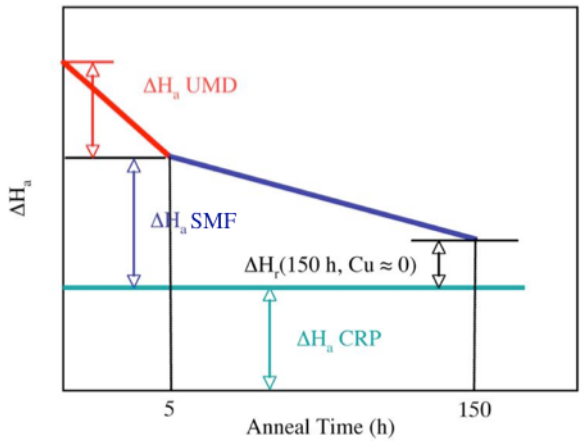

Fig. 3.4 Schematic illustration of the annealing signature procedure used to define the UMD, SMF and CRP hardening contributions (see Table 3.1).

The effect of flux on the balance of hardening contributions is illustrated in Fig. 3.5, which shows the recovery of microhardness as a function of time for 343°C anneals of Cu-bearing steels irradiated at different flux levels [41,48]. Clearly, the recovery for the high-flux irradiations at 343°C and 1.8×10^4 s (5 h) is much larger than for the corresponding low-flux irradiations. Figure 3.6 plots the individual and combined contributions of CRP, SMF, and UMD that were empirically estimated for the high ≈ 0.3% Cu alloys, based on their respective low-temperature 290 and 343°C thermal annealing signatures, as described above. Figure 3.6 shows that the CRP and SMF terms decrease with increasing flux while the UMD term increases. Notably, while the balance of defects changes, *the overall hardening is relatively insensitive to flux*. The UMD contribution to hardening also increases with decreasing temperature and increasing Ni, and, by inference, Mn and Cu content. At that time, the UMDs were believed to be small 5-30 vacancy clusters complexed with solutes, which increases their thermal stability and effectiveness as strengthening features. While positron annihilation studies have subsequently shown that such Cu-coated microvoids are indeed present in simple Fe-Cu model alloys, in complex steels (and even simple Fe-Mn model alloys), the UMDs and SMFs are not associated with clusters containing a significant number of vacancies [55-57].

This three-feature description of irradiation hardening and embrittlement is powerful but certainly approximate. In reality, there is not a sharp delineation between UMD, SMF and CRP, especially at high flux. Such features also implicitly interact with one another by mechanisms such as competition for finite numbers of solute atoms and excluded volume effects. Nevertheless, as shown in Figure 3.6, it is possible to independently approximate the balance of hardening from those features as a function of flux. The three-feature concept described above was used by Mader and Odette to develop a very successful PIA model. However, that concept can also be used to quantitatively model dose rate effects at high flux.

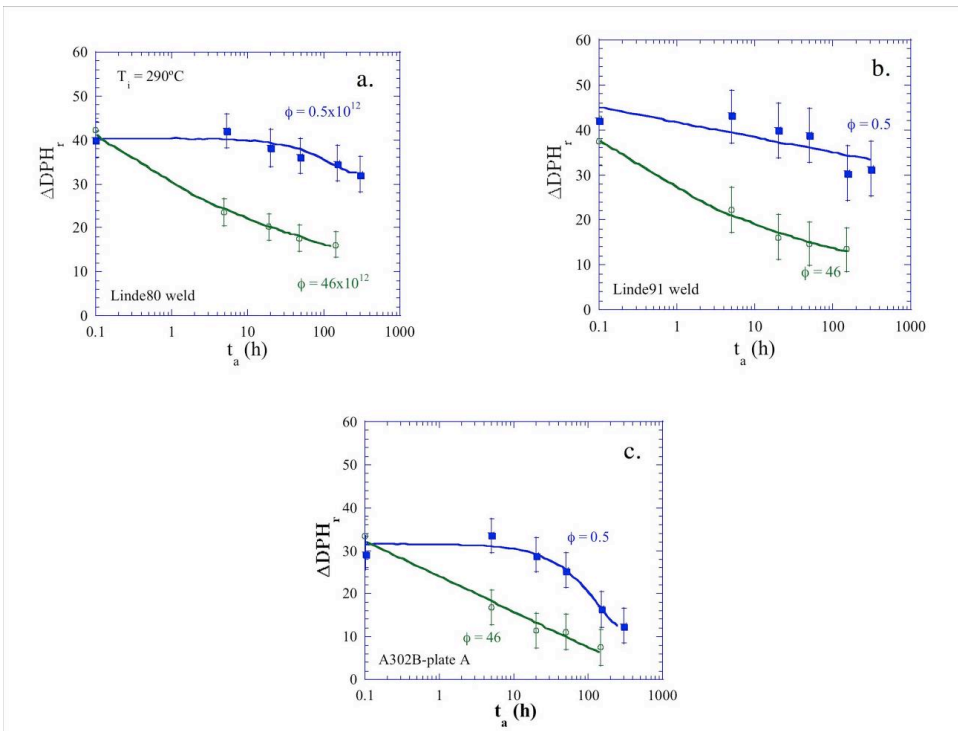

Fig. 3.5 The recovery of microhardness ΔH (ΔDPH, kg/mm^2) as a function of time during a annealing at 343°C for three alloys (two welds and one plate) irradiated at fluxes of 0.5×10^{12} and 46×10^{12} n/cm^2/s to a fluence of ~0.5×10^{19} n/cm^2. While the initial H are similar, the ΔH in the steels irradiated at high flux is much more rapid.

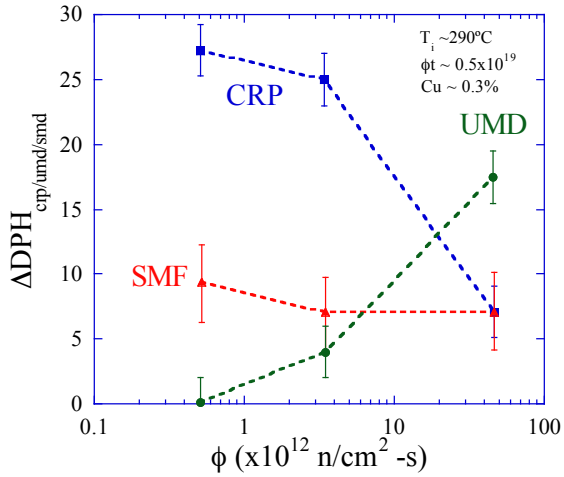

Fig. 3.6 The average microhardness contributions from copper-rich precipitates (CRPs), stable matrix features (SMFs), and unstable matrix defects (UMDs), for high copper (~0.3 wt %) alloys based on their respective low temperature 290 and 343°C thermal annealing signatures.

3.3.1 Previous 3FM

The number of UMD (N_{umd}) is governed by their generation rate (G_{umd}) and annealing time (τ_{umd}) as

$$dN_{umd}/dt = G_{umd} - N_{umd}/\tau_{umd} \qquad = \phi\sigma_{umd} - N_{umd}/\tau_{umd} \tag{3.11a}$$

Here σ_{umd} is the UMD formation cross section. Integration of this simple differential equation gives

$$N_{umd}(\phi, \phi t) = N_{umds}[1 - \exp(-\phi t/\phi\tau_{umd})] \tag{3.11b}$$

N_{umds} is the steady state number density of UMDs.

$$N_{umds} = \tau_{umd}G_{umd} = \phi\tau_{umd}\sigma_{umd} \tag{3.11c}$$

Since UMD hardening (ΔH_{umd}) approximately scales with the $\sqrt{N_{umd}}$, the corresponding fluence (ϕt) dependence of $[\Delta H_{umd}(\phi t)]$ is given by

$$\Delta H_{umd}(\phi t) = \Delta H_{ums}(\phi)\{\phi[1-\exp(\phi t/\phi\tau_{umd})]\}^{1/2} \tag{3.11d}$$

Here, $\Delta H_{ums}(\phi)$ is the saturation UMD hardening at a specified flux. Figure 3.7 shows the corresponding predictions of UMD ΔH as a function of fluence for a nominal 0.3% Cu alloy at 290°C and various dose rates based on the estimated values of ΔH at lower fluence and $\tau_{umd} = 3.25 \times 10^5$ s. Clearly, UMD hardening is minimal at low flux, but it builds up to a much higher value at high flux. The $\Delta H_{ums}(4.6x10^{13}$ n/cm^2) is ≈ 33 dph (kgf/mm^2). Assuming a conversion factor of 3.3 MPa/kg$_f$/mm^2 to convert hardness to yield stress increases and 0.7°C/MPa to convert the yield stress increase to a TTS, the corresponding saturation UMD TTS at 5x10^{13} n/cm^2 is ≈ 80°C.

The effect of the UMD on the RED diffusion coefficient D* was modeled crudely in terms of a UMD modified effective fluence, ϕt_{umd}. Note this treatment is not strictly correct, but is shown for historical reasons. For simplicity we applied the UMD effective fluence adjustment to ϕt_e at a flux greater than a minimum reference flux, ϕ_{ru}, as

$$\phi t_{umd} = \phi t_e[(1 + k)/(1 + k\phi/\phi_{ru})] \qquad \phi > \phi_{ru} \tag{3.12}$$

The ϕ_e accounts for any flux effects that are not due to UMD and the term in the brackets accounts for UMD sinks. Above the threshold flux of 10^{12} n/cm^2-s, the UMD reduce ϕt_{umd}. Table 3.3 summarizes the various regimes of flux effects mechanisms and their limiting p-scaling laws. The product of the RED coefficient and time, D*t, is a measure of the amount of precipitation at a specified fluence. Figure 3.8 shows an example of the predicted variation of an effective fluence factor $M_\phi = (\phi t_e \text{ or } \phi t_{umd})/\phi t$ with flux for k = 0.1. M_ϕ, which is normalized to 1 at 3x10^{11} n/cm^2-s, decreases with increasing flux due to the mechanisms described in Table 3.3.

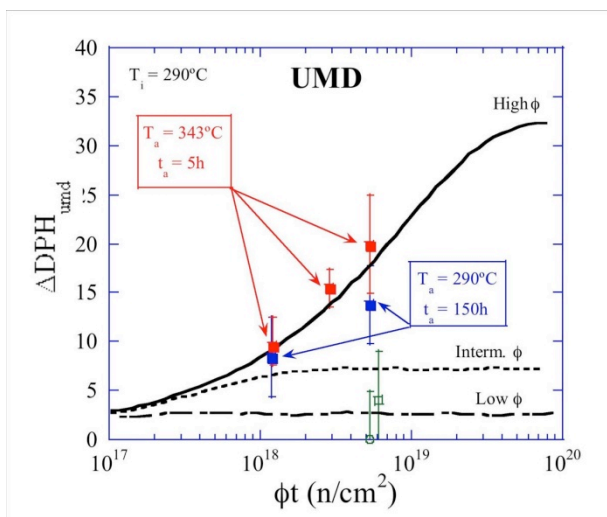

Figure 3.7 The predicted change in microhardness vs fluence for UMD for a nominal 0.3 wt % Cu alloy at 290°C and at low, intermediate, and high fluxes. The curves are based on a τ_{umd} =3.25 × 10^5 s and the estimates of UMD hardening over a range of lower fluences from 290°C-150 h and 343°C-5 h from annealing signatures.

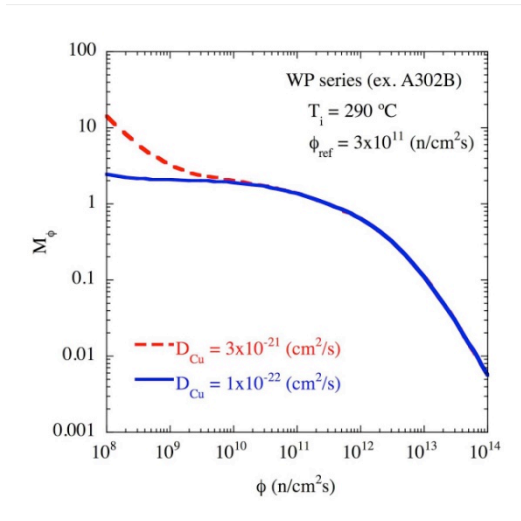

Figure 3.8 An example of the variation of the ratio of the effective fluence and UMD modified effective fluence (for $\phi > 10^{12}$ n/cm^2/s) to the actual fluence normalized to 1 at 3x10^{12} n/cm^2/s. Note this is shown for purposes of illustration only.

The concepts described above were used to develop a *three feature TTS* model (3FM), that is used to analyze subsets of the high-flux test reactor database complied by Kirk.

$$TTS = TTS_{md} + TTS_{crp} + TTS_{umd} \tag{3.13a}$$

The SMF and CRP contributions are calculated by using the ϕt_{eff} and ϕt_{umd} in the low flux EONY TTS model, assuming $\phi t_e = \phi t$ and the effect of flux, other than that due to the UMD, is represented in terms of its effect on the saturation fluence. The UMD contribution is based on Equation 3.11d as

$$TTS_{umd}(\phi t) = TTS_{urs}\{(\phi/[5 \times 10^{13}])[1\text{-}\exp(\phi t/\phi\tau_{umd})]\}^{1/2} \tag{3.13b}$$

Here TTS_{urs} is the saturation TTS contribution at ϕ = 5x10^{13} n/cm^2-s. As noted previously, at 290°C TTS_{urs} was estimated to be about ≈ 80°C for high-Cu steels. Thus, the saturation TTS_{umd} at other fluxes is given by

$$TTS_{umd}(\phi) = TTS_{urs}\sqrt{(\phi/[5 \times 10^{13}])} \tag{3.13c}$$

Note, in a number of cases in the test reactor data in the, the flux and fluence are directly proportional, since the irradiations are for a fixed time (t_{irr}) at different fluxes: $\phi t = \phi t_{irr}$. In this case the TTS_{umd} is simply

$$TTS_{umd} = TTS_{urs}\sqrt{[\phi t/(5 \times 10^{13} t_{irr})]} \quad (3.13d)$$

This trend is observed in a number of the data subsets.

Table 3.3 Flux dependence mechanisms, regimes and scaling laws for T_i = 290°C

Dominant mechanism	ϕ-regime (n/cm^2/s)	Limiting scaling p[a]	Comments[b]
Thermal diffusion assisted	$\phi < 10^{10}$	D*t @ $\phi t/\phi$	Depends on low-temperature D_{cu}. Thermal precipitation is observed in sensitive model alloys and sensitive steels at 290 to 350°C. This flux range is pertinent to BWR vessels and some low-flux surveillance capsules.
Solute trap recombination	$10^{13} > \phi > 10^{10}$	D*t @ $\phi t/\sqrt{\phi}$	Depends on alloy Ni & Mn contents, microstructure Pertinent to PWR surveillance capsules and test reactor irradiations as well as higher flux regions in PWR vessels and low fux test reactor irradiations.
Unstable matrix defect sinks	$\phi > 10^{13}$	D*t @ $\phi t/\phi$	Pertinent to materials test reactor irradiations and high flux

[a]The flux-scaling varies smoothly in transitions between regimes that are dominated by a specific mechanism that may overlap between some regimes.

[b]The flux levels at actual surveillance and vessel locations vary greatly, depending on the reactor type and details of the design and fuel assembly arrangements and surveillance capsule locations.

The τ_{umd}, k, and TTS_{uos} relate to the UMD annealing time, sink strength, and saturation hardening, respectively. The latter two parameters are for the specified reference flux ($5x10^{13}$ n/cm^2-s). In principle, they all can be related to physical quantities, such as vacancy binding energies and the self-diffusion coefficient in the case of τ_{umd}, for example. Indeed, such models have been developed by Mader and Odette [41,48] for irradiations around 290°C. However, detailed development of more general models is beyond the scope of this effort. Another approach would be to treat τ_{umd}, k, and TTS_{urs} as fitting parameters to establish the UMD contribution to the TTS at high flux as well as the corresponding effect on the fluence dependence of the SMF and CRP contributions. However, our initial application of the 3FM model revealed a practical problem related to a high degree of covariance between the fitting parameters; for example, the delay imposed by k in the MD and CRP TTS can trade off with the fluence dependence of the UMD contribution, which is controlled by τ_{umd}.

3.3.2 Previous Three Feature Model (3FM) Analyses of Selected Test Reactor Data

A large subset database compiled by Kirk for high fluence ETC analysis in 2007 has been analyed using the 3FM. The database included TTS and $\Delta\sigma_y$ data from the literature including for neutron irradiations to greater than $5x10^{19}$ n/cm^2. The data sources consisted of: 1) Test Reactor Embrittlement Data Base (TR-EDB) that included literature data before 1990 compiled by ORNL; 2) the IAEA Cooperative Research Project databases that have accrued since 1974; and, 3) other literature since 1990. However, the most important sources of data were: 4) $\Delta\sigma_y$ measurements from the UCSB IVAR program, for low to intermediate flux [7,8,40]; and, 5) the RADAMO database, for intermdiate to high flux compiled at the SCK laboratory in Begium [58]. The database included over 1100 individual TTS and/or $\Delta\sigma_y$ points; the latter were converted to TTS. Table 3.3 summarizes data sources with type of embrittlement measures and reactor types. More details of irradiation conditions and materials included in each data set can be found in [59]. Here we focus two program forgings (A508 and IAEA JRQ) and one weld (ORNL 73W) that have been irradiated in several programs, including both IVAR and Radamo.

The previos application of the 3FM was based on fixing τ_{umd} at a nominal value of $3.25x10^5$ s at 290°C and scaling it at other temperatures of 266 and 300°C by the activation energy corresponding to the ratio of $\tau_{umd}(343)/\tau_{umd}(290) = 30$ in the Mader-Odette stuy. The ratio gives $\tau_{umd}(300°C) = 1.63x10^5$ s and $\tau_{umd}(266°C) = 1.9 \times 10^6$ s, respectively. A k (at 290°C) = 0.1 was found to give a reasonable fit to some of the test reactor data at a nominal irradiation temperature of 290°C. Since at saturation k scales with τ_{umd}, the corresponding k (at 266°C) is 0.58 and k (at 300°C) is 0.05. This leaves TTS_{urs} as the only remaining fitting constant.

Figures 3.9 to 3.11 show three examples of the application of the 3FM to test reactor data. Figure 3.9 is for the 0.31% Cu 73W data at both high-flux (BR2-Radamo) and low-flux (IVAR) conditions. The high flux data are shown for both 266°C in Figure 3.9a and 300°C in Figure 3.9b. Here, we have adjusted the IVAR data at 290°C to the higher temperature using the 3FM. The solid red curves are the 3FM predictions at fluxes of 5 $5x10^{13}$ n/cm^2-s. The dashed blue line is the PREDB fitted Kirk model that is not modified for UMD sinks; the dashed green line is the UMD-modified effective fluence curve for the Kirk model SMF and CRP TTS contributions. The effect of the UMD sinks in shifting the SMF and CRP curves to higher fluence is clear, especially at the lower temperature. The short dashed purple line is the UMD contribution to the TTS. The small filled diamonds are the actual data for a range of irradiation conditions, and the open diamonds are the data adjusted by the model to the specified flux and temperature. The fitted TTS_{urs} are ≈ 180°C and ≈ 50°C at irradiation temperatures of 266°C and 300°C, respectively. The decrease in the TTS_{urs} with increasing temperature is not unexpected and is qualitatively consistent with the observations of Mader and Odette [41,48]. The interpolated TTS_{urs} to an irradiation temperature of 290°C is ≈ 89°C which is only slightly higher than the previous estimate for such high-Cu alloys of ≈ 80°C. Figure 3.9c shows that the corresponding 3FTM prediction at a low flux of 5×10^{10} n/cm^2/s, with a minimal contribution from the UMD, is also in good agreement with the adjusted TTS data.

Figure 3.10 shows a similar plot for a low 0.05% Cu A508 forging. The TTS_{urs} are 84°C, 63°C, and 23°C at irradiation temperatures of 266°C, 290°C, and 300°C, respectively. The TTS_{urs} are lower than those for 73W, probably reflecting the low ≈0.05% Cu content of that alloy. In this case the adjusted data show a large amount of scatter around the predicted TTS curve at 290°C, and at both low and high flux, but the absolute values of the shifts are small.

Figure 3.11 shows similar plots for the intermediate 0.14% Cu JRQ plate at three irradiation temperatures for the RADAMO and IVAR databases, again over a wide range of flux. The TTS_{urs} again decrease with increasing temperature with values of 145°C, 87°C, and 52°C at irradiation temperatures of 266°C, 288°C and 300°C, respectively. The intermediate Cu JRQ plate falls between the low-Cu A508 and the high-Cu 73W. The 3FTM predictions at low flux are again consistent with the adjusted TTS data.

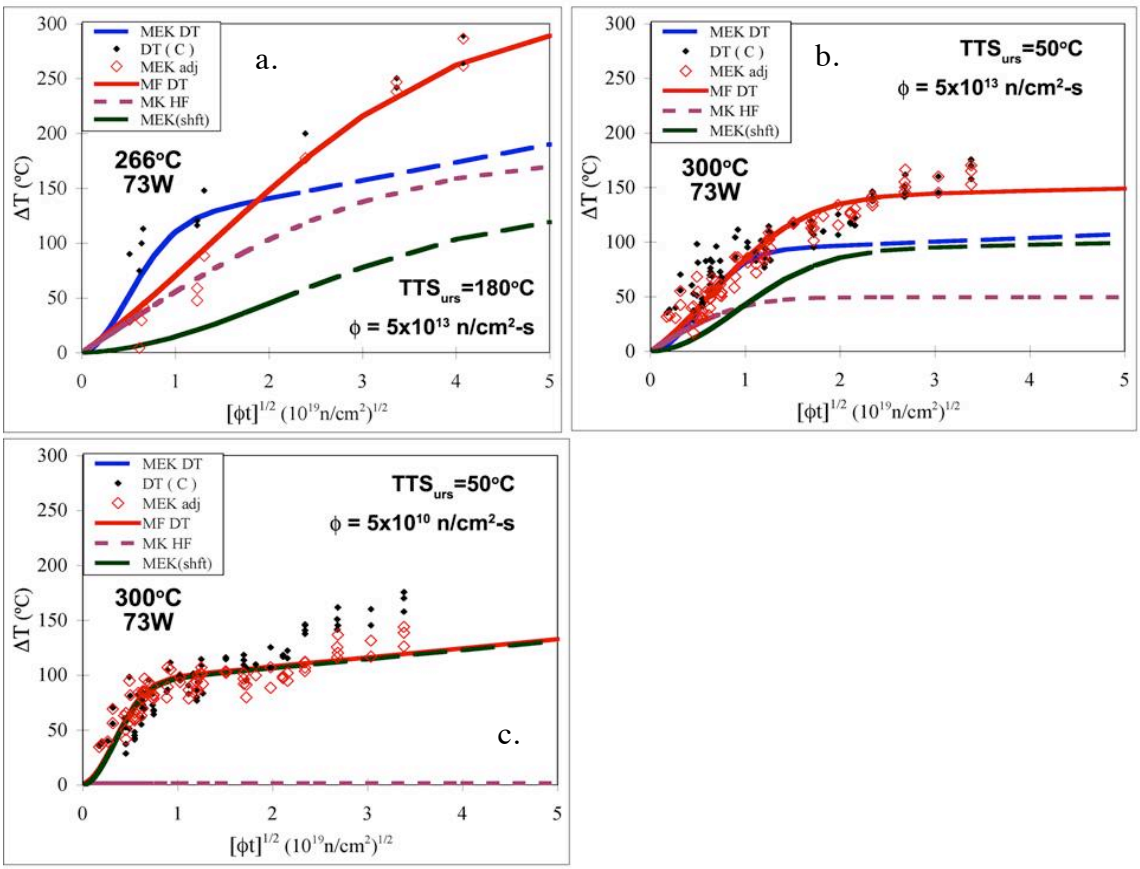

Figure 3.9 The 3FM predictions vs the sqrt fluence for the high 0.31 wt % Cu HSSI Weld 73W at high flux ($5x10^{13}$ n/cm^2/s) at both nominal temperatures of 511 and 572°F (266 and 300°C). The predictions for low flux ($5x10^{10}$ n/cm^2/s) at 300°C are also shown. The open diamonds are the data adjusted to the reference conditions by the 3FM.

Figure 3.12 plots the TTS_{urs} for the three alloys and nominal irradiation temperatures, showing the systematic trends in Cu and irradiation temperature described above. We have applied the 3FM mny other the alloys and high-flux irradiation conditions; in the other cases we examined, the results were generally similar to those illustrated in

Figs. 3.9 to 3.11. Extension of the 3FM approach to a *general* TTS model encompassing the entire range of flux, irradiation temperature, and alloy chemistry is an objective of the program reported here.

For the present purposes, the most important conclusion is that including a UMD TTS contribution in the 3FM rationalizes most of the high-flux TTS data in Appendix G up to relatively high fluence. Further, at low flux the 3FTTS model provides reasonable predictions of the adjusted TTS up to about 6×10^{19} n/cm^2 or more. However, we do not claim that the very simple 3FTTS model fully represents all the physics of embrittlement at high flux and fluence. Indeed, it almost certainly does not. However, the 3FTTS model does have a solid and *independent* physical basis. Most importantly, *the model can be tested* by future low-temperature (e.g., 290 to 350°C) annealing studies of a large number of RPV alloys that we have included in both IVAR and BR2 irradiations.

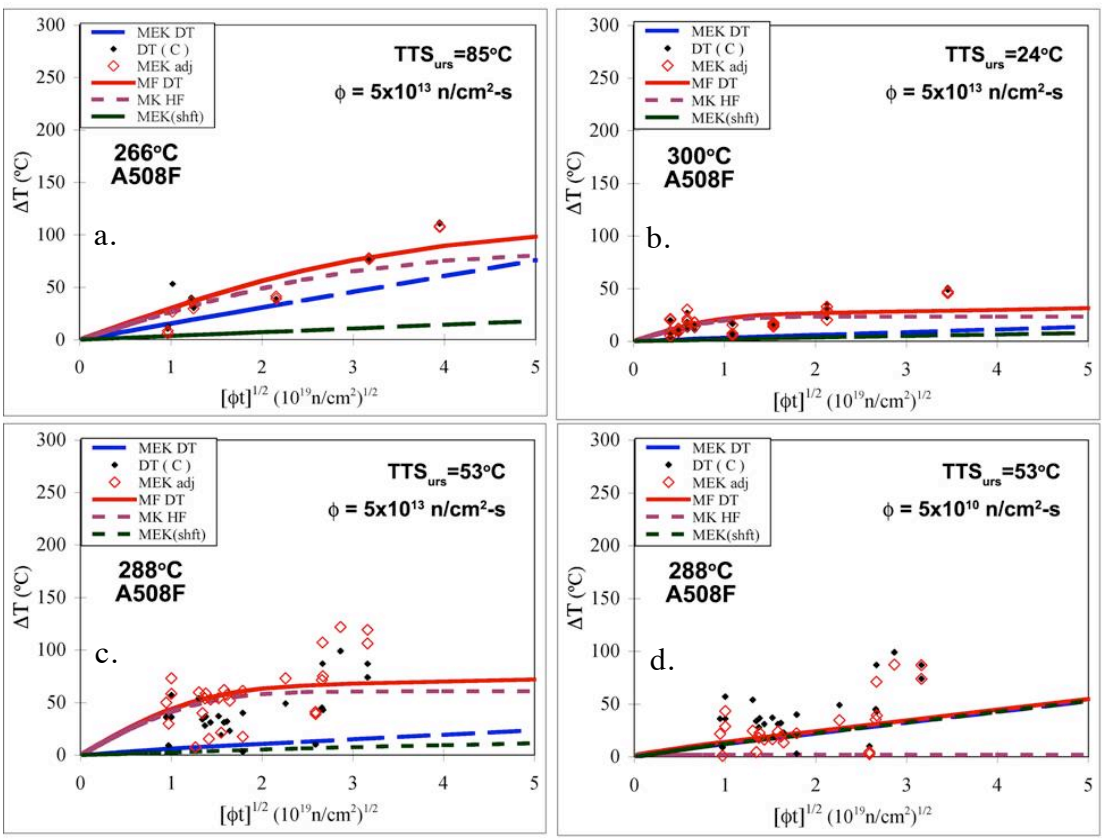

Figure 3.10 The 3FM predictions vs the sqrt fluence for a low-Cu (0.05 wt %) A508 forging at high flux (5×10^{13} n/cm^2/s) at nominal temperatures of 266, 288, and 300°C (511, 552, and 572°F). The predictions for low flux (5×10^{10} n/cm^2/s) at 288°C are also shown. The filled diamonds are RADAMO (high-flux) data. The open diamonds are the data adjusted to the reference conditions by the 3FM.

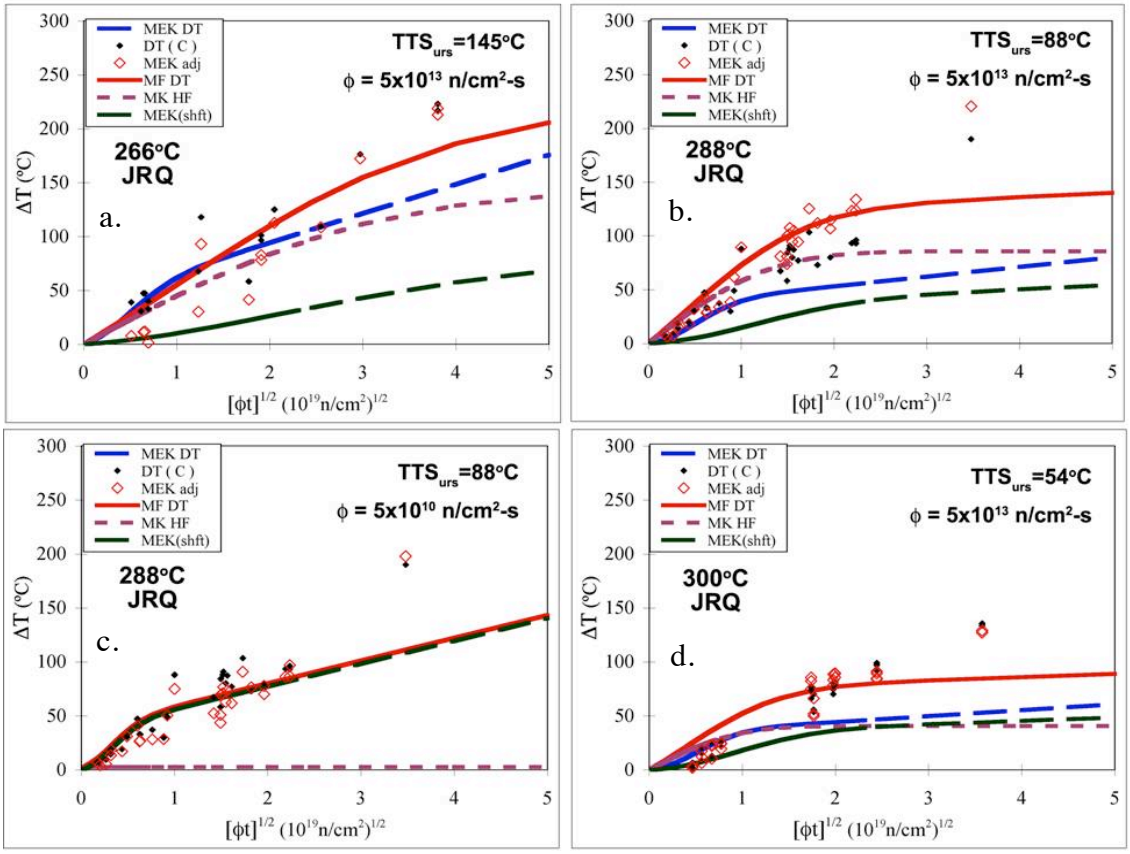

Fig. 3.11 The 3FTTS model predictions vs the sqrt fluence for the intermediate Cu (0.14 wt %) JRQ plate at high flux (5×10^{13} n/cm^2/s) at nominal temperatures of 266, 288, and 300°C (511, 554, and 572°F). The predictions for low flux (5×10^{10} n/cm^2/s) at 288°C are also shown. The filled diamonds are both IVAR (low-flux) and RADAMO (high-flux) data. The open diamonds are the data adjusted to the reference conditions by the 3FTTS model.

It is also important to note limitations of the 3FM in fitting some subsets of test reactor data. First, in most cases, the predicted minus measured TTS decreased relatively slowly, but systematically, with increasing measured TTS, yielding negative residuals at the highest TTS. The residual trends suggest that the simple 3FM model does not fully capture the shape of the TTS curve, especially at high fluence. Overpredictions are observed at low dose, especially for alloys with Cu contents above the threshold of ≈ 0.07 but below ≈ 0.2%Cu. The 3FM worked very well for the high-Cu welds in spite of the fact that the lowest irradiation temperature is outside the surveillance database limits. We believe that the differences at low fluence are primarily due to limitations in the base CRP + SMF model in these cases.

The results reported here were obtained prior to the current program but form th basis for improvements in the 3FM pursued in this work. This is sicussed in Section 5 below. Finally, Table 3.3 gives brief discriptions of the databases we use in the analyses.

Table 3.3 Brief summaries of databases used in the analyses

Database	Description	Ref.
IVAR	A comprehensive and systematic database developed by UCSB Irradiation Variables (IVAR) program, using a facility at University of Mishigan Ford Research Reactor for precisely controlled irradiations of large numbers of small specimens at different T_i (270, 290 and 310°C), ϕ ($\approx 8x10^{10}$, $3x10^{11}$ and ≈ 8 $x10^{11}$ n/cm^2-s) and overlapping ϕt ($\approx$ 0.006 to 3.6 x 10^{19} n/cm^2). The alloy matrix included 41 split melt model steels with systematic single and combined variations in the alloy Cu (0=0.8%), Mn (0-1.6%), Ni (0-1.6%), and P (0.005-0.040%) contents, 14 commercial/program steels (10 welds, 3 plates, and 1 forging) and 24 model alloys. The primary hardening database consists of $\approx$1900 $\Delta\sigma_y$ data points for different alloy-irradiation condition combinations.	DB1
RADAMO	A database developed by SCK•CEN in the RADAMO program to cover a large spectrum of irradiation conditions. Fourteen RPV materials (plates, forgings and welds) with various chemical compositions (Cu, Ni and P) were irradiated in the BR2 materials test reactor under well controlled conditions at two temperatures, 300 and 265°C in a large neutron fluence range from low (< 10^{19}) to high (>10^{20} n/cm², E > 1MeV) and various flux levels (0.2 to 8 x 10^{13} n/cm^{2}s, E > 1MeV).	DB2
PR-EDB	The Power Reactor Embrittlement Database (PR-EDB) is a comprehensive collection of data for U.S. designed commercial nuclear reactors. The current version of the PR-EDB lists the test results of 104 heat-affected-zone (HAZ) materials, 115 weld materials, and 141 base materials, including 103 plates, 35 forgings, and 3 correlation monitor materials that were irradiated in 321 capsules from 106 commercial power reactors.	DB3
Reve (UCSB BR2-A) DB	A database developed by UCSB within REVE program organzed by SCK•CEN for high flux high fluence conditions. 29 RPV materials (SMMS, Welds and model alloys) with systematic variation of chemical compositions (Cu, Ni, Mn and P) were irradiated in the BR2 materials test reactor at 300 °C to four neutron fluences ranging from 1.7 x 10^{19} to 1.3 x 10^{20} n/cm² (E > 1MeV) at a high flux of 10^{14} n/cm^{2}s as well as to a neutron fluence of 1.7 x 10^{19} n/cm² at a lower flux of 3 x 10^{12} n/cm^{2}s.	

[DB1] G. R. Odette, G. E. Lucas, D. Klingensmith, B. D. Wirth and D. Gragg, The Effects of Composition and Heat Treatment on Hardening and Embrittlment of Reactor Pressure Vessel Steels, NUREG/CR-6778 HT (2003)
[DB2] R. Chaouadi, "An Engineering Radiation Hardening Model for RPV Materials," SCK/CEN Report R-4235, September 2005.
[DB3] J-A. J. Wang and R. Subramani, "PR-EDB: Power Reactor Embrittlement Database Version 3," ORNL/TM-2006/605 (2008)

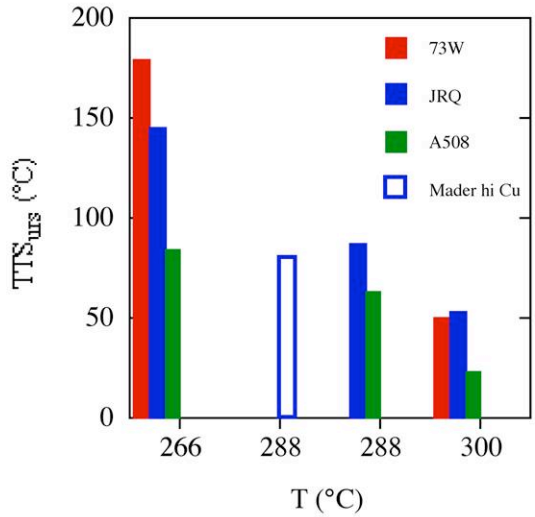

Fig. 3.12 The saturation TTS_{urs} for the A508 forging, JRQ plate, and HSSI Weld 73W showing the systematic effect of the (nominal) irradiation temperatures of 510, 550, and 570°F (266, 288, and 300°C) and alloy composition.

Section 4. Database Analyses

4.1 Formulating a Two-Feature Model (2FM) For the IVAR Database

We first analyzed updated database of all the low Cu alloys in the IVAR database in terms of an effective fluence ϕt_e fluence (10^{19} n/cm^2) referenced at a flux of $3x10^{11}$ /cm^2-s to fit SMF chemistry factors (CF_m) for individual alloys with a range of compositions in the form

$$\Delta\sigma_m = CF_m\sqrt{\phi t_e} \tag{4.1a}$$

The CF_m values for the various alloys were then fit to a simple linear equation with terms for both the compositions of individual, and products of, solutes that affect hardening. The best fit was found to be,

$$CF_m = 19.0Ni + 7.2Mn + 1246P + 245Cu - 46.1C + 18.3Si - 396.8NiP - 11.8 \tag{4.1b}$$

Figure 4.1 shows the resulting predicted versus measured comparison. The standard deviation in the CF_m ($\Delta\sigma_y$ at $\phi t_e = 10^{19}$ n/cm^2) is ≈ 3 MPa. Note Figure 4.1 also includes three alloys shown in open red cirucles that contain 0.1%Cu, slightly larget than ≈ 0.07%Cu minimum level generally observed to cause CRP hardening. While two 0.1% Cu alloys with low P are singifiantly underpredicted, the alloy with high 0.04%P is well

fit. This suggests there is an interaction between Cu and P that is consistent with previous observations that P that is contained in CRP is not available to form phosphide precipitates. The large negative Ni-P interaction is is not well understood.

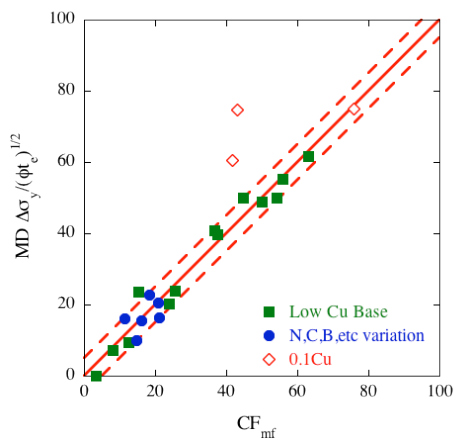

Figure 4.1 (a) Measured versus pedicted CF_{mf} for low Cu IVAR alloys.

Table 4.1 shows the parameters we obtained from fitting individual alloy $\Delta\sigma_y$ data sets IVAR database to our 2FM given in Section 3 as Eqs. 3.6c, 3.6f and 3.7a. We analyzed chemistry dependence of the three paramters, $\Delta\sigma_{pm}$, ϕt_{e80} and β, for CRP hardening term in various single variable data subsets. Figure 4.2 shows some single variable plots as a function of (a) Cu, (b) Ni or (c) Mn for corresponding subsets. For example, in Figure 4.2(a), blue show $\Delta\sigma_{pm}$ versus Cu for all the alloys with 0.8% Ni and 1.4%-1.6%Mn, while blue filled squares show the corresponding relation for 0.8% Ni and 1.6% Mn. The small differences in Mn does not seem to affect $\Delta\sigma_{pm}$ so that the two subsets were treated as one to give a curve that starts rising above a specified 0.072%Cu and saturates at around Cu ≈ 0.3%. The is well represented by

$$\Delta\sigma_{pm}(Cu) = C_{pm}[1 - \exp\{-k(Cu-Cu_{min})^m\}] \tag{4.2a}$$

Since the other alloys do not have enough data points to fit to their own curves, C_{pm} can be adjusted to account for different Ni and Mn contents as shown in Figure 5.2b and c. Including both Ni and Mn dependence in C_{pm} and rewriting the exponent part in more convenient way, we obtained a formula for $\Delta\sigma_{pm}$ as,

$$\Delta\sigma_{pm} = \left(k_{Ni}Ni + k_{Mn}Mn + k_o\right)\left[1 - \exp\left\{-\left(\frac{Cu - Cu_{min}}{Cu_0}\right)^m\right\}\right] \tag{4.2b}$$

The lines shown in Figure 4.2 are the model curves optimized for the parameter values from individual alloy fits. Here again the minimum Cu, Cu_{min}, is fixed to a well-

established value of 0.072%[7,8]. In summary, the $\Delta\sigma_{pm}$ analyses and the resulting formula indicated that $\Delta\sigma_{pm}$;

- Rises rapidly at Cu < 0.1% and saturate at Cu ≈ 0.3%
- Strongly depends on Ni at a rate of ≈ 100 and 120 MPa/Ni for Cu of 0.2 and 0.4, respectively
- Weakly depends on Mn at a rate of ≈ 30 MPa/Mn for 0.4% Cu

Figure 4.3 shows Cu, Ni and Mn dependence of ϕt_{e80}, that sets the hardening transition ϕt_e scale. As expected ϕt_{e80} decrease with incrasing Cu in a way that can be represented as a linear function of k/(Cu - Cu_{min}) (Figure 4.3a) times a coefficient and intercept that depends on Ni as seen in Figures 4.3b. Mn has little effect as shown in Figure 4c. One alloy with 0.1%Cu, 0.8%Ni and 1.4%Mn (LH) falls well above the other data trends. As will be shown later, because of the small CRP hardening for the alloy with relatively low Cu, this has little effect on the overall hardening prediction. The resulting fit function form is,

$$\phi t_{e80} = \frac{k_{a,Ni}Ni + k_{ao}}{Cu - Cu_{min}} + k_{b,Ni}Ni + k_{b,Mn}Mn + k_o \tag{4.3}$$

Again Cu_{min} = 0.072%.

Table 4.1 optimized parameters for CRP hardening formula in individual alloy fits

Alloy	Cu	Ni	Mn	P	$\Delta\sigma_{ypm}$	β	L	ϕt_{e80}
LA	0.4	0	1.37	0.005	77.75	0.958	33620595.94	0.0774
LB	0.4	0.18	1.35	0.005	84.66	4.041	44.83	0.0474
LC	0.41	0.86	1.44	0.005	163.85	1.170	122.90	0.1939
LD	0.38	1.25	1.38	0.005	213.33	1.110	594.77	0.3501
LH	0.11	0.74	1.39	0.005	59.12	0.955	37.38	1.1444
LI	0.2	0.74	1.37	0.005	116.06	1.117	448.29	0.3247
LJ	0.42	0.81	1.34	0.005	142.86	1.227	37.22	0.1698
LK	0.8	0.81	1.13	0.005	113.67	1.125	25.01	0.1599
LO	0.41	0.86	1.44	0.005	186.59	1.445	9.94	0.2456
CM11	0.34	0.85	1.64	0.006	157.14	1.332	340.00	0.1846
CM13	0.11	0.83	1.61	0.004	69.81	1.502	110.69	0.6909
CM15	0.22	0.02	1.59	0.002	43.72	4.000	109.53	0.0479
CM16	0.22	0.82	1.58	0.004	138.25	1.729	148.68	0.2898
CM17	0.22	1.59	1.54	0.004	242.62	1.574	172.10	0.4197
CM18	0.43	0.02	1.7	0.002	66.97	4.000	172.08	0.0435
CM19	0.42	0.85	1.63	0.005	162.02	1.208	217.38	0.1579
CM20	0.43	1.69	1.63	0.006	270.54	1.084	316.02	0.2770
CM21	0.42	0.84	0.01	0.002	107.35	1.087	26.57	0.1312
CM22	0.42	0.84	0.84	0.002	146.76	1.435	32.11	0.1722
JRQ	0.14	0.82	1.4	0.019	119.33	1.091	60.00	2.5087
A302	0.14	0.2	1.2	0.015	57.49	0.988	100000000.00	2.8607

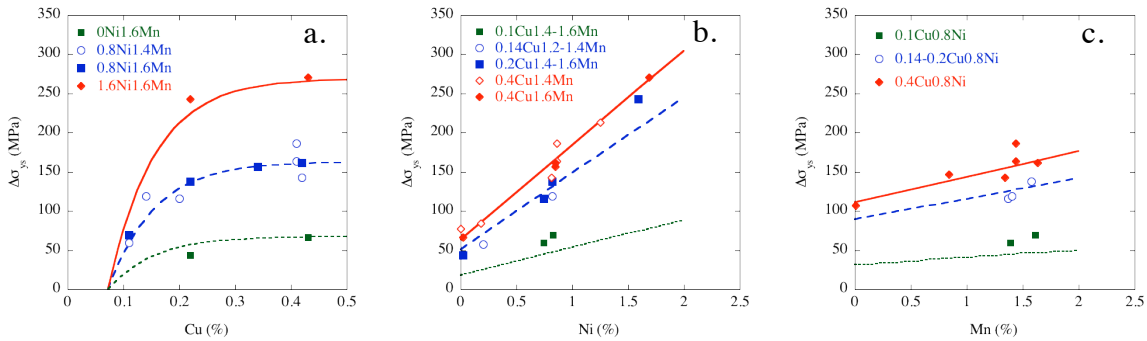

Figure 4.2 $\Delta\sigma_{pm}$ parameters best fitted to individual alloy sets as a function of (a) Cu, (b) Ni or (c) Mn for single variable subsets where only the focused element varies with other chemistry in common.

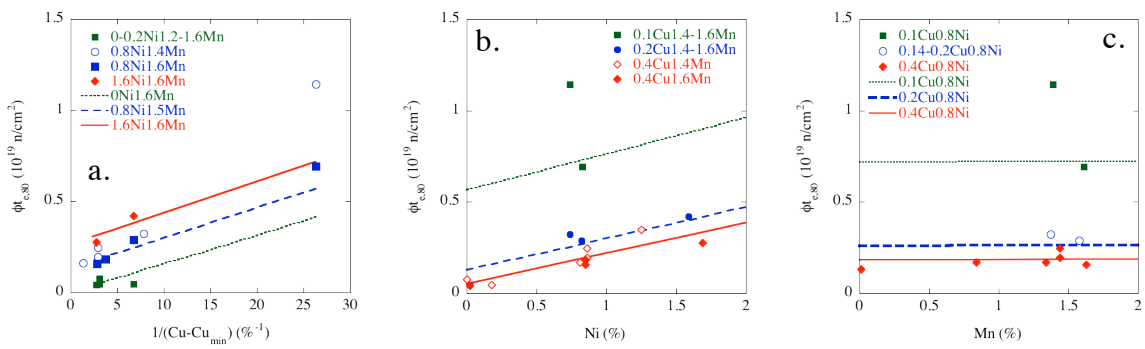

Figure 4.3 ϕt_{e80} parameters best fitted to individual alloy sets as a function of (a) Cu, (b) Ni or (c) Mn for single variable subsets where only the focused element varies with other chemistry in common.

Figure 4.4 shows the transition shape factor, β, as a function of Cu, Ni and Mn. There is no statistically significant effect of composition except for 3 out of the 5 low Ni (≤ 0.2%) alloys with a high β ≈ 4 versus an average of 1.xx for higher Ni alloys; two low Ni steel added Ni also has a low β ≈ 1. The average value is ≈ 2.8 in the low Ni case. The lines in Figure 5.4 are have slopes that result from fits to all the data and magnitudes for that slope fit to the data subset. Thus (need space after =)

$$\beta = k_{\beta,Cu}Cu + k_{\beta,Ni}Ni + k_{\beta,Mn}Mn + k_{\beta 0} \tag{4.4}$$

The implied dependence on is weak (Cu and Ni) or negligible (Mn) and and has little overall effect on the $\Delta\sigma_y(\phi t_e)$ models.

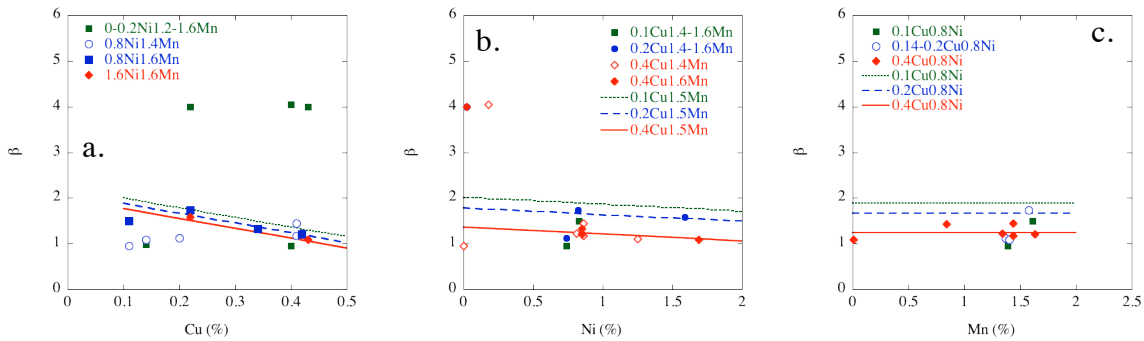

Figure 4.4 β parameters best fitted to individual alloy sets as a function of (a) Cu, (b) Ni or (c) Mn for single variable subsets where only the focused element varies with other chemistry in common.

The values of parameters were further refined by least square fitting all the $\Delta\sigma_p$ data simultaneously. During the overall fitting we identified some limitations of the models for a few alloys. One has an extremely high Cu content of 0.8% (LK), while the others have different production route or heat treatment conditions (JRQ and A302B). Those data have been excluded in the refinement. Table 4.2 summarizes the optimized values for the coefficients. Figure 4.5a shows the measured $\Delta\sigma_y$ versus predicted values for all the relevant alloys. The optimized model gives the predictions with standard error of ≈ 15 MPa for the whole dataset. Figures 4.5b, c and d show comparisons of indivually fitted $\Delta\sigma_{pm}$, ϕt_{e80}, and β, with those from the optimized chemistry formulas. The chemistry formulas predicted those experimental values with a standard error of 10.3 MPa, 0.15×10^{19} n/cm^2 and 1.1, respectively, for relevant alloys.

4.2 Predicted $\Delta\sigma_y(\phi t_e)$ Curves for the IVAR Database

Figure 4.6 shows the optimized 2FM model predictions (red solid lines) for 0.8%Ni, 1.4-1.6%Mn split melt IVAR alloys with various Cu contents, plotted along with experimental data and the curves fitted to the individual alloys (black dashed lines). Except some minor discrepancies in transition shapes, the 2FM predictions are consistent with experiment.

Figure 4.7 shows the corresponding comparisons for 0.2 (top) or 0.4% Cu (bottom) and 1.6%Mn split melt IVAR alloys with Ni varing from 0% on the left to 1.6% on the right. Figure 4.8 shows comparisons for 0.4% Cu and 1.4%Mn split melt IVAR alloys with Ni varying from 0.2% on the left to 1.3% on the right. Higher Ni significantly increase the saturation CRP hardening and also increases the slope at saturation due to higher SMF hardening with increasing Ni. Higher Cu for the alloys in the bottom figures shifts the CRP transition to a slightly lower fluence. The optimized prediction model is very consisyent with experiment with some exceptions in the transition shape (due to poor representation of β parameter in some low Ni alloys and slightly over estimate and underestimate of low Ni and high Ni alloys, repectively, for Cu = 0.2%, due to the $\Delta\sigma_{pm}$ function shape that was optimized for 0.8% Ni. Ni content seems to affect transition parameter, Cu_0, in Equation 4.2. The refinement of the coefficients should be performend in our future project for an expanded database with more alloys in the chemistry range.

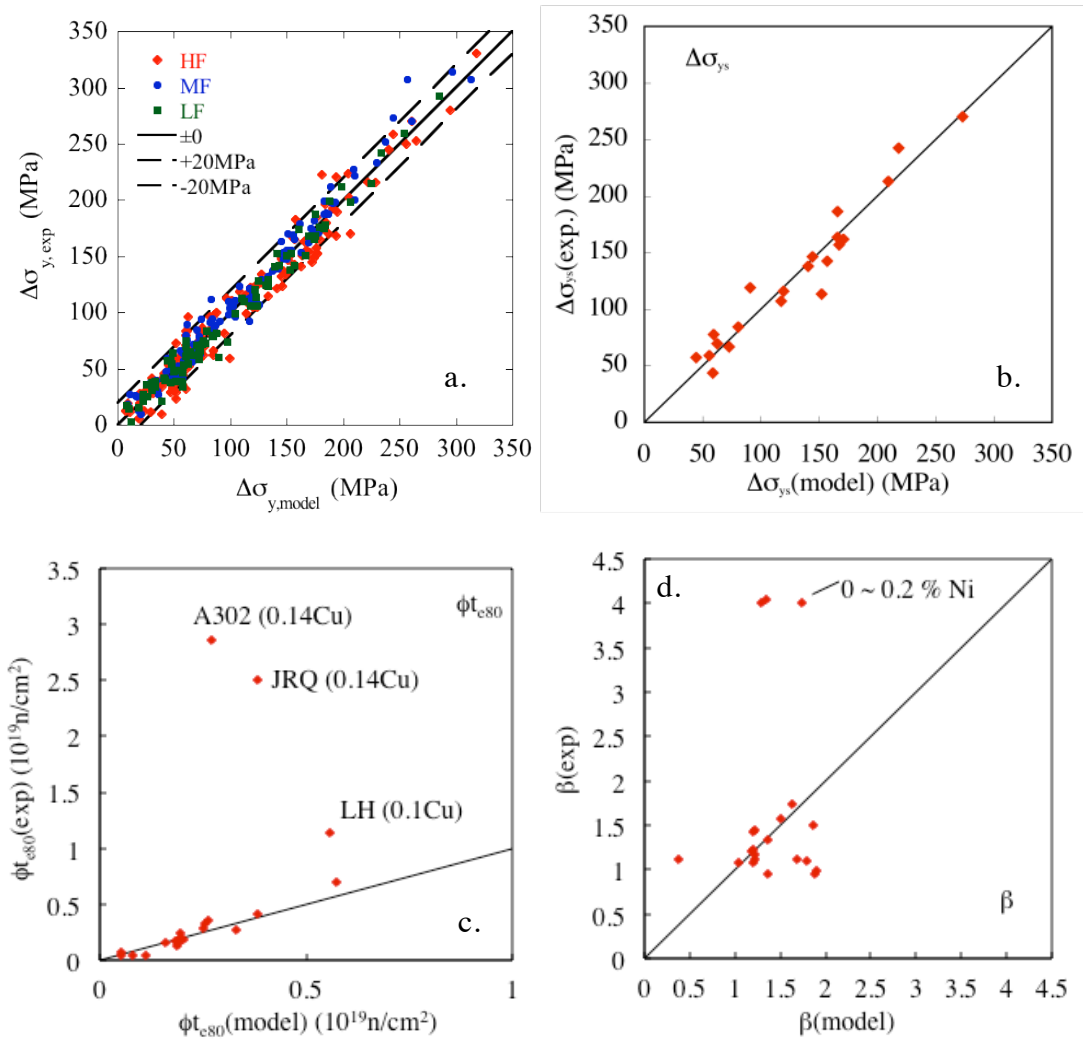

Figure 4.5 Measured (for the individual alloys fit) versus predicted (by Equations 3.8, 3.9, 4.2-4) $\Delta\sigma_y$ (a) and c CRP hardening term paramters $\Delta\sigma_{pm}$ (b), ϕt_{e80} (c) and β (d).

Figure 4.9 compares the 2FM prediction on split melt IVAR alloys with 0.4% Cu and 0.8% Ni for Mn variations from 0% on the left to 1.6 % on the right. As has been discussed earlier Mn has a weak effect on $\Delta\sigma_{pm}$. The agreement with the experimenta data is excellent in all of these cases.

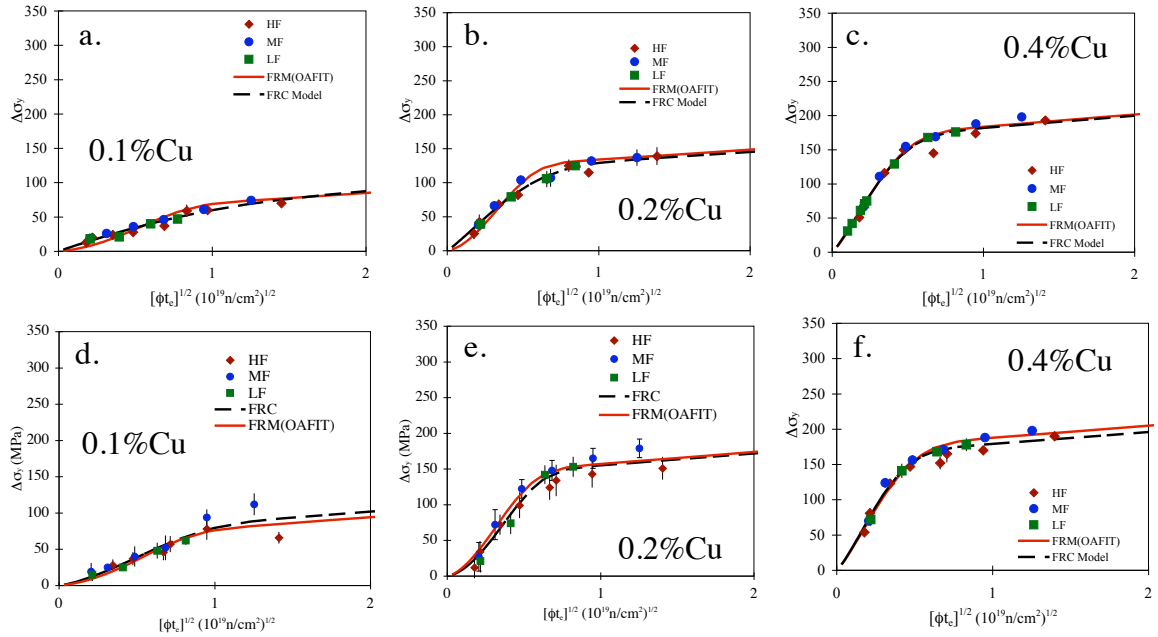

Figure 4.6 The 2FM prediction (red solid lines) compared to experimental data and fits to the individual alloys (black dashed lines) for 0.8%Ni, 1.4-1.6%Mn split melt IVAR alloys with a range of Cu contents.

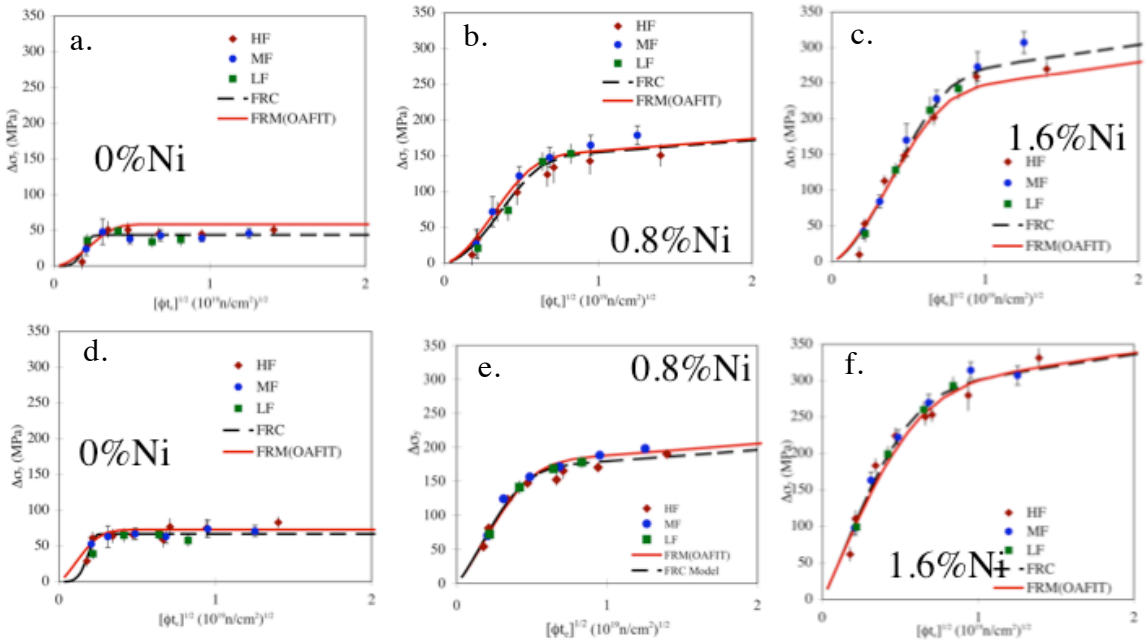

Figure 4.7 The 2FM prediction (red solid lines) compared to experimental data and fits to the individual alloys (black dashed lines) for 0.2 – 0.4% Cu, 1.6% Mn split melt IVAR alloys with a range of Ni contents.

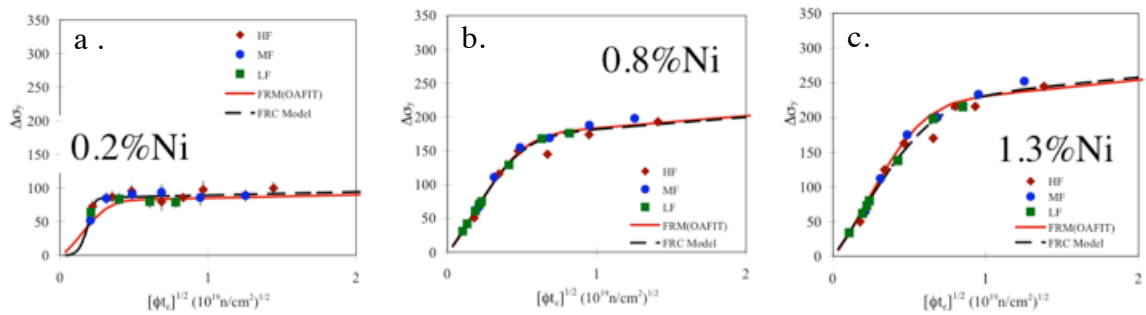

Figure 4.8 The 2FM prediction (red solid lines) compared to experimental data and fits to the individual alloys (black dashed lines) for 0.4% Cu, 1.4% Mn split melt IVAR alloys with a range of Ni contents.

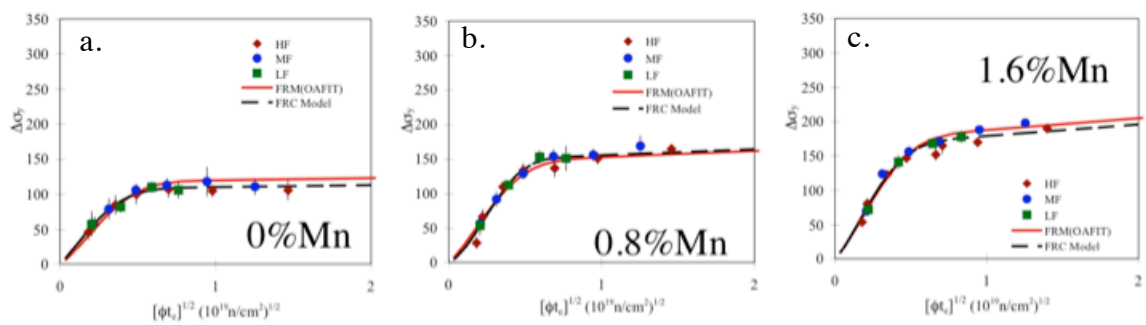

Figure 4.9 The 2FM prediction (red solid lines) compared to experimental data and fits to the individual alloys (black dashed lines) for 0.4% Cu, 0.8% Mn split melt IVAR alloys with a range of Mn contents

4.3 Updated 3FM

The basis for the 3FM was described in Section 3.3 Considerable effort has been put into refining the 3FM. We show only one example of various approaches including one based on an extensive analysis of a low Cu steel database another program. The examples we show are for the same three alloys described in Section 3 (73W, JRQ and A508).

The Mader-Odette model is used to calculate the UMD hardening and TTS, which is given by

$$\Delta\sigma_{UMD} = 3Gb\alpha_{UMD}[2r_{UMD}\phi\tau_{UMD}N_a\sigma_{vc}\{1 - \exp(-\phi t/\phi\tau_{UMD})\}]^{1/2} \quad (4.5)$$

The UMD parameters are listed in Table 4.3. Good fits were obtained with a nominal UMD strength parameter $\alpha_{umd} = 0.1$ except in the case of the low Cu A508 forging where $\alpha_{umd} = 0.067$ gave a good fit. The τ_{UMD} were based on the nominal value at 290°C and scaled to 266 and 300°C using the nominal activation energy of 1.92 eV.

The CRP and SMF contributions were taken for the EONY model using a effective fluence, ϕt_e, based on the caculated $g_s(\phi)/g_s(\phi_r)$ computed from the model described in Section 3.3 for $\phi_r = 4.4x10^{10}$ n/cm^2: $\phi t_e = \phi t_e[g_s(\phi)/g_s(\phi_r)]$. The EONY and ϕt_e parameters are also given in Refs. [7, 8]. The only modification was that the product form for plates was used for the forging with ≈ 1.4%Mn versus ≈ 0.8%Mn characteristic of that product from in the US database.

Table 4.2 optimzed values for 2FM CRP term coefficients

$\Delta\sigma_{pm}$ term		$\phi t_{e,80}$ term		β term	
k_{Ni}	122.9	$k_{a,Ni}$	0.0009490	$k_{b,Cu}$	-2.151
k_{Mn}	32.93	k_{ao}	0.01571	$k_{b,Ni}$	-0.1525
k_o	15.19	$k_{b,Ni}$	0.1645	$k_{b,Mn}$	0 (fixed)
Cu_{min}	0.072(fixed)	$k_{b,Mn}$	0.002263	k_{b0}	2.224
Cu_0	0.08270	k_o	0 (fixed)		
m	1.013				

Table 4.3 optimzed values for 3FM UMD hardening

Base Material Parameter		
Shear modulus (MPa)	G	8000
Burgers vector (nm)	b	0.248
Atom density (m^{-3})	N_a	8.55x10^{28}
Formation cross section (baan)	σ_{vc}	45
UMD obstacle strength	α_{UMD}	0.672
UMD radius (nm)	r_{UMD}	0.31
UMD annealing time constant (sec)	$\tau_{UMD,0}$	1.24x10^{11}
UMD annealing activation energy (eV)	E_{umd}	1.855

The results for this example are shown on Figure 4.10 to 4.12. In each case the sub-figure a shows the raw data, sub-figure b shows the high flux 290°C condition, sub-figure c shows the low flux 290°C condition and sub-figure d shows the 266°C high flux conditions, respectively. The filled symbols are the raw data and the open symbols are adjusted to the common irradiation temperature and flux indicated in the figure, as well as a Mn content of 1.4% for the IVAR A508 forging.

The agreement between the revised 3FM and the IVAR (blue circles) and Radamo (red triangles) data is reasonable to good in all cases. It is noted that other vatiants of the model, including the version described in Section 3.3 yielded similar fits.

However it must be emphasised that such agreement does not signal the model is correct. As is described in Section 6, post irradiation annealing at 350°C for 5 h has been

carried out to try to estiate the UMD hardening in high flux (10^{14} n/cm^2-s) irradiated alloys. Preliminary analysis of these results suggests that the 3FM presented here overestimates the UMD hardening underestimates τ_{UMD} by about a factor of 2, respectively. Further, that fact that no recover is observed in a high fluence irradiation at a slightly lower flux is even more incosistent with the 3FM hypothesis regarding UMD. These issues are being investigated in our current RPV NEUP program.

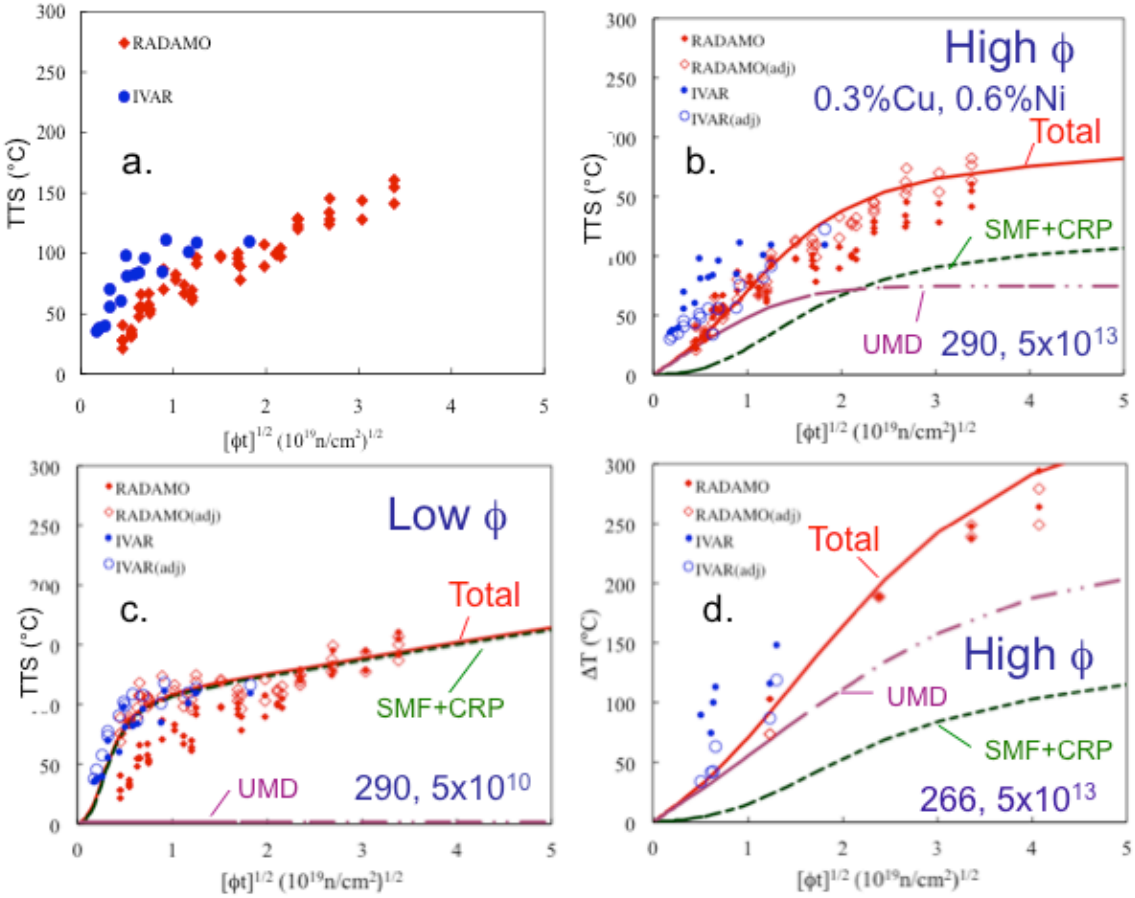

Figure 4.10 EONY- SMF/CRP + MO-UMD model predictions of TTS for 73W at 290 and 266 °C

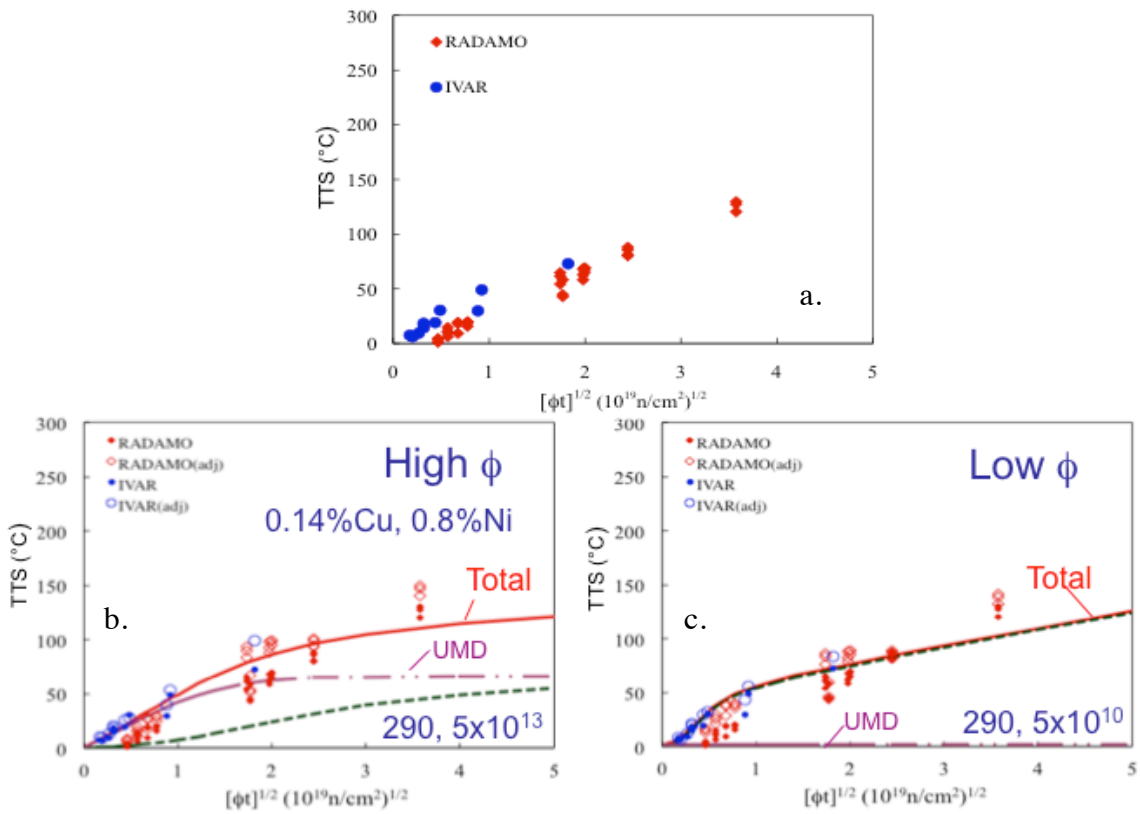

Figure 4.11 EONY- SMF/CRP + MO-UMD model TTS predictions for JRQ at 290 °C for two fluxes, 5 x 10^{10} and 5 x 10^{13} n/cm2s. Open symbols are adjusted for the model condition.

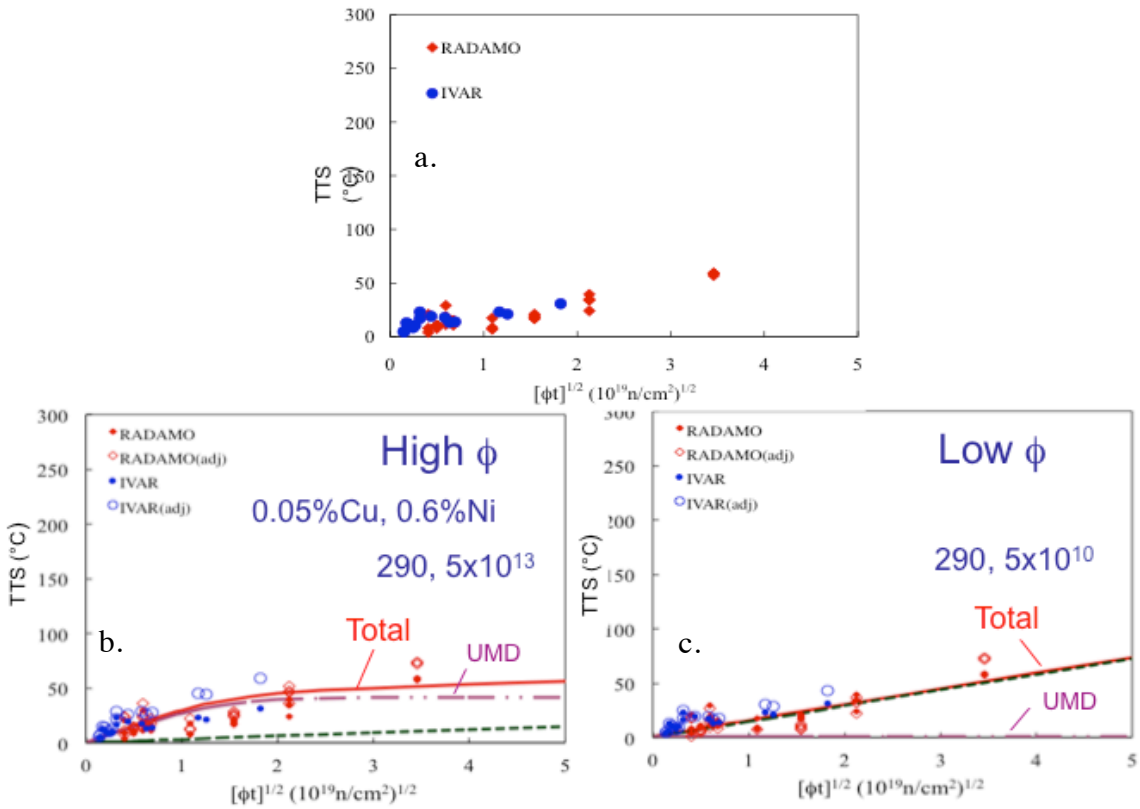

Figure 4.12 TTS predictions for A508 at 290 °C for two fluxes, 5 x 10^{10} and 5 x 10^{13} n/cm^{2}s. using EONY- SMF/CRP + MO-UMD model with α_{UMD} reduced by 1/3. Open symbols are adjusted for the model condition. Significantly over predict high flux data. (Similar to EONY-SMF/CRP + RR-UMD)

Section 5. The BR2 High Flux-High Fluence Irradiation Study

5.1 BR2 Experiments

While the previous results are very encouraging, there are only limited independent low ϕt data to support the 3FM. Thus, it is critical that the 3FM be refined and validated up to high ϕt. Fortunately, taking initial steps towards this objective is possible based on previous irradiations of a large number of IVAR alloy coupons in the BR2 reactor, which was an experiment designed to observe the effects of the irradiation variables at high flux ϕ and ϕt. There were five different irradiation conditions that included four at the same ϕ 10^{14} n/cm^2-s and a ϕt range from 1.7 to 12.7x10^{19} n/cm^2. The other condition was at a lower ϕ of 1.33x10^{12} n/cm^2-s to a ϕt of 2.1x10^{19}n/cm^2. This will be referred to as the BR2-A experiment. A second irradiation in BR2 was carried out at a lower flux of 2x10^{13} n/cm^2-s to 10^{20} n/cm^2. This so-called BR2-B study is ogoing and will only be briefly summarized in this report.

5.2 The BR2-A Irradiation

PIA experiments on the BR2-A and IVAR alloys were used to discriminate the flux-dependent UMD, SMF and CRP contributions from ≈ 6x10^{10} to 10^{14} n/cm^2-s. In

particular, lower temperature short time post irradiation annealing (PIA) at 350°C for 5 h was used to 'remove' the UMD, leaving the CRP and SMF hardening contributions largely unaffected. This allowed better quantification of the balance of UMD, SMF and CRP hardening contributions at high versus low ϕ for a wide range of alloys and compositions. The results can also quantify the UMD sink-induced delay in the SMF and CRP hardening contributions.

The irradiation conditions (G1-G5) in BR2-A are given in Table 5.1. A total of 29 different RPV alloys were included in the irradiation in the form of 0.5x2.9x25 mm coupons. Table 5.2 lists the 5 alloys that will be dicussed in this report. These alloys were all also included in IVAR, and 3 of the lower flux irradiation conditions from this latter experiment were studied here. Microhardness and SANS measurements were carried out on unirradiated, irradiated and PIA (350°C for 5 h to remove the UMD hardening contribution) conditions. The SANS measurements characterized the precipitate sizes, number densities and volume fractions.

5.3 PIA Results and Analysis

PIA studies at 350°C of the IVAR low ϕ and BR2 high flux data are shown in Figure 5.1 for 73W, LC and LG. Little recovery is seen in the low flux IVAR condition for annealing times of 5 and 10 h (top), while there is significant recovery in the high flux BR2 (bottom) that appears to level off at about 5 h. The recovery in BR2 generally increases with fluence, consistent with the increase in the population of UMD up to a steady state.

The hardness recovery after a 350°C, 5 h anneal for some IVAR and BR2 data is shown in Figure 5.2. There was a relatively large scatter in the recovery data, so the IVAR and BR2 data were averaged over several irradiation conditions at similar flux and fluence. The IVAR data was averaged over 3 conditions, T5, T6 and T16, which had average flux $\phi \approx 6\text{x}10^{11}$ n/cm^2-s and $\phi t \approx 2.1\text{x}10^{19}$ n/cm^2. The BR2 data was averaged over 2 conditions, G3 and G4, which had a flux $\phi \approx 1\text{x}10^{14}$ n/cm^2-s and an avergage $\phi t \approx 2.5\text{x}10^{19}$ n/cm^2. This data cleary shows that the UMD contribution to hardening is much more significant at high flux.

Table 5.1. The irradiation conditions in this study

Capsule	ϕ	ϕt
BR2 G1	1	12.7
BR2 G2	1	6.6
BR2 G3	1	1.7
BR2 G4	1	3.3
BR2 G5	0.0133	2.1
IV T5	0.008	1.4
IV T6	0.008	3.3
IV T16	0.003	1.6

*(10^{14} n/cm^2-s) **(10^{19} n/cm^2)

Table 5.2 The IVAR alloys in this study

Alloy	Cu (%)	Ni (%)
LG	0	0.8
LI	0.2	0.8
LC	0.4	0.8
LD	0.4	1.3
73W	0.3	0.6

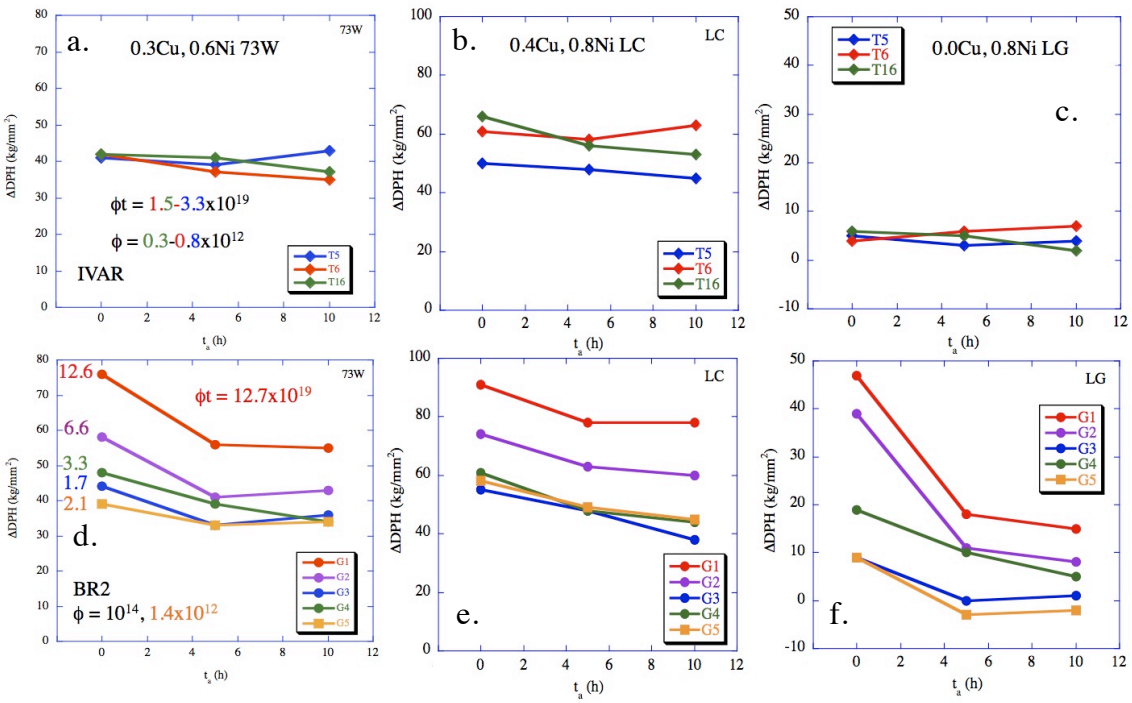

Figure 5.1 PIA hardness recovery in a copper free and high Cu split melt steel and a high Cu weld (73W) at 350°C for IVAR (top) and BR2-A (bottom) irradiations.

Figure 5.3 shows the yield stress increase as a function of square root of ϕt for a Cu-free steel (LG) with 0.8%Ni and 1.4%Mn. The hardening contributions are from SMF and UMD in Cu free steels, since no CRP are present. The filled symbols are the as-irradiated $\Delta\sigma_y$, while the open symbols are for the 350°C, 5 h annealed condition. The latter is assumed to be the hardening contributiondue to SMF because the UMD have been removed. The dotted blue line is the EONY $\Delta\sigma_y$ prediction for this steel while the red line is a fit to the low flux IVAR data. Both overpredict the estimated SMF hardening at high flux, consistent with the expected delay of SMF hardening to a higher fluence.

Increasing flux also delays CRP evolution to a higher fluence. Figure 5.4 plots SANS data for the precipitate sizes and volume fractions as a function of the square root of fluence for two high 0.4%Cu steels, LC (0.8%Ni) and LD (1.25%Ni). The very systematic effect of increased flux delaying precipitation is absolutely clear in this and for all other alloys (not shown) characterized in the BR2-A study.

Figure 5.5 plots $\Delta\sigma_y$ as a function of square root of ϕt for a 0.4%Cu, 0.8%Ni, 1.4%Mn steel (LC). The dotted blue line is the EONY prediction, while the red line is the fit of the IVAR data. While the highest fluence, high flux BR2 $\Delta\sigma_y$ is larger than the EONY prediction, after the UMD are removed with the 350°C, 5 h anneal, the CRP and SMF hardening are overpredicted at all but the highest fluence, which is consistent with the EONY prediction. This result is again further evidence that the CRP and SMF are delayed at higher flux.

The unfilled symbols in Figure 5.6 shows the CRP hardening ($\Delta\sigma_p$) predictions of for the LC alloy, based on the SANS data used input into Russell Brown hardening and obstacle superposition models described elsewhere [7,8]. The dashed blue and solid red lines are the EONY and IVAR fit predictions, repsectively. The delay in precipitate hardening with increasing flux is absolutely clear and far in excess of any uncertanties in the model based $\Delta\sigma_p$ predictions.

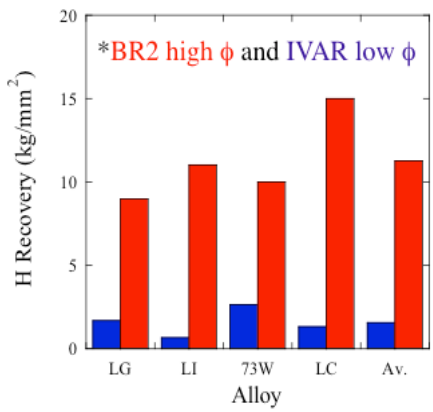

Figure 5.2 Comparison of the average hardness recovery for 350°C-5h anneals for irradiations in IVAR and BR2-A.

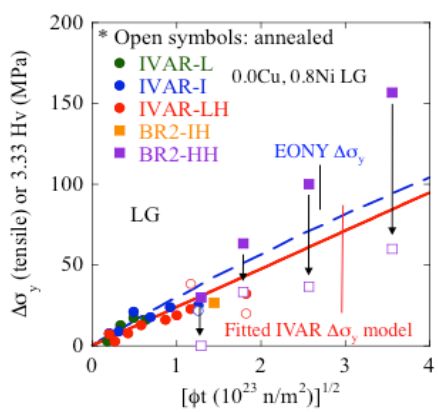

Figure 5.3 IVAR and BR2 hardening data in a Cu-free split melt steel (LG) in as-irradiated and PIA conditions along with EONY and IVAR fit model predictions.

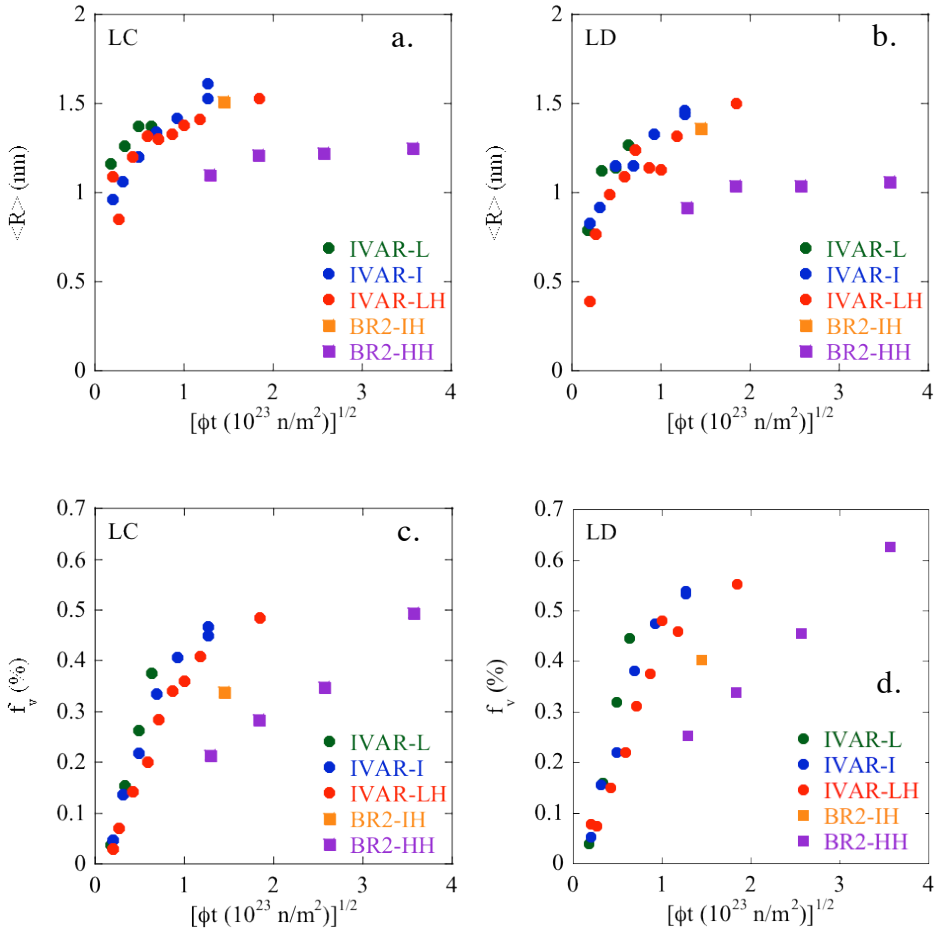

Figure 5.4 IVAR and BR2 SANS data for 0.4%Cu split melt steels with 0.8 (LC) and 1.3 (LD) %Ni.

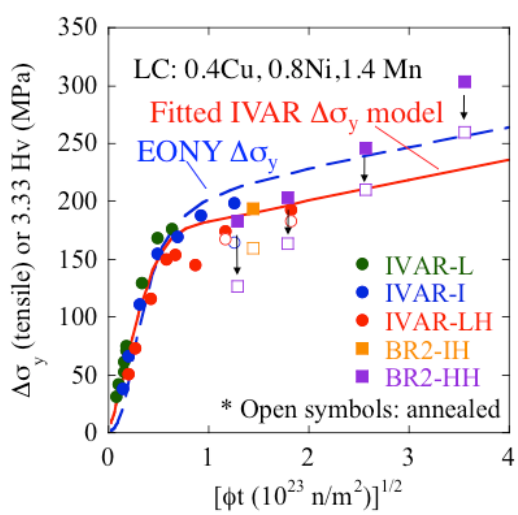

Figure 5.5 IVAR and BR2 hardening data for a 0.4%Cu, 0.8%Ni split melt steel in as-irradiated and PIA conditions along with EONY and IVAR fit model predictions.

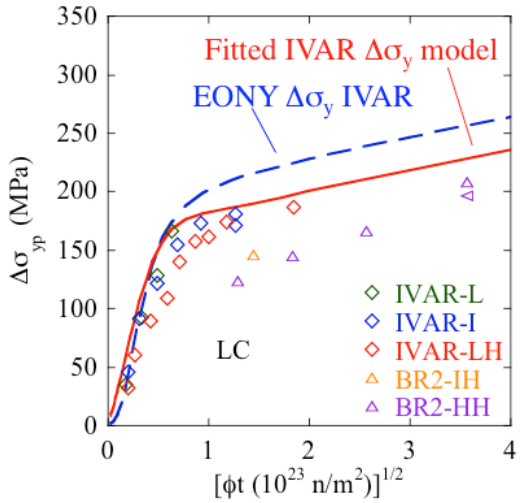

Figure 5.6 Predicted IVAR and BR2 CRP hardening (triangles) in LC based on the SANS data in Figure 5.4 along with EONY and IVAR fit model predictions.

Figure 5.7 Shows estimated SMF hardening for high flux BR2 irradiations based on subtracting the SANS based estimates of precipitate hardening (unfilled triangles) from BR2 350°C-5h PIA without UMD (unfilled squares). The results shown as half filled square symbols are remarkably consistent with the estimate of SMF hardening based on the annealed Cu free LG alloy in Figure 5.3, shown as the least square fitted solid line. Again the delay in the SMF hardening at high flux is perfectly clear.

Figure 5.8 shows that similar delays in high flux BR2 CRP and SMF hardening in the other alloys 73W, LI and LD shown in Table 5.2.

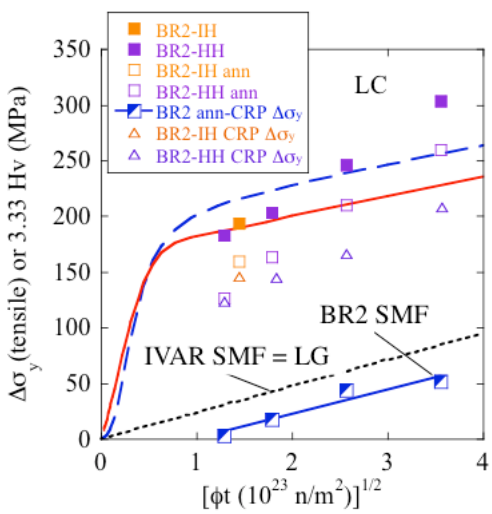

Figure 5.7 Predicted IVAR and BR2 SMF hardening (half filled squares) in LC based on subtracting the SANS based CRP hardening in Figure 5.6 along with the BR2 line for LG in Figure 5.3 (blue solid line) and the IVAR fit (dashed line).

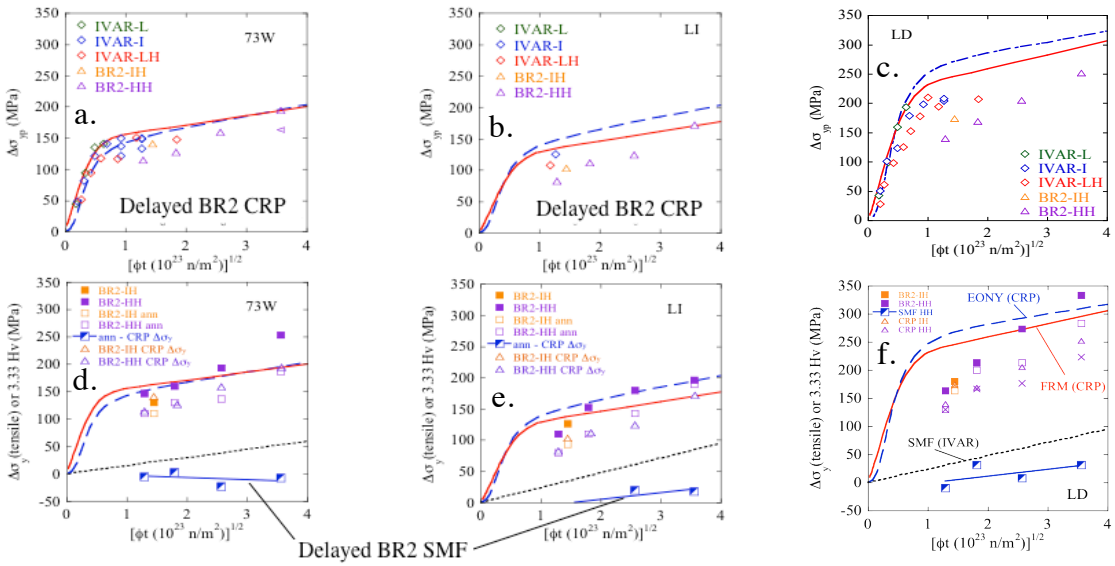

Figure 5.8 Corresponding SANS based CRP hardening (top) and predicted IVAR and BR2 SMF hardening (half filled squares with blue solid line in bottom figures) and the IVAR fit (dashed line) in 73W, LI and LD alloys.

5.4 Summary of BR2-A Results

The general trends in the IVAR-BR2 data are generally highly consistent with the 3FM with a few exceptions and differences. The most important observations are that:

- The 350°C-5h PIA produces significant recovery of UMD hardening.
- The high BR2 flux delay CRP and SMF hardening.
- The delays are observed in both mechanical properties and CRP nanostructures.
- The recovery observed in BR2-A is less than estimates in the previous 3FM
- The corresponding recovery times are similar to, or up to 2x larger, than estimates in the previous 3FM
- There is evidence of delayed emergence of late blooming phases in both Cu free and high Cu alloys with 0.8, 1.25 and 1.6%Ni in the high flux and fluence BR2-A irradiations (ongoing work not discussed here).
- The generally significant PIA recovery of hardeness in the interediate flux BR2-A irradiation (G5) is larger than expected and not well understood.
- There is significant scatter in the hardness data that may affect some data comparisons.

5.5 The BR2-B irradiation

A matrix of IVAR split melt IVAR model steels 0-0.4&Cu, 0-1.6%Ni, 1.4-1.6%Mn was irradiated at 290°C in BR2-B at a flux of $2x10^{13}$ n/cm^2-s to a fluence of 1 x 10^{20}. Since

there is only one fluence BR2-B results can be compared to the high fleuence BR2-A condition (G1). The PIE included hardeness change and positron annihlation spectroscopy (PAS) measurements of both the orbital electron momentum (OEM) spectra and positron lifetime of various alloys with systematic Cu and Ni variations. The irradiation was carried out in BR2 reactor at SCK-CEN, Belgium, using a Calisto capsule. The PIE was carried out the Oarai International Research Center for Nuclear Materials Science of Tohoku University. Measurements were made in the as-irradiated condition and flowing PIA at 350°C for 5 h. Since this is ongoing research we will only summarize the results obtained to date.

- Significantly lower hardening for the as-irradiated BR2-B condition than at a slightly higher fluence for BR2-A at a 5x higher flux of 10^{14}
- There is almost no PIA DH recovery for BR2-B $2x10^{13}$ vs large recovery for BR2-A at a higher flux of 10^{14}
- Hardening is similar for the as-irradiated and PIA BR2-B condition and the PIA condition for BR2-A
- There is good agreement in the DH and extrapolations of fitted IVAR curves for 0.0-0.4%Cu alloys with ≥ 0.8%Ni; but DH is higher than the predictions for low Ni steels
- PAS shows the BR2-B irradiation suppresses the high momemtum Cu and Ni like component and enhances low momentul component, associated with Mn and especially vacancies, in the OEM specra.
- PIA recovers the high Cu and Ni like momentum component, and reduces the low momentum component of the OEM spectra
- The low momentum component increases with Cu, especially after PIA.
- The average positron lifetime (τ_{av}) increases with Cu in the as irradiated but not in the PIA condition.
- The low versus high momentum and components are similar for Ni variations at ≤ 0.8% but the low momentum component decreases significantly in the 1.3%Ni alloy along with τ_{av}. In the latter case, the as irradiated and PIA low and high momentum components are similar.
- The higher flux BR2-A irradiation produces a larger low momentul component of the OEM spectra, a longer τ_{av} and a much larger fraction of the longer ($\tau_2 \approx 180$ ps) lifetime ($I_2 \approx 80\%$) compared to the lower flux BR2-B condition.

The most important overall conclusions derived from the BR2-B study, is that the while hardness generally follows compositional trends onserved at lower flux, and is insentive to PIA, significant changes in the PAS OEM and lifetimes occur during annealing. The low momentum component of OEM and lifetime is larger in the as-irradiated condition and increases with flux and Cu content. The large lifetime component is ≈ 180 ps. PIA reduces or eliminates the flux and Cu sensitivity. These results suggest that UMD are associated with a mono-vacancy. However the effect of vacancies associated with solute clusters is

not known. Thus there is a need to model the PAS data to obtain a more quantitative interpretation of the results.

Section 6. Design and Preparation for UCSB ATR-2 Irradiation Experiment to Develop a High Fluence Embrittlement Database

6.1 Background

The BR2-A and B experiments have been very useful in gaining insight on the effects of high flux and fluence on irradiation embrittlement. However, the flux levels in these irradiations were 400 to 2000 times higher than for typical RPV surveillance conditions. Further both the amount of material and specimen form (small coupons) in BR2-A and B were very limited. Thus the National Scientific Users Facility (NSUF) ATR UCSB-2 RPV Steel Irradiation Experiment (UCSB ATR-2) was proposed to fill the gap in embrittlement data. The irradiation itself was the result of a successful peer reviewed NSUF proposal awarded in 2009. The irradiation began in the summer of 2011. The preceeding two years involved a very major and intense effort to design, construct, fabricate, assemble and insert a large number (>1600) of specimens into the test train and the test train into the ATR. The engineering design of ATR-2 test train was led by INL staff in close cooperation with UCSB, especially in developing key conceptual features of the irradiation vehicle. The detailed engineering design, including extensive thermal and neutronic calculations, as well as a rigorous safety analysis, were carried out by INL staff. Steps involved in the scientific and technical design of the experiment, alloy acquisition and qualification, specimen fabriction, and loading into thin-walled subcapsule packets for insertion into the test train were carried out by UCSB with the assistance of a number of collaboraotrs. The collaborating instiutions included Oak Ridge National Laboratory, Rolls Royce Marine Power, in England, Bettis Laboratory, and the Central Research Institue of Electric Power Industry, in Japan.

The UCSB ATR-2 irradiation includes a large number (≈180) of RPV steels that fall into two broad categories: a) those which have been irradiated in a number of other programs over a wide range of flux; and, b) a new set of alloys that will fill in major gaps in the effects of composition on embrittlement. Irradiations are being carried out at nominal temperatures of 250, 270, 290 and 310 °C. Peak flux levels of ≈ 3.8×10^{12} n/cm^2-s will produce a maximum fluence of ≈ 10^{20} n/cm^2. All of the alloys are included in the form of multipurpose disc coupons. The specimens will be used for hardeness and shear punch tests and for making a wide variety of micorstructural samples for techniques that include transmission electron microscopy (TEM), small angle neutron scattering (SANS), atom probe tomography (ATP), resistivity-Seebeck coefficient measurements (RSC) and x-ray diffraction (XRD). A subset of 55 alloys is included as tensile specimens and 3 alloys as disc compact tensions specimens.

The most notable feature of the experiment is that it will provide high fleunce data at an intermediate flux that can be linked with other test reactor and surveillance data over a much wider range of flux. The experiment includes 9 steels that are included in rector surveillance programs. Thus the new ATR-2 and a number of other databases will be combined to refine and validate predictive physically based TTS models. A flux-fleunce map of some of these databases is shown in Figure 6.1.

Special emphasis will be on: a) assessing the effects of flux including use of post irradiation annealing (PIA) to evaluate the contributions of various hardening irradiation features as a function of flux, fluence and other embrittlement variables; b) identifying alloy-irradiation conditions leading to the formation of so-called late blooming phases that could lead to severe, and currently untreated, embrittlement; c) extensive microstructural characterization and mechanism studies; d) PIA recovery experiments as a potential embrittlement mitigation strategy; e) irradiation of new RPV alloys, including candidates for use in advanced reactors; f) evaluating the master curve method for measuring fracture toughness at high fluence in sensitive alloys; and g) addressing the surrogacy issue associated with alloy conditions in the actual vessel that typically differ from the nominally limiting steels for a particular reactor vessel.

6.2 Target Irradiation Conditions

The ATR-2 project is being irradiated in the I-22 position (southeast small I position) in the ATR, which has a peak fast flux of about 3.3×10^{12} n/cm^2-s. Insertion of irradiation test train was carried out in June of 2011. The initial plan was to withdraw the experiment from the reactor approximately one year after insertion upon achieving a peak fluence of approximately 1.3×10^{20} n/cm^2. However, unplanned outages have resulted in lower fluence at end of the planned final cycle of $\approx 0.88 \times 10^{20}$ n/cm^2, which occured early in 2013. The experiment had to be removed at that point since it was followed by a so-called PALM cycle that would result in overheating of the specimens. However, it was possible to re-insert the test train after the PALM cycle to achieve the peak and average fluence targets. .

The flux (and fluence) varies by about a factor of 3 along the test train. The nominal target temperatures and fluence for 13 subcapsules are shown in Table 6.1, along with the types of specimens. Multiple reaction dosimitry foil packets are also included in the test train.

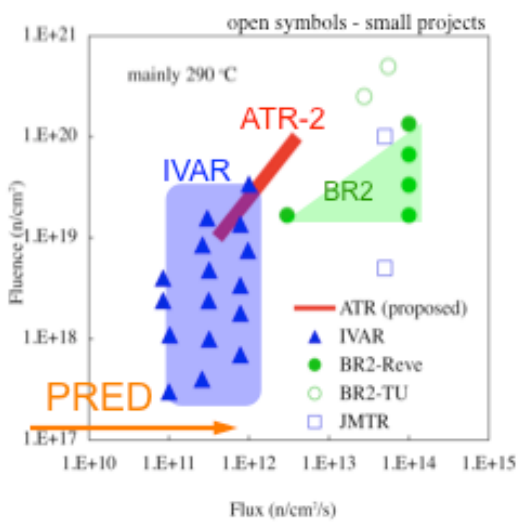

Figure 6.1. Flux-fluence map for RPV steel irradiations.

After the irradiation is completed the test train will be removed from ATR during a scheduled outage and stored in the canal for a cool down period of typically several months. After the initial cooling, the test train will be sized (cropped) for shipping to ORNL for disassembly and PIE. The mechanical testing PIE will primarily be carried out at ORNL but small microstuctural specimens will be shipped to UCSB and other laboratories, like the Idaho Center for Advanced Energy Studies (CAES), for detailed characterization by TEM, APT, SANS and so on.

*6.3 Test Train Design**

The test train provides a means to monitor and control experiment temperature and a barrier between the experiment samples and the reactor coolant. Figure 6.2 shows a cross section of the test train assembly, including the shroud basket. The test train pressure tube is designed to meet the intent of the American Society of Mechanical Engineers (ASME), Section III, Class 1 pressure vessel code requirements.

The interior of the test train contains specimen packets with a variety of specimen types as is described in later sections. The specimen packets are stacked vertically within the test train. The aggregate density of the specimens and sample holder is 95 - 97% of the density of steel (7.4 – 7.6 g/cm^3). A thermal neutron shield incorporated in the experiment basket is used to prevent excessive activation of the specimens. The thermal neutron shield must be effective for the lifetime of the experiment, up to a peak fast fluence of at least more than 10^{20} n/cm^2.

Vertical stacks of specimen packets in the test are separated by thermal insulating spacers. Insulator disks are be used at the top and bottom of the packets and are made of a low thermal conductivity stainless steel.

Table 6.1 UCSB-2 Subcapsule Target Irradiation Conditions Summary.

Capsule ID	Materials	Target Temp.	Nominal Target ϕt (x10^{19}n/cm^2)
UCSB-1	coupon/tensile	290 ºC	low 4.2
UCSB-2	coupon/tensile	290 ºC	low 6.2
UCSB-3	coupon/tensile	290 ºC	med 8.8
UCSB-4	coupon/tensile	270 ºC	med 10.3
UCSB-5	coupon/tensile	250 ºC	med/hi 10.9
UCSB-6	DCT	290 ºC	hi 11.7
UCSB-7	coupon/tensile	290 ºC	hi 12.2
UCSB-8	coupon/tensile	290 ºC	hi 12.3
UCSB-9	DCT	290 ºC	hi 11.7
UCSB-10	coupon/tensile	310 ºC	med/hi 11.0
UCSB-11	coupon/tensile	290 ºC	med 9.8
UCSB-12	DCT	290 ºC	low 7.6
UCSB-13	coupon/tensile	290 ºC	low 5.5

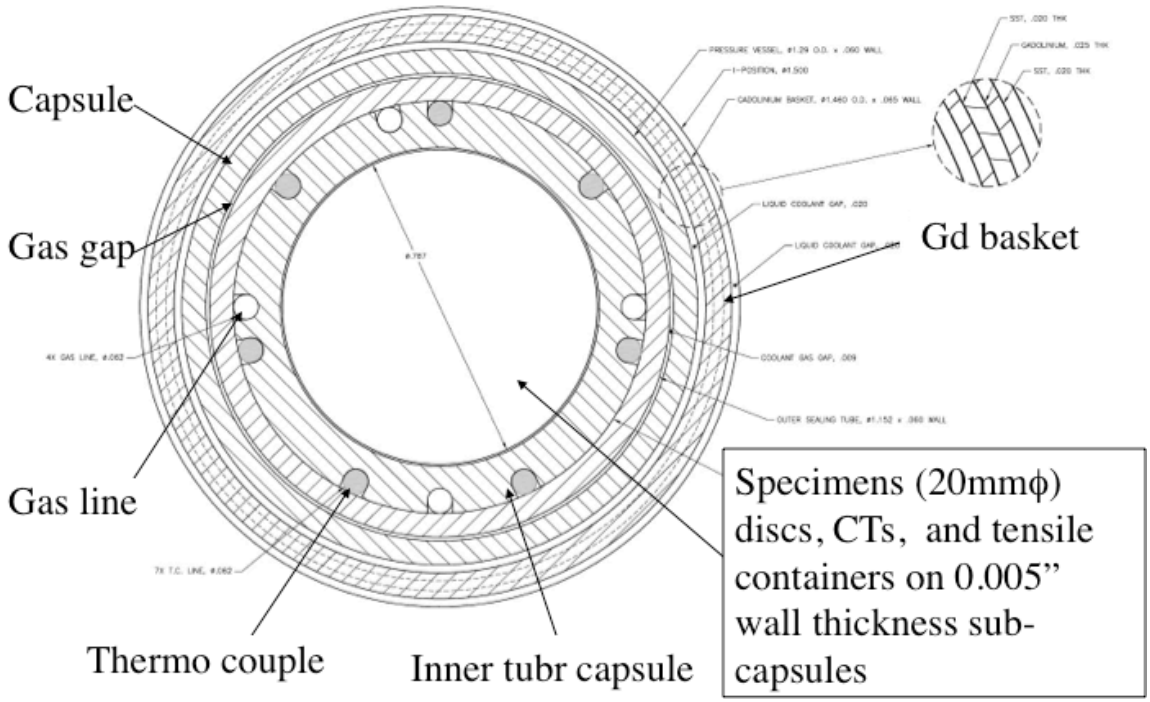

Figure 6.2. UCSB ATR-2 experiment test train cross section. Dimensions listed in inches.

The radial gap between the sample holders and test train inner diameter is filled by a gas mixture of helium and argon. The gas gap width is designed to allow temperature control over the lifetime of the experiment, within the range of the He/Ar gas composition. The irradiation temperature is monitored by thermocouples located in close proximity to the specimen packets. If the specimen packet temperature varies from the target temperature, the composition of the gas mixture is automatically adjusted by a gas control system to provide the thermal resistance in the gas gap necessary to achieve the design irradiation temperature. The test train included three individual gas control segments. The gas gaps within each segment were vatied to provide different temperature zones, with approximately uniform temperature within each zone.

The specimen subcapsule packets were fabricated and assembled at UCSB. Final assembly of the test train was performed at INL. Figure 6.3 shows the location of the different packets and their nominal target temperatures.

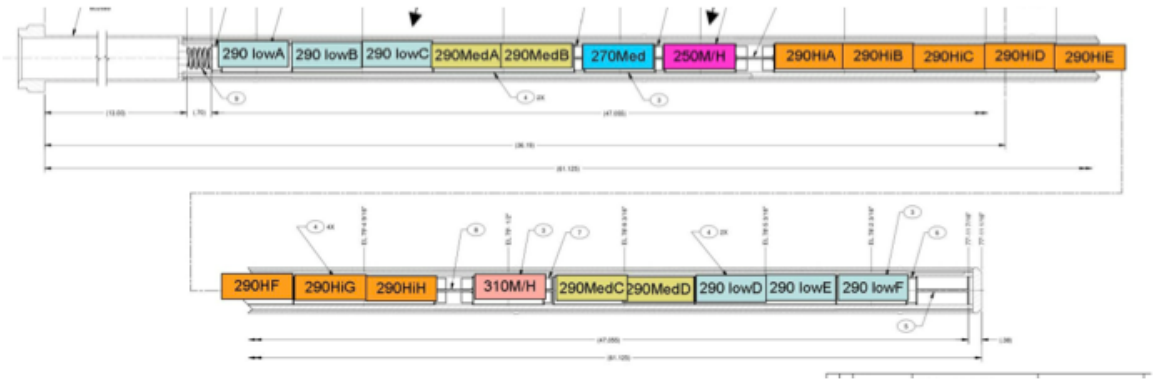

Figure 6.3. Packet locations and target temperatures

The internal gamma and neutron heating for each component of the test train was calculated using MCNP (Monte Carlo N-Particle) code. The nominal peak target specimen dose is also listed in Table 6.1. The test discharge date will be based on actual ATR operations and discussions between INL and UCSB and the test will be discharged from the reactor during a scheduled ATR outage.

The expected peak thermal conditions during irradiation for this experiment were estimated based on thermal analysis using sample heating rates calculated by MCNP. Complete finite element thermal analysis was performed at the INL to identify the design parameters and gas mixtures needed to reach the target temperatrures. Mock-up tests with simulated gamma heating and gas mixtures were performed at the INL to verify the target temperatures will be met. Figure 6.4 shows the excellent agreement between the calculated and actual temperatures in the capsules.

6.4 Materials and Specimens

ATR-2 includes a test matrix of ≈ 180 RPV steels and model alloys with carefully controlled compositions and commercial alloys. This includes materials from the IVAR program (CM, L-series) and commercial and program welds, plates and new split melt alloys. These alloys have iron (Fe) as the major constituent, making up ≥ 90 wt.% of the alloy mass. A few alloys with 8-14% Cr, 3% W, 1.5% Mo and < 0.5 %V, Si, Ti, Ta, Y and bal Fe > 0.8 are also included, as well as small quantities of elemental Cu, Fe, Ni, Mn incorporated into diffusion couples. The composition of alloying additions or impurities such as copper (Cu), nickel (Ni), manganese (Mn), chromium (Cr), molybdenum (Mo), phosphorous (P), carbon (C), silicon (Si) and carbon (C) are varied to determine the effect on alloy irradiation behavior. In addition, trace impurities that result from the fabrication process may be present.

Several different specimen geometries were included in the experiment. All specimens were placed inside packets. Packets of irradiation specimens were assembled that represent a common sample geometry and irradiation temperature. Spaces between specimens in the packets were be filled with steel. The sample types are described below and the number of specimens and alloys of each type are summarized by alloy (or project) group in Table 6.2.

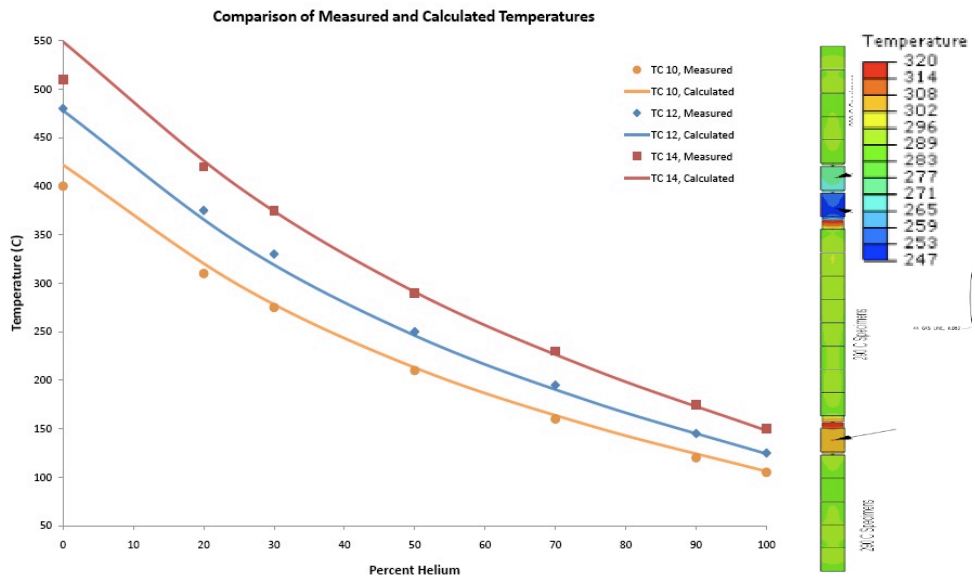

Figure 6.4. Comparison of measured and calculated temperatures in the mock up test.

Disc multi-purpose coupons (DMC), shown in Figure 6.5 or embedded discs make up the majority of the samples. They will be ≈ 20.0 mm (.79 in.) in diameter and from 0.25 to 1.0 mm (.010 to .039 in.) thick. The majority of coupon specimens are in 2 cm diameter disc form; precision punched, ground and polished on both faces and laser engraved with alloy code and serial number. Other coupon specimens will have square, circular or tensile specimen inserts. These specimens will be used for microstructural studies, hardness and shear punch tests, atom probe tomography, neutron and X-ray scattering spectroscopy, and TEM.

Disc compact tension (DCT) specimens, shown in Figure 6.6a, that are ≈ 20.0 mm (.79 in.) in diameter with fatigue pre-cracks will be used for fracture toughness tests. Steel inserts will be placed in the holes in the DCT specimens to reduce temperature gradients. Subsize tensile specimens (SS-J2), shown in Figure 6.6b, are 4.0 mm (0.16 in.) wide x 16.0 mm (0.63 in.) long and 0.5 mm (0.02 in.) thick. Over 350 specimens were included. The gauge (testing part) length is 5.0 mm (0.2 in). A stack of the specimens is contained in a holder with the dimensions of ≈ 20.0 mm in diameter and ≈ 6 mm tall, that is designed to minimize temperature gradient across the specimen stack.

Diffusion multiples were included to study the different diffusion behaviors of Fe-Cu-Ni-Mn. It contains an outer ring of OV1, which is an Fe model alloy containing 1.6 wt% Mn. A disc was inserted into this ring that is composed of one half of high purity Cu and one half of high purity Ni. Different intersections of materials can be used to evaluate diffusion of each of the individual elements in the others.

6.5 Status and Schedules

UCSB ATR-2 experiments started irradiation on 6/7/2011. Figure 6.7 summarizes the differences of actual temperatures recorded during irradiation from their target value. Except the low-mid flux range at the bottom being slightly affected by adjacent high temperature zone, all the subcapsules are maintained within ≈ 15 °C from the target. The capsule was removed from

the position during the “palm” cycle, the reactor being operated at higher nominal power, to avoid higher neutron flux and temperature. Currently the capsule waits for re-insertion to receive three more cycles of irradiation to achieve target neutron fluences. Post-irradiation examination is expected to begine in early 2014.

Table 6.2 Type and number of specimens included for alloy group.

	Lg Disc		Sm Disc		Tens		DCT		Any Type	
Total # alloy/irrad cond	Alloy	Spc.	Alloy	Spc.	Alloy	Spc.	Alloy	Spc.	Alloy	Spc.
Total # spc	144	1028	40	224	55	367	3	45	173	1664
DCT matrix	3	14			3	54	3	45	3	113
CM alloys	21	231			13	92			21	323
Laval alloys	10	72			8	48			10	120
UCSB Commercial alloys	13	107	1	4	9	53			13	164
EPRI alloys	20	141			6	21			20	162
ORNL alloys	5	64	5	41	8	51			9	156
RR alloys	57	356	11	80	8	48			68	484
Bettis alloys	5	25							5	25
CRIEPI alloys			13	65					13	65
OV model alloys	9	15	10	34					10	49
Diffusion Multiples	1	3							1	3

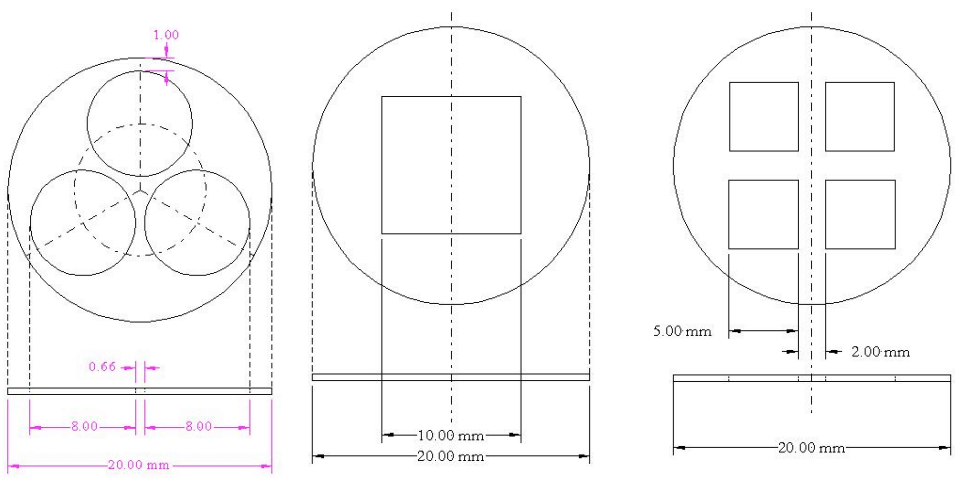

Figure 6.5. Disc Multipurpose coupons, which have 3 different designs for inserts.

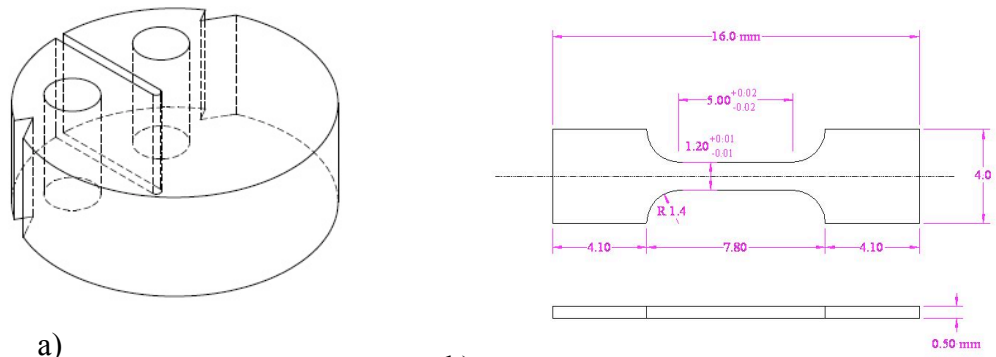

a) b)

Figure 6.6. Schematics for a) disc compact tention (DCT) fracture, and b) SS-J2 flat sheet type tensile specimens

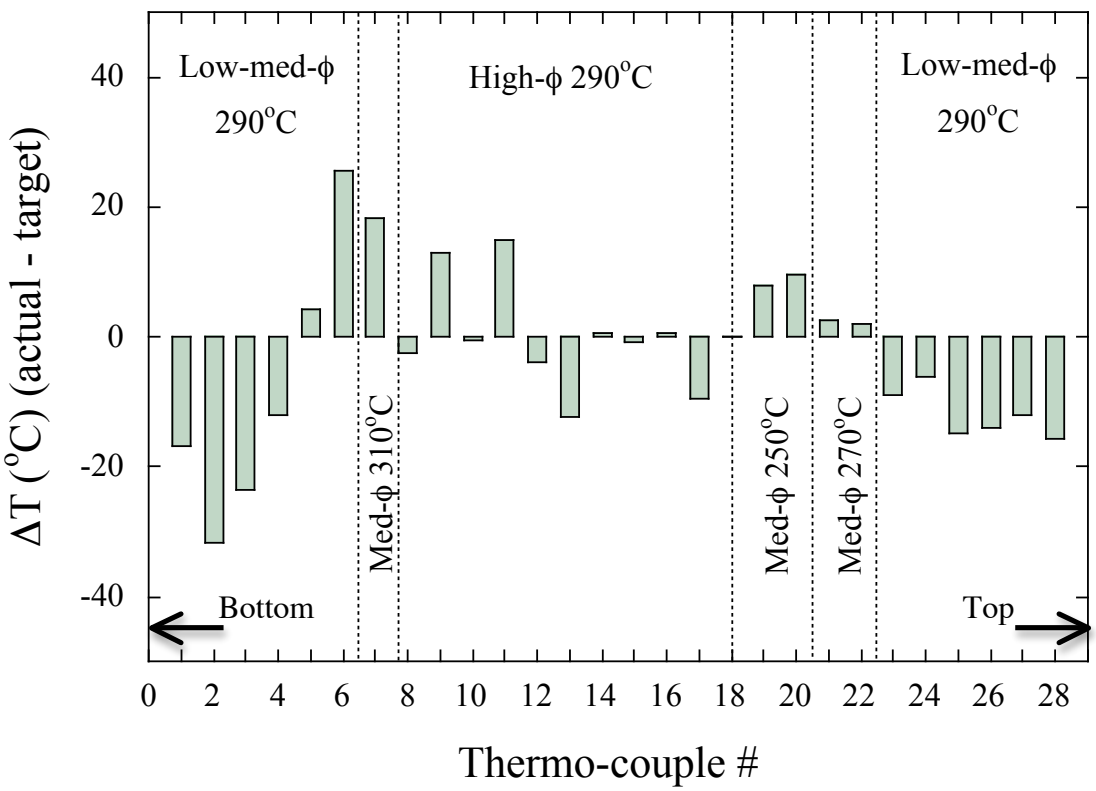

Figure 6.7 Differences of actual temperatures recorded during irradiation from their target value. Except the low-mid flux range at the bottom being slightly affected by adjacent high temperature zone, all the subcapsules are maintained within 20 °C from the target.

REFERNCES

[1] U.S NRC Regulatory Guide 1.99 Revision 2, *Radiation Embrittlement of Reactor Vessel Materials*, U.S. Nuclear Regulatory Commission, Washington DC (1988).

[2] G. R. Odette and G. E., Lucas, Irradiation Embrittlement of Reactor Pressure Vessel Steels, EPRI NP 6114 (1989).

[3] Odette, G. R., "Modeling of Irradiation Embrittlement in Pressure Vessel Steels", *Irradiation Effects on Pressure Vessel Steels*, IAEA IRRWG-LMNPP98-3, International Atomic Energy Agency, Vienna, Austria, 438, 1998.

[4] Odette, G. R. and G. E. Lucas, "Recent Progress in Understanding Reactor Pressure Vessel Embrittlement," *Radiation Effects and Defects in Solids* 144, 189, 1998.

[5] G. R. Odette and G. E. Lucas, "Embrittlement of Nuclear Reactor Pressure Vessel Steels," *JOM*, 53 (7) (2001), p. 18.

[6] G. R. Odette and R. K. Nanstad, "Predictive Reactor Pressure Vessel Steel Irradiation Embrittlement Models: Issues and Opportunities," *JOM*, 61 (7) (2009) p. 17.

[7] Eason, E. D., G. R. Odette, R. K. Nanstad, and T.Yamamoto, *A Physically Based Correlation of Irradiation-Induced Transition Temperature Shifts for RPV Steels*, ORNL/TM-2006/530, Oak Ridge National Laboratory, Oak Ridge, Tennessee, November 2007.

[8] E. D. Eason, G. R. Odette, R. K. Nanstad, T. Yamamoto, "A physically-based correlation of irradiation-induced transition temperature shifts for RPV steels," *J. Nucl. Mater.* **433** (2012) 240.

[9] S. B. Fisher, J. T. Buswell, "A Model For PWR Pressure-Vessel Embrittlement", *Int. Jour. of Pressure Vessels And Piping* 27-2 (1988) 91

[10] C. J. Bolton, J. T. Buswell, R. B. Jones, R. Mskovic and R. H. Priest, "The Modeling of Irradiation Embrittlement in Submerged Arc Welds, *Effects of Radiation on Materials: 17th International Symposium*, ASTM STP 1405, D. S. Gelles et. al. American Society for Testing and Materials, West Conshohocken, PA (2001) 103.

[11] G. R. Odette and G. E. Lucas G E, "Recent Progress in Understanding Reactor Pressure Vessel Embrittlement", *Rad. Effects and Defects in Solids* 144 (1998) 189.

[12] T. J. Williams and D. Ellis, "A Mechanistically-Based Model of Irradiation Damage in Low Alloy Steel Submerged Arc Welds", *Effects of Radiation on Materials: 20th International Symposium*, ASTM STP 1405, S. T. Rosinski et. al. eds. American Society for Testing and Materials, West Conshohocken, PA (2001) 8.

[13] T. J. Williams, D. Ellis, C. A. English and J. Hyde, " A Model of Irradiation Damage in High Nickel Submerged Arc Welds", *Int. Jour. of Pressure Vessels and Piping* 79 (2002) 649

[14] E. D. Eason, J. E., Wright and G. R. Odette, *Improved Embrittlement Correlations for Reactor Pressure Vessel Steels*, NUREG/CR-6551, U.S. Nuclear Regulatory Commission, Washington DC (1998).

[15] G. R. Odette, B. D. Wirth, D. J. Bacon and N. M. Ghoneim, "Multiscale-Multiphysics Modeling of Radiation-Damaged Materials: Embrittlement of Pressure Vessel Steels", *MRS Bulletin,* 26 (2001) 176.

[16] G. R. Odette and B. D. Wirth, "A Computational Microscopy Study of Nanostructural Evolution in Irradiated Pressure Vessel Steels", *J. Nucl. Mater.* 251 (1997) 157.

[17] M. Kirk, C. Santos, E. D. Eason, J. E. Wright and G. R. Odette, Updated Embrittlement Trend Curve for Reactor Pressure Vessel Steels, submitted to SMIRT, (2003).

[18] S. Jumel, C. Domain, J. Ruste et al., "Simulation of Irradiation Effects in Reactor Pressure Vessel Steels: The Reactor for Virtual Experiments (REVE) Project J. Test. Eval., 30-1 (2002) 37

[19] G. R. Odette, G.E. Lucas, D. Klingensmith, B.D. Wirth and D. Gragg, *The Effects of Composition and Heat Treatment on Hardening and Embrittlement of Reactor Pressure Vessel Steels*, NUREG/CR-6778, U.S. Nuclear Regulatory Commission, Washington DC (2003).

[20] R. G. Carter N. Soneda K. Dohi K, et al., "Microstructural Characterization of Irradiation-Induced Cu-Enriched Clusters in Reactor Pressure Vessel Steels", *J. Nucl. Mater.*, 298-3 (2001) 211.

[21] G. R. Odette, P.M. Lombrozo and R.A. Wullaert, "The Relationship Between Irradiation Hardening and Embrittlement of Pressure Vessel Steels", *Effects of Radiation on Materials: 12th International Symposium*, ASTM STP 870, F. A. Garner and J. S. Perrin eds., American Society for Testing and Materials, Philadelphia, PA (1985) 840.

[22] G. R. Odette and M. Y. He, "A Cleavage Toughness Master Curve Model", J. Nuc. Mater. 283 (2000) 120

[23] T. Harry and D. J. Bacon, "Computer Simulation of the Core Structure of the < 111 > Screw Dislocation in Alpha-Iron Containing Copper Precipitates: II. Dislocation-Precipitate Interaction and The Strengthening Effect", *Acta Materialia,* 50 (2002) 209.

[24] B. D. Wirth, G. R. Odette, W. A. Pavinich, G. E. Lucas and S. Spooner, "Small Angle Neutron Scattering Study of Linde80 RVSP Welds", *Effects of Radiation on Materials: 18th Symposium*, ASTM STP 1325, R. K. Nanstad et. al. eds., American Society for Testing and Materials, West Conshohocken, PA (1999) 102.

[25] G. F. Solt, F. Frisius, W. B. Waeber and P. Tipping, "Irradiation Induced Precipitation in Model Alloys with Systematic Variation of Cu, Ni and P Content: A Small Angle Neutron Scattering Study", *Effects of Radiation on Materials-16th International Symposium*, ASTM STP 1175, A S Kumar et. al. eds., American Society for Testing and Materials, West Conshohocken, PA, (1993) 444.

[26] T. J. Williams and W. J. Phythian, "Electron Microscopy and Small Angle Neutron Scattering Study of Precipitates in Low-Alloy Submerged-Arc Welds", *Effects of Radiation on Materials-17th International Symposium*, ASTM 1270, D. S. Gelles et. al. eds., American Society for Testing and Materials, West Conshohocken, PA (1996)191.

[27] G. R. Odette et al., The Effects of Composition and Heat Treatment on Hardening and Embrittlement of Reactor Pressure Vessel Steels, NUREG/CR-6778 (U.S. Nuclear Regulatory Commission, Washington, DC, 2003).

[28] G.R. Odette, T. Yamamoto, E. D. Eason, R. K. Nanstad, "On the Metallurgical and Irradiation Variable Dependence of the Embrittlement of RPV Steels: Converging Mechanistic Based Predictions and Critical Unresolved Issues," *Research for Aging Management of Light Water Reactors and Its Future Trend ed. B. L. Eyre and I. Kimua*, Institute of Nuclear Safety System, Inc., Fukui, Japan (2008) 279.

[29] B. D. Wirth, "On the Character of Nano-Scale Features in Reactor Pressure Vessel Steels Under Neutron Irradiation", PhD. Thesis UC Santa Barbara (1998).

[30] J. Marian, B. D. Wirth, J. M. Perlado, T. Diaz de al Rubia and G.R. Odette, "Atomistic Simulation of Vacancy and Self-Interstitial Diffusion in Fe-Cu Alloys", *Microstructure in Irradiated Materials-2000*, MRS Symp. Proc. 650, G. E. Lucas et. al eds., Materials Research Society, Warrendale, PA (2001), R6.9.

[31] Y. Le Bouar and F. Soisson, "Kinetic Pathways From Embedded-Atom-Method Potentials: Influence of the Activation Barriers", Phys. Rev. B. 65-9 (2002) 094103

[32] G. Salje, and M. Feller-Kneipmeier, "The Diffusion and Solubility of Copper in Iron", *J. of App. Phys* **.,** 48-5 (1977) 1833.

[33] A. D. le Claire, "Solvent Self-Diffusion in Dilute B.C.C. Solid Solutions", *Phil. Mag* 172 (1970) 819.

[34] E. V. Mader, "Kinetics of Irradiation Embrittlement and the Post-Irradiation Annealing of Nuclear Reactor Pressure Vessel Steels", PhD. Thesis, UC Santa Barbara (1995).

[35] C. L. Liu, G. R. Odette, B. D. Wirth and G. E. Lucas, "A Lattice Monte Carlo Simulation of Nanophase Compositions and Structures in Irradiated Pressure Vessel Fe-Cu-Ni-Mn-Si Steels", *Mat, Sci. Eng. A-Struct.,* 238-1 (1997) 202.

[36] G. R. Odette, "Radiation Induced Microstructural Evolution in Reactor Pressure Vessel Steels", *Microstructural Evolution During Irradiation*, Mat Res. Soc. Symp. Proc. 373, I. M. Robertson et. al. eds., Materials Research Society, Warrendale, PA (1995) 137

[37] F. Soisson, A. Barbu and G. Martin,"Monte Carlo Simulations of Copper Precipitation in Dilute Iron-Copper Alloys During Thermal Ageing and Under Electron Irradiation", *Acta Mater.*, 44-3 (1996) 789.

[38] M. K. Miller, P. Pareige and M. G. Burke, "Understanding Pressure Vessel Steels: An Atom Probe Perspective", *Materials Characterization* 44 (2000) 235.

[39] M. K. Miller and P. Pareige, Atomic Level Characterization of Neutron Irradiated Pressure Vessel Steels, *Microstructural Processes in Irradiated Materials*, MRS Soc. Symp. Proc. 650, G. E. Lucas et. al eds., Materials Research Society, Warrendale, PA (2001) R6.1

[40] G.R. Odette, T. Yamamoto, D. Klingensmith, "On the effect of Dose Rate on Irradiation Hardening of RPV Steels", *Phil. Mag.* 85 (2004) 779-797.

[41] G. R. Odette, E. V. Mader, G. E. Lucas, W. J. Phythian and C. A. English, " The Effect of Flux on Irradiation Hardening of Pressure Vessel Steels, *Effects of Radiation on Materials-17th International Symposium*, ASTM 1175, A. S. Kumar

et. al. eds. et., American Society for Testing and Materials, West Conshohocken, PA (1993) 373

[42] P. Asoka-Kumar, B. D. Wirth, P. A. Sterne, R. Howel and G. R. Odette, "Composition and Magnetic Character of Nanometre-size Cu Precipitates in Reactor Pressure Vessel Steels: Implications for Nuclear Power Plant Lifetime Extension, *Phil. Mag. Lett.*, 82-1 (2002) 609

[43] B.D. Wirth, G.R. Odette, P. Asoka-Kumar, R.H. Howell and P.A. Sterne, "Characterization of Nanostructural Features in Irradiated Reactor Pressure Vessel Model Alloys", *Proceedings of the 10th International Symposium on Environmental Degradation of Materials in Light Water Reactors*, G. S. Was et. al. eds., NACE (2001).

[44] Y. Nagai, Z. Tang, M. Hasegawa, T. Kanai and M. Saneyasu, Irradiation Induced Cu Aggregation in Fe: An Origin of Embrittlement of Pressure Vessel Steels, *Phys. Rev. B*, 63-13 (2001) 134110-2

[45] M. Hasegawa, Y. Nagai, Z. Tang, T. Kanai and T. Chiba, "Positron Annihilation Characterization of Ultrafine Cu Precipitates and Vacancy Cluster Complexes in Thermally Aged and Neutron Irradiated Fe-Cu Model Alloys", *Proceedings of the 10th International Symposium on Environmental Degradation of Materials in Light Water Reactors*, G. S. Was et. al. eds., NACE (2001)

[46] L. K. Mansur, A. D. Brailsford and W. G. Wolfer, "On The Meaning Of Sink Capture Efficiency and Sink Strength for Point-Defects", J. Nucl. Mater., 105-1 (1982) 36

[47] A. Moslang, E. Albert, E. Recknagel and A. Weidinger, "Interaction of Vacancies With Impurities in Iron", *Hyperfine Interactions*, 15/16 (1983) 409

[48] E. V. Mader, "Kinetics of Irradiation Embrittlement and the Post-Irradiation Annealing of Nuclear Reactor Pressure Vessel Steels", PhD. Thesis, UC Santa Barbara (1995).

[49] B.D. Wirth and G.R. Odette, "Kinetic Lattice Monte Carlo Simulations of Cascade Aging in Iron and Dilute Iron-Copper Alloys", *Microstructural Processes in Irradiated Materials*, MRS Soc. Symp. Proc. 540, S. J. Zinkle et. al eds., Materials Research Society, Warrendale, PA (1999) 637.

[50] B.D. Wirth, G.R. Odette and R.E. Stoller, "Recent Progress Toward an Integrated Multiscale-Multiphysics Model of Reactor Pressure Vessel Embrittlement", *Multiscale Modeling of Materials*, MRS Soc. Symp. Proc. 677, V. Bulatov et. al. eds., Materials Research Society, Warrendale, PA (2001) AA5.2.

[51] C. Domain, C. S. Becquart, J. C. Van Duysen, "Kinetic Monte Carlo Simulations of Cascaded in Fe Alloys", *Microstructure in Irradiated Materials-2000*, MRS Symp. Proc. 650, G. E. Lucas et. al eds., Materials Research Society, Warrendale, PA (2001) R3.25

[52] G. R. Odette, "On the Dominant Mechanism of Irradiation Embrittlement in Pressure Vessel Steels", *Scripta Met.*, 11 (1983) 1183.

[53] E. S. Machlin, *An Introduction to Therodynamics and Kintetics Relevant to Materials Science*, 2nd ed., Giro Press, Croton-on Hudson, NY (1999)

[54] Odette, G. R., and G. E. Lucas, "The Effect of Nickel in Irradiation Hardening of Pressure Vessel Steels," E*ffects of Radiation on Materials: 14th International*

Symposium, ASTM STP 1046, ed. N. H. Packan et al., American Society for Testing and Materials, West Conshocken, PA,, 323, 1990

[55] Glade, S. C., B. D. Wirth, P. Asoka-Kumar, P A. Sterne, and G. R. Odette, "Positron Annihilation Spectroscopy of Nanostructural Features in Model Reactor Pressure Vessel Steels", *Materials Science Forum* 445-446 (2004) 87.

[56] Glade, S. C., B. D. Wirth, G. R.. Odette, P. Asoka-Kumar, P. A., Sterne, and R. H. Howell, "Positron Annihilation Spectroscopy and Small Angle Neutron Scattering Characterizations of the Effect of Mn on the Nanostructural Features Formed in Irradiated Fe-Cu-Mn Alloys," *Philosophical Magazine* 85 (2005) 629.

[57] Glade, S. C., B. D. Wirth, G. R. Odette and P. Asoka-Kumar, "Positron Annihilation Spectroscopy and Small Angle Neutron Scattering Characterization of Nanostructural Features in High-Nickel Model Reactor Pressure Vessel Steels," *J. Nucl. Mater* 351 (2006) 197.

[58] R. Chaouadi, "An Engineering Radiation Hardening Model for RPV Materials," SCK/CEN Report R-4235, September 2005

[59] R. K. Nanstad, G. R. Odette, R. E. Stoller, T. Yamamoto, "Review of Draft NUREG Report on Technical Basis for Revision of Regulatory Guide 1.99," ORNL/NRC/LTR-08/03 (2008).

Appendix 1: Publications and presentations from this work

P1. G. R. Odette, T. Yamamoto, D. Klingensmith, G.E. Lucas, "A Review of Flux Effects Found in the IVAR Database," International Group for Radiation Damage Mechanisms (IGRDM15), October 11-16, 2009, Budapest, Hungary.

P2. G. R. Odette, T. Yamamoto, D. Klingensmith, "An Update on High Flux-High Fluence Irradiation Hardening: Observations and Models," International Group for Radiation Damage Mechanisms (IGRDM15), October 11-16, 2009, Budapest, Hungary.

P3. G. R. Odette, T. Yamamoto, R. K. Nanstad, B.D. Wirth and M. Meyer, "A Reactor Pressure Vessel Extended Life Support Irradiation Experiment in the Advanced Test Reactor National Scientific Users Facility," International Group for Radiation Damage Mechanisms (IGRDM15), October 11-16, 2009, Budapest, Hungary.

P4. T. Yamamoto, G. R. Odette, T. J. Williams, "A Physically Based Integrated IVAR-PREDB Hardening and Embrittlement Model: Update on UMD Hardening Model," International Group for Radiation Damage Mechanisms (IGRDM15), October 11-16, 2009, Budapest, Hungary.

P5. N. Soneda, K. Nishida, K. Dohi, A. Nomoto, G. R. Odette, T. Yamamoto, "Flux Effect on the Hardening of High Copper IVAR Material, LI," International Group for Radiation Damage Mechanisms (IGRDM15), October 11-16, 2009, Budapest, Hungary.

P6. R. K. Nanstad and G. R. Odette, "Reactor Pressure Vessel Issues for the Light Water Reactor Sustainability Program" International Group for Radiation Damage Mechanisms (IGRDM15), October 11-16, 2009, Budapest, Hungary.

P7. G. R. Odette, T. Yamamoto and D. Klingensmith Flux Effects on Irradiation Hardening High Fluence: Models and Recent Observations, ASTM Workshop on Obtainment and Use of High Fluence Surveillance Data to Improve Existing Embrittlement Correlations, San Antonio, TX, 1/26/2010

P8. R. K. Nanstad and G. R. Odette, Reactor Pressure Vessel Issues for the Light Water Reactor Sustainability Program, ASTM Workshop on Obtainment and Use of High Fluence Surveillance Data to Improve Existing Embrittlement Correlations, San Antonio, TX, 1/26/2010

P9. G. R. Odette, T. Yamamoto and D. Klingensmith, Developing Knowledge Base for Predicting Low Flux High Fluence RPV Embrittlement, Extended Service Materials Working Group Meeting, EPRI, Palo Alto, CA 2/10-11/2010

P10. R. K. Nanstad and G. R. Odette, Plans/Activities for the DOE Light-Water Reactor Sustainability Program RPV Task Including an ATR Experiment Extended Service Materials Working Group Meeting, EPRI, Palo Alto, CA, 2/10-11/2010

P11. G. R. Odette, T. Yamamoto and D. Klingensmith, When the Turtle Can't Get There and the Rabbit Gets Lost: Predicting Low Flux-High Fluence RPV Embrittlement, TMS 2010, Seattle, Wa, 2/10-14/2010

P12. R. K. Nanstad and G. R. Odette Ensuring the Performance of Nuclear Reactor Pressure Vessels for Long Time Service, TMS 2010, Seattle, Wa, 2/10-14/2010

P13. R.K. Nanstad and G.R.Odette and M. A. Sokolov, Ensuring the Performance of Nuclear Reactor Pressure Vessels For Long Time Service, 2010 ASME PVP Conference, Bellevue, WA, 7/18-22/2010

P14. G. Robert Odette, Takuya Yamamoto, Douglas Klingensmith, David Gragg, Ben Sams, Mitchell Meyer, Gregg Wachs, Julie Foster, James Cole, Dan Ogden, Michael Sprenger, Thomas Maddock, Paul Murray, Joseph Nielsen, Randy Nanstad, William Server, "Status of UCSB ATR-1 and ATR-2 Experiments," TMS 2011 140th Annual Meeting & Exhibition, February 27 – March 3, 2011, San Diego, CA.

P15. G. R. Odette, T. Yamamoto, N. Cunningham, and D. Klingensmith, "Experimental and Modeling Studies on the Effects of a Wide Range of Flux on the Microstructures and Mechanical Properties of RPV Steels Predicting Low Flux High Fluence Embrittlement," ASTM 25th Symposium on Effects of Radiation on Nuclear Materials, June 15-17, 2011, Anaheim, CA.

P16. T Yamamoto, and G. R. Odette, "Analyses of IVAR Database for an Advanced MD/CRP Hardening Models," ASTM 25th Symposium on Effects of Radiation on Nuclear Materials, June 15-17, 2011, Anaheim, CA.

P17. G. R. Odette, P. Wells, T. Yamamoto, D. Klingensmith, E. Mader, E. Eason, J. Wright, "A Brief Review of Low Temperature Annealing of Irradiated RPV Steels," IGRDM-16, Dec. 4-9, 2011, Santa Barbara, CA.

P18. G. R. Odette, T. Yamamoto, N. Cunningham, D. Klingensmith, "A Review of Developing a Mechanism-Microstructure Based Low Flux High Fluence Model," IGRDM-16, Dec. 4-9, 2011, Santa Barbara, CA.

P19. G. R. Odette, T. Yamamoto, D. Klingensmith, G.E. Lucas, M. Meyer, D. Ogden, M. Sprenger, T. Maddock, P. Murrey, J. Nielsen, R. Nanstad, W. Server, "The Status of the UCSB ATR2 RPV Irradiation Experiments," IGRDM-16, Dec. 4-9, 2011, Santa Barbara, CA.

P20. T. Yamamoto, G. R. Odette, D. Klingensmith, "A Semi-empirical Analysis of the Precipitate Contribution to Hardening in the IVAR Database," IGRDM-16, Dec. 4-9, 2011, Santa Barbara, CA.

P21. T. Yamamoto, T. Toyama, Y. Nagai, G. R. Odette, D. Klingensmith, "Effects of Post-Irradiation Annealing on BR2 Irradiated RPV Steels Characterized by Positron Annihilation and Microhardness," IGRDM-16, Dec. 4-9, 2011, Santa Barbara, CA.

P22. N. Soneda, K. Nishida, K. Dohi, G. R. Odette, T. Yamamoto, D. Klingensmith, "Effect of irradiation temperature on the Cu-enriched clusters in Cu-containing RPV materials," IGRDM-16, Dec. 4-9, 2011, Santa Barbara, CA.

P23. K. Nishida, N. Soneda, K. Dohi, G. R. Odette, T. Yamamoto, D. Klingensmith, "Effect of Ni and Mn on the Cu-enriched clusters," IGRDM-16, Dec. 4-9, 2011, Santa Barbara, CA.

P24. T. Yamamoto, P. Wells, T. Toyama, Y. Nagai, A. Kimura, Y. Wu, and G. R. Odette, "Microstructural characterization of test reactor irradiated RPV steels by post-irradiation annealing and state-of-the-art characterization tools," NuMat 2012, Oct. 21-25, 2012, Osaka, Japan.

Appendix 2: Publications and presentations from related work

P1. T. Williams, G. R. Odette, T. Yamamoto, K. Wilford, "Effect of High Flux on Irradiation Embrittlement: Assessment of Test Reactor Data," International Group for Radiation Damage Mechanisms (IGRDM15), October 11-16, 2009, Budapest, Hungary.

P2. T. Williams, G. R. Odette, T. Yamamoto, "Relationship between Changes in Tensile Properties and Hardness," International Group for Radiation Damage Mechanisms (IGRDM15), October 11-16, 2009, Budapest, Hungary.

P3. P. Wells, N. J. Cunningham, G. R. Odette, D. Klingensmith and T. Yamamoto, "Some APT Observations and Issues," IGRDM-16, Dec. 4-9, 2011, Santa Barbara, CA.

P4. Peter Wells, G. Robert Odette, Yuan Wu, Tim Milot, Takuya Yamamoto, Doug Klingensmith and Nick Cunningham, "The Search for Late Blooming Phases: Atom Probe Tomography of Irradiated RPV Steels and Model Alloys," 2012 MRS Spring Meeting, April 9-13, 2012, San Francisco, CA.

P5. G. R. Odette and R. K. Nanstad, "A Brief History and Current Status of Insight on Late Blooming Ni-Mn-Si Phases in Irradiated RPV Steels," Soteria – PERFORM60 meeting, Seville, Spain, September 17, 2012

P6. P. Wells, T. Yamamoto, Y. Wu, T. Milot, G. R. Odette, J. I. Cole, B. Miller, K. Yabuuchi, A. Kimura, "Late Blooming Phases in RPV steels: High Fluence Neutron and Ion Irradiations," NuMat 2012, Oct. 21-25, 2012, Osaka, Japan.

P7. G. Robert Odette et al., "On the Evolution Late Blooming Phases in RPV Steels: Theoretical Foundations, Experimental Observations and Recent Insights," TMS 2013 142th Annual Meeting & Exhibition, March 3 - 7, 2013, San Antonio, TX.

P8. Yuan Wu, Takuya Yamamoto, Peter Wells, Nicholas J. Cunningham, G. Robert Odette, Kiyohiro Yabuuchi, Akihiko Kimura, James I. Cole, "TEM Characterization of Dislocation Loops and Precipitates in RPV Steels under Neutron and Charged Particle Irradiations," TMS 2013 142th Annual Meeting & Exhibition, March 3 - 7, 2013, San Antonio, TX.

P9. Peter Wells et al., "Ni-Si-Mn Dominated Late Blooming Phases in RPV Steels at High Fluence and Flux," TMS 2013 142th Annual Meeting & Exhibition, March 3 - 7, 2013, San Antonio, TX.

P10. Peter Wells et al., "On the Evolution of Ni-Si-Mn Dominated Phases and Solute Segregation in RPV Steels under Charged Particle Irradiation," TMS 2013 142th Annual Meeting & Exhibition, March 3 - 7, 2013, San Antonio, TX.